Dissertation

Put forward by

Pavlo V. Bilous

Born in: Kherson, Ukraine

Oral examination: 13.12.2018

Towards a nuclear clock with the ^{229}Th isomeric transition

Zusammenfassung

Der Kern ^{229}Th mit seinem Isomerzustand bei 7.8 eV ist ein einzigartiger Kandidat für die erste *nukleare* optische Uhr mit außerordentlicher Genauigkeit von 10^{-19}. Aufgrund der niedrigen Isomerübergangsenergie ist die Kopplung an die atomare Hülle bei den Prozessen der inneren Konversion (IK) oder Elektronenbrücke (EB) sehr stark. In dieser Arbeit untersuchen wir theoretisch die IK- und EB-Mechanismen und entwerfen neuartige lasergestützte Systeme, die auf (*i*) eine genauere Bestimmung der Isomerenenergie E_m und (*ii*) effiziente Anregung des Isomers abzielen. Einerseits zeigen wir, wie die IK von angeregten elektronischen Zuständen von Th-Ionen zur Bestimmung der Isomerübergangsenergie verwendet werden kann. Wir schlagen auch einen neuen Ansatz zur Messung der Isomerenergie mit Laserspektroskopie-Genauigkeit mit der laserinduzierten EB in ^{229}Th^{3+} Ionen vor. Andererseits stellen wir mögliche Isomeranregungsschemata vor, die auf dem EB-Prozess in hochgeladenen Th-Ionen oder auf lasergestützter Kernanregung durch Elektroneneinfang des 29.19 keV-Kernzustands direkt über dem Isomer beruhen. Durch die Anwendung von hochgeladenen Ionen wird möglich, die EB optisch mit Hochleistungslasern zu treiben, was laut unserer Ergebnisse zu einer effizienten Anregung führen sollte. Ein solcher Aufbau mit Ionenfallen könnte für die zukünftige Entwicklung der Atomkernuhr relevant werden.

Abstract

The ^{229}Th nucleus with its 7.8 eV isomeric state is a unique candidate for the first *nuclear* optical clock at an exceptional accuracy of 10^{-19}. Due to the low isomeric transition energy, the coupling to the atomic shell in the processes of internal conversion (IC) or electron bridge (EB) is very strong. In this work we investigate theoretically the IC and EB mechanisms and design novel laser-assisted schemes aimed at (*i*) a more accurate determination of the isomer energy E_m and (*ii*) efficient excitation of the isomer. On the one hand, we show how IC occurring from excited electronic states of Th ions can be used to determine the isomeric transition energy. We also propose a new approach to measure the isomer energy with laser spectroscopy accuracy via laser-induced EB in ^{229}Th^{3+} ions. On the other hand, we put forward possible isomer excitation schemes based on the EB process in highly charged Th ions or on laser-assisted nuclear excitation by electron capture of the 29.19 keV nuclear state lying directly above the isomer. Our results show that EB in highly charged ions which allow optical driving with high-power lasers should lead to efficient excitation. Such a setup using ion traps might become relevant for the future development of the nuclear clock.

Within the framework of this thesis, the following articles were published in refereed journals:

- ***Internal conversion from excited electronic states of*** ^{229}Th ***ions***
  Pavlo V. Bilous, Georgy A. Kazakov, Iain D. Moore, Thorsten Schumm, and Adriana Pálffy.
  Phys. Rev. A **95**, 032503 – Published 13 March 2017

- ***Laser-induced electronic bridge for characterization of the*** ^{229m}Th $\rightarrow$ ^{229g}Th ***nuclear transition with a tunable optical laser***
  Pavlo V. Bilous, Ekkehard Peik, and Adriana Pálffy.
  New J. Phys. **20**, 013016 – Published 10 January 2018

- ***Electric quadrupole channel of the 7.8 eV*** ^{229}Th ***transition***
  Pavlo V. Bilous, Nikolay Minkov, and Adriana Pálffy.
  Phys. Rev. C **97**, 044320 – Published 25 April 2018

Articles in preparation:

- ***Electronic bridge excitation of the 7.8 eV nuclear isomeric state in highly charged*** ^{229}Th ***ions***
  Pavlo V. Bilous, Hendrik Bekker, José R. Crespo López-Urrutia, and Adriana Pálffy.

- ***Theory of laser-assisted nuclear excitation by electron capture***
  Pavlo V. Bilous and Adriana Pálffy.

to Daria Bilous,

my love and my source of inspiration

Contents

Introduction

Frequency standards play an important role in modern science and technology. For instance, satellite-based systems of radionavigation such as the Global Positioning System (GPS) are able to provide a position determination with a few-meter accuracy due to a set of frequency standards operating onboard of satellites. In such systems the user to be located receives signals emitted synchronously by a number of satellites, typically at least four. The position is then determined by the time difference of the reception events. Frequency standards are employed in this scheme for achievement of a high level of synchronization in the signal emission. In the field of metrology, frequency standards are used first of all for precise measurements of time. The notions "clock" and "frequency standard" are often used as synonyms due to the fact that the time measurement procedure typically reduces to counting of the number of periods of some oscillating system. A second is defined as the duration of exactly $9\,192\,631\,770$ oscillations of a Cs atomic frequency standard, where the electronic transition between the two hyperfine levels of the ground state of the ^{133}Cs atom is used as the oscillator [1].

The most accurate frequency standards today are atomic standards based on electronic microwave or optical transitions. The first practical idea of implementation of a microwave clock was proposed by Isidor Rabi [2] based on the magnetic resonance method developed by Rabi and his collaborators in the end of 1930s [3]. The first precise atomic frequency standard based on the microwave electronic transition in the ^{133}Cs atom excited and interrogated by radiofrequency signals was built by Louis Essen and Jack Parry at the National Physical Laboratory in the UK in 1955 [4]. This opened an era of microwave atomic clocks which rapidly outperformed their quartz-based predecessor. During the 20th century the accuracy of the microwave frequency standards, i.e., the ratio of the time shift ΔT to the measured time interval T, reached 10^{-15} [5].

The next generation of atomic frequency standards is based on electronic transitions in the optical range. The operating frequency in such clocks is a few orders higher than in the Cs clock with the microwave transition. This brings the advantage that the same error in the number of counted oscillations is "collected" during a much shorter time allowing more efficient and simple correction of the systematic frequency shift of the standard. Started in the 1980s [6], the development of such optical frequency standards was boosted around the turn of the 21st century when an optical frequency comb was developed [7, 8]. The frequency comb technique allows linking the optical frequency to a radiofrequency which can be then effectively measured by means of ordinary electronics. A proper choice of the electronic transition for the optical frequency standard is of crucial importance. It should have a narrow spectral width and be stable enough with respect to external perturbing fields. The excitation of the atomic system to the involved electronic states should be at the same time straightforward with laser sources available today. Such transitions have been found in a number of ions and neutral atoms. The most advanced frequency standards based on an electronic transition in a trapped single ion achieved the relative accuracy of 10^{-17} for ions ^{199}Hg^{+} and ^{27}Al^{+} [9, 10]. Clocks based on a few thousand neutral atoms placed in an optical lattice were a further breakthrough in optical frequency standards. The accuracy reached a few years ago in such clocks with atoms ^{171}Yb [11] and ^{87}Sr [12] was of the order 10^{-18}. This year (2018) a record precision

of $2.5 \cdot 10^{-19}$ obtained with the ^{87}Sr-based standard has been reported in Ref. [13].

In order to fully exploit the technical opportunities rendered possible by the high accuracy of the ^{87}Sr clock, it is important to make a comparison with another state-of-art frequency standard. An opportunity to develop such a standard is offered by the isotope ^{229}Th, which possesses a nuclear excited state at the energy $E_m = 7.8 \pm 0.5$ eV [14, 15]. In nuclear physics terms this state is a so-called isomer — denoted ^{229m}Th — due to its long lifetime. The mere radiative lifetime of the state is estimated at 10^4 s. Since the energy $E_m = 7.8 \pm 0.5$ of the isomer ^{229m}Th lies in the optical (VUV) range, ^{229}Th is considered as a candidate for the first *nuclear* optical frequency standard at an unprecedented accuracy of 10^{-19} for a single Th ion [16–18]. This accuracy, achieved due to the very narrow width of the transition between the excited and the ground states and the high stability to external perturbations, corresponds to an error of about 10^{-11} seconds per year which converts to a ten-millisecond shift during the time equal to the age of the Universe. A clock of such precision would be sensitive to the variation of the gravitational field corresponding to the altitude change of a few cm at the Earth surface. This would allow its application for experimental tests of the general theory of relativity. Furthermore, it has been proposed to use a nuclear frequency standard based on ^{229}Th for fundamental applications such as the detection of time variation of fundamental physical constants [19] which is predicted by many theories beyond the standard model and may be caused by presence of dark matter in the Universe [20]. Among other exciting applications of the nuclear isomeric state in ^{229}Th are the first laser operating between nuclear states [21] and coherent control of the nuclear transition with a VUV laser [22].

The nuclear state at $E_m = 7.8 \pm 0.5$ eV in ^{229}Th is an extremely peculiar case from the point of view of nuclear physics dealing typically with electromagnetic excitations in the keV or MeV range. Its existence was predicted in 1976 by Kroger and Reich [23] based on the γ-ray spectrum of ^{229}Th produced from α-decay of ^{233}U. Energy intervals between some levels obtained from this spectrum contradicted to theoretical predictions unless an additional level were present which could not be resolved from the ground state by means of γ-ray spectroscopy. The upper limit for the energy of this state was set 100 eV based on measurement accuracy. Since that time, the value E_m has been measured and updated over a few decades [24–27] by means of resolution improvement of the γ-ray spectra and the usage of more advanced methods for extraction of the isomer energy from the experimental data. The value $E_m = 7.8 \pm 0.5$ eV widely used today was reported only about ten years ago [14, 15] and was provided by an indirect measurement of the X-ray decay cascades following α-decay of ^{233}U. The first direct observation of the nuclear isomeric state in ^{229}Th was reported only in 2016 [28] without providing a transition energy measurement.

Electromagnetic transitions in a bare nucleus occur by absorption or emission of a photon. In the case of a nucleus surrounded by the electronic shell, these transitions may involve the atomic electrons. The simplest and the most known case is the internal conversion (IC) process, in which the energy of the nuclear excitation is transferred to an electron. Since nuclear excitations lie typically in the keV or MeV range, this energy is in most cases large enough to expel the electron from the electronic shell. Due to the very low energy of the isomer ^{229m}Th, IC can occur only in neutral atoms and expels the outermost electron. This process has been experimentally observed [28] and appears to have a nine orders of magnitude faster rate than the radiative decay rate of the isomeric state [29]. At the same time, if an electronic transition between bound states in a Th ion happens to be energetically close to the value of E_m, the nuclear

4

decay may occur simultaneously driving this atomic shell transition. In order to fulfill energy conservation, this process is accompanied by the emission of a photon. We refer to this scenario as to electronic bridge (EB) [30, 31]. The EB channel in turn may lead to a fast decay of the isomer in ^{229}Th ions as shown by calculations in Ref. [30, 31]. As a consequence, the isomeric transition in ^{229}Th may be broadened due to the strong coupling of the nuclear and electronic degrees of freedom. It is therefore of paramount importance to completely understand and potentially exploit this coupling for the isomer energy determination and isomer excitation alike.

This thesis is dedicated to the theoretical investigation of excitation and decay mechanisms of the nuclear isomeric state in ^{229}Th involving atomic electrons. Our aim is to exploit such processes in new laser-assisted schemes for efficient excitation of the isomeric state and for an accurate direct measurement of the isomeric energy. These studies are of relevance since the implementation of a nuclear frequency standard based on the isomer ^{229m}Th requires an excitation mechanism of this state, which in turn depends on the exact value of the transition energy. Although it is believed that the latter lies in the accessible range of VUV laser sources, direct excitation of the isomer has not been achieved so far. Due to the very low accuracy of the value $E_m = 7.8 \pm 0.5$ eV, the scanning time of a tunable VUV laser is prohibitively long. A tunable VUV laser is itself a technological challenge and the working concept depends on the more exact range required for operation. In addition, it is possible that the actual value E_m lies outside the error bars ± 0.5 eV. This may explain why the attempts to excite the nuclear isomer ^{229m}Th using broadband synchrotron radiation have been unsuccessful [32, 33]. We show in this thesis how such difficulties might be circumvented by taking advantage of the electronic shell as a resonator in four novel laser-driven schemes involving existing laser technologies in the optical, ultraviolet (UV) or X-ray regime.

Starting from the process of IC, in this thesis we address for the first time IC from excited electronic states, which can uniquely occur in ^{229}Th. We recall that IC is energetically forbidden in ^{229}Th ions starting already with Th$^+$. However, the IC channel can be opened by prior laser excitation of the electronic shell. We perform extensive IC calculations taking into account the multipole mixing between the magnetic dipole and electric quadrupole components of the nuclear transition. Based on our numerical results, we put forward a scheme that can make use of the process of IC from excited electronic states to determine the strength of the isomeric transition and estimate the energy value E_m.

Based on the process of EB, we put forward a new method to determine the isomer energy with accuracy typical for laser spectroscopy in the process of laser-induced EB (LIEB) in ^{229}Th^{3+} ions. In the LIEB process the decay of the nuclear excitation is accompanied not by emission but by absorption of a photon from the externally applied laser field. LIEB is allowed by the energy conservation laws only for particular frequencies of the laser radiation which can be determined experimentally using a tunable optical or UV laser source. The laser radiation for which the LIEB process is observed can be linked to a precise value of the isomer energy E_m.

The inverse EB process can be used for the isomer excitation, in which the external photon from an optical or UV laser is absorbed by an already excited electronic shell [34]. This promotes the electron to a (virtual) excited state which decays simultaneously driving the nuclear transition. As shown in Ref. [34], such an excitation can be implemented in the ^{229}Th$^+$ ion using optical lasers. The proper choice of the involved electronic states is however a severe limitation for the EB excitation. It remains a mere

guess as long as the energy E_m is not known with sufficient precision. At the same time, there is a limitation to the applied laser power due to multi-photon ionization of ^{229}Th$^+$. In order to avoid these disadvantages, in this thesis we propose for the first time to use highly charged ions (HCI) ^{229}Th with open d and f shells instead of Th$^+$. The rich electronic spectra of HCI offer possible excitation schemes at different values E_m and pose no restrictions on the power of the applied light sources due to large ionization potential of HCI. Examining particular excitation schemes in HCI ^{229}Th, we show that a considerable excitation rate can be achieved using laboratory means available today.

Finally, in this thesis we also propose and investigate a possible excitation mechanism for the isomer ^{229m}Th via the nuclear level at the energy 29.19 keV which decays predominantly to the ^{229m}Th state. Since the transition energy of 29.19 keV lies above the present-day capabilities of X-ray free electron lasers (XFEL), we envisage excitation via the electronic shell in the process of laser-assisted nuclear excitation by electron capture (LANEEC). Schematically, LANEEC requires that a two-color XFEL creates simultaneously an inner-shell hole and expels an outer-shell electron which then recombines in the created inner-shell hole with the simultaneous excitation of the nucleus. Since this process has not been considered yet in literature, we provide a complete rigorous theoretical analysis based on the Feshbach projection operator formalism. Although the calculated excitation rate turns out to be small, a comparison with the process of two-photon nuclear absorption reveals that LANEEC enhances the excitation probability by more than ten orders of magnitude due to the involvement of the electronic shell. This process may therefore find future applications in the area of X-ray quantum optics with nuclei.

The thesis is structured as follows. Chapter 1 contains a detailed analysis of the IC process in a neutral ^{229}Th atom and ^{229}Th ions. Here we investigate the experimental scheme for characterization of the nuclear isomer ^{229m}Th based on IC from excited states in ^{229}Th ions and we also provide a theoretical foundation to the experimental proposal in Ref. [28, 35] to determine E_m by a precise measurement of the energy of the electrons converted from neutral ^{229}Th atoms. Chapter 2 is devoted to the EB process in ^{229}Th ions. Following an introduction in the theory of EB decay, we analyze the experimental scheme based on the LIEB process with a tunable optical laser. Furthermore, we study in this Chapter the possibility to excite the isomer ^{229m}Th in HCI using the inverse EB process. In Chapter 3 we investigate the LANEEC excitation scheme of the nuclear isomer ^{229}Th. Based on the Feshbach projection operator formalism, we develop the theory of the LANEEC process and evaluate the excitation rate. Chapter 4 is completely devoted to the description of the numerical methods used in the present work based both on existing packages and the codes developed in the frames of this project. The thesis concludes with Summary and Outlook. Atomic units ($\hbar = e = m_e = 1$) are used throughout this work unless otherwise mentioned.

Chapter 1

Internal conversion (IC)

In ^{229}Th, the ground state $\frac{5}{2}^+$ is connected to the isomeric state $\frac{3}{2}^+$ via a magnetic dipole ($M1$) mixed with an electric quadrupole ($E2$) transition. Due to the very low energy E_m of the transition from the isomeric nuclear state to the ground state in the isotope ^{229}Th, the radiative decay is strongly suppressed, since its rate is proportional to E_m^3 for a dipole and E_m^5 for a quadrupole nuclear transition. If the nuclear excitation energy E_m exceeds the ionization threshold, the isomer decay becomes dominated by the IC process, in which the nuclear excitation is transferred to the electronic shell with is then ionized. The IC rate Γ_{IC} has a relatively weak dependence on the energy E_m in comparison to the radiative decay rate Γ_{rad}, because E_m enters to the expression for Γ_{IC} only indirectly via the wave functions of the continuum electron. Therefore, the value Γ_{IC} in contrast to Γ_{rad} does not decrease significantly at small E_m and leads to a large value of the IC coefficient $\alpha_{\text{IC}} = \Gamma_{\text{IC}}/\Gamma_{\text{rad}}$. In this Chapter we carry out a thorough analysis of the IC process in ^{229}Th, which due to the very low energy $E_m \sim 10$ eV has special properties in comparison to the ordinary IC at keV energies. We calculate the IC rates for different electronic shells in a neutral ^{229}Th atom and ^{229}Th ions taking into account mixing between the magnetic dipole and electric quadrupole components of the nuclear transition. We also consider possible applications of this phenomenon for characterization of the ^{229}Th isomeric state.

It has been experimentally shown [28] that the IC decay channel for the nuclear isomer ^{229m}Th in a neutral atom strongly dominates in agreement with the predicted IC coefficient of $\alpha_{\text{IC}} \sim 10^9$. In this experiment electrons originating from IC in neutral ^{229}Th were detected. Comparison with the case of ^{232}Th atoms, which do not possess any nuclear excited states at low energies, has shown that the detected signal can be completely attributed to the ^{229}Th isomeric state. Based on this experimental scheme, it has been proposed to carry out a measurement of the energies of the IC electrons and evaluate the isomer energy E_m [28, 35] with the help of the obtained data. The IC electrons in such an experiment would not have a single energy value due to the following reasons. On the one hand, the final ion ^{229}Th$^+$ after IC can be not only in the ground state but in a number of excited states. On the other hand, the production procedure of the neutral ^{229}Th atoms used by the authors of Ref. [28] leads inevitably to excitation of the outer electrons of the atom prior to IC. It results in the appearance of a number of lines with different strengths in the IC electron energy spectrum. In this Chapter we carry out a detailed investigation of the IC electron energy distribution and predict the IC electron spectra for different values of E_m and different initial electronic states of the atom ^{229}Th. The results are both of fundamental importance for understanding of the IC process at low energies and serve as a theoretical support for the experiment proposed in Ref. [28, 35].

Whereas the IC process is energetically allowed for neutral Th, it becomes forbidden already for the ion ^{229}Th$^+$, as its ionization potential exceeds the presumed nuclear transition energy E_m (see Table 1.1). In this case IC only from an excited electronic

state may take place. We note that in most cases of IC studied in nuclear physics,

Ion charge	0	1+	2+	3+	4+
Ion. threshold (eV)	6.3	12.1	20.0	28.7	58

Table 1.1: Ionization thresholds for several charges of ^{229m}Th ions [36, 37].

the electronic state of the atom prior to IC is its ground state, since given the usually high nuclear transition energy mostly electrons from inner shells are converted. Due to the very low value E_m for the isomer ^{229m}Th, it is a unique case in which IC from excited electronic states becomes possible. In this Chapter we propose an experimental scheme based on the IC from excited electronic states in ^{229}Th ions for characterization of the ^{229}Th isomeric state [38]. If a ^{229}Th ion is prepared in an excited electronic state at an energy exceeding the difference between the ionization threshold and the isomer energy E_m, IC from this excited state may occur resulting in a production of ions in a higher charge state. Detection of these ions can be carried out with high efficiency, whereas a comparison of the result with the case of ^{232}Th would allow to obtain the signal originating only from the nuclear isomer ^{229m}Th. We formulate requirements for the electronic state from which the IC is observed and choose proper electronic levels from the spectra of ^{229}Th ions for different values of the isomer energy E_m.

1.1 IC theory

We develop in this Section a theoretical background necessary for calculation of IC rates. The IC process occurs due to the electromagnetic coupling of the nuclear multipole moments to the electronic shell. As shown in Appendix A, the corresponding Hamiltonian can be represented as

$$\hat{H}_{\text{int}} = \sum_{\lambda L, q} (-1)^q \hat{\mathcal{M}}_{\lambda L, q} \hat{\mathcal{T}}_{\lambda L, -q} \,, \tag{1.1}$$

where $\hat{\mathcal{M}}_{\lambda L, q}$ and $\hat{\mathcal{T}}_{\lambda L, q}$ are the spherical components of the nuclear multipole moment operator $\hat{\mathcal{M}}_{\lambda L}$ and corresponding electronic coupling operator $\hat{\mathcal{T}}_{\lambda L}$, respectively. Here λ denotes the type of the operator (electric or magnetic). If a particular type is considered, we depict it explicitly by the letter E or M. The quantum numbers L and q reflect the multipolarity of the interaction and the corresponding magnetic quantum number, respectively. Given that the hyperfine mixing is small, the states before and after IC can be represented as the products of the nuclear and electronic parts

$$
\begin{aligned}
|\alpha_m I_m N_m; \beta_i J_i M_i\rangle &= |\alpha_m I_m N_m\rangle |\beta_i J_i M_i\rangle \,, \\
|\alpha_g I_g N_g; \beta_f J_f M_f, \vec{p} m_s\rangle &= |\alpha_g I_g N_g\rangle |\beta_f J_f M_f, \vec{p} m_s\rangle \,.
\end{aligned}
\tag{1.2}
$$

Here I and N are the quantum numbers of the nuclear spin and the spin projection in the excited (m) or the ground (g) state, and the generic notation α stands for the remaining quantum numbers characterizing the nuclear state. The quantum numbers J and M are the total angular momentum and its projection for the electronic shell in the initial (i) or the final (f) state and the rest of relevant quantum numbers for the electronic shell are collected under the label β. The final continuum state of the IC electron is characterized by its momentum $\vec{p}$ and spin projection m_s.

The IC rate can be expressed via the matrix elements of the coupling operator $\hat{H}_{\text{int}}$

with Fermi's golden rule as

$$
\begin{aligned}
\Gamma_{\text{IC}} \quad &= \quad \frac{2\pi}{(2I_m+1)(2J_i+1)} \\
&\times \sum_{N_m,M_i,N_g,M_f,m_s} \int d\hat{p} \left| \langle \alpha_g I_g N_g; \beta_f J_f M_f, \vec{p}m_s | \, \hat{H}_{\text{int}} \, | \alpha_m I_m N_m; \beta_i J_i M_i \rangle \right|^2 ,
\end{aligned}
\tag{1.3}
$$

where we average over the initial states with different magnetic quantum numbers and sum over the final states with integration over all possible directions of the outcoming IC electron, depicted by the vector $\hat{p} = \vec{p}/p$. Written in this form, Fermi's golden rule does not include the density of final states, but at the same time the wave function for the continuum electron is normalized with respect to energy [see (1.9)]. After substitution of (1.1) and (1.2) the sum (integral) in (1.3) reduces to the sum (integral) of the products of the nuclear and electronic matrix elements of the form $\langle \alpha_g I_g N_g | \, \hat{\mathcal{M}}_{\lambda L,q} \, | \alpha_m I_m N_m \rangle$ and $\langle \beta_f J_f M_f, \vec{p}m_s | \, \hat{\mathcal{T}}_{\lambda L,q} \, | \beta_i J_i M_i \rangle$. Using the Wigner-Eckart theorem, the nuclear matrix element can be represented as the product of the corresponding reduced matrix element (RME) and Clebsch-Gordan coefficient [39]

$$
\langle \alpha_g I_g N_g | \, \hat{\mathcal{M}}_{\lambda L,q} \, | \alpha_m I_m N_m \rangle = (-1)^{I_m - N_m} \frac{\langle \alpha_g I_g \| \, \hat{\mathcal{M}}_{\lambda L} \, \| \alpha_m I_m \rangle}{\sqrt{2L+1}} \, C^{I_g \ I_m \ L}_{N_g - N_m \, q} .
\tag{1.4}
$$

For the Clebsch-Gordan coefficients corresponding to the coupling of the angular momenta j_1 and j_2 to the angular momentum j we use the notation $C^{j_1 \ j_2 \ j}_{m_1 m_2 m}$, where m_1, m_2 and m are corresponding magnetic quantum numbers. Instead of the nuclear RME, the so-called reduced transition probability $B^L_\downarrow$ is commonly used. Considering the definition of the operator $\hat{\mathcal{M}}_{\lambda L}$ used here (see Appendix A), $B^L_\downarrow$ is defined as [30]

$$
B^{\lambda L}_\downarrow = \frac{2L+1}{4\pi} \cdot \frac{\left| \langle \alpha_g I_g \| \, \hat{\mathcal{M}}_{\lambda L} \, \| \alpha_m I_m \rangle \right|^2}{2I_m + 1} .
\tag{1.5}
$$

For the electronic matrix element, we neglect the coupling of the angular moment of the IC electron and the remaining ion and assume

$$
| \beta_f J_f M_f, \vec{p}m_s \rangle = | \beta_f J_f M_f \rangle \, | \vec{p}m_s \rangle .
\tag{1.6}
$$

For the plane wave we make use of the expansion in partial waves [40]

$$
| \vec{p}m_s \rangle = \sum_{\kappa m} i^l e^{i\Delta_\kappa} \sum_{m_l} Y^*_{lm_l}(\hat{p}) \, C^{l \ \frac{1}{2} \ j}_{m_l m_s m} \, | \varepsilon \kappa m \rangle ,
\tag{1.7}
$$

where ε is the IC electron energy, j and m are the quantum numbers of the total angular momentum and its projection, l and m_l represent the orbital angular momentum and its projection, and the relativistic quantum number κ is defined as

$$
\kappa = \begin{cases} l, & \text{if } j = l - \frac{1}{2} , \\ -l - 1, & \text{if } j = l + \frac{1}{2} . \end{cases}
\tag{1.8}
$$

The phase factors Δ_κ are chosen such that in the asymptotic $r \to \infty$ the wave function $| \vec{p}m_s \rangle$ represents the outgoing plane wave. We do not specify them here as they are not relevant for the IC rate. The wave functions $| \varepsilon \kappa m \rangle$ are normalized with respect to the

variable ε as

$$\langle \varepsilon' \kappa m | \varepsilon \kappa m \rangle = \delta(\varepsilon' - \varepsilon) \,, \tag{1.9}$$

where $\delta(x)$ is the Dirac delta-function for the continuous variable x. The wave function $|\vec{p} m_s\rangle$ is then also energy-normalized

$$\langle \vec{p}' m_s | \vec{p} m_s \rangle = \delta(\varepsilon' - \varepsilon) \delta(\hat{p}' - \hat{p}) \,, \tag{1.10}$$

as required for Fermi's golden rule in the form (1.3). The partial wave expansion reduces the electronic matrix element to the sum of matrix elements of the form

$$\langle \beta_f J_f M_f, \varepsilon \kappa m | \hat{\mathcal{T}}_{\lambda L, q} | \beta_i J_i M_i \rangle \ .$$

We consider this matrix element in a few particular cases of the electronic configuration.

One-electron case

We start from IC in the case of one electron above closed shells. The state of the electronic shell is then fully characterized by the state of this electron $|n_i \kappa_i m_i\rangle$, where n_i is its principal quantum number, κ_i is the relativistic quantum number defined as (1.8), and m_i is the quantum number of the total angular momentum projection. The electronic matrix element for a partial wave $|\varepsilon \kappa m\rangle$ takes the form $\langle \varepsilon \kappa m | \hat{\mathcal{T}}_{\lambda L, q} | n_i \kappa_i m_i \rangle$ and can be written with the help of the Wigner-Eckart theorem [39] as

$$\langle \varepsilon \kappa m | \hat{\mathcal{T}}_{\lambda L, q} | n_i \kappa_i m_i \rangle = (-1)^{L - j_i + j} \frac{\langle \varepsilon \kappa \| \lambda \hat{\mathcal{T}}_L \| n_i \kappa_i \rangle}{\sqrt{2j + 1}} C^{L \, j_i \ j}_{q \, m_i m} \,. \tag{1.11}$$

The total matrix element becomes then

$$\langle \alpha_g I_g N_g; \vec{p} m_s | \hat{H}_{\text{int}} | \alpha_m I_m N_m; n_i \kappa_i m_i \rangle = \sum_{L\kappa} (-1)^{L - j_i + j + I_m - N_m} i^l e^{i\Delta_\kappa}$$
$$\times \frac{\langle \alpha_g I_g \| \hat{\mathcal{M}}_{\lambda L} \| \alpha_m I_m \rangle \langle \varepsilon \kappa \| \hat{\mathcal{T}}_{\lambda L} \| n_i \kappa_i \rangle}{\sqrt{(2L + 1)(2j + 1)}} \tag{1.12}$$
$$\times \sum_{m_l m_s m q} (-1)^q \, C^{I_g \ I_m \ L}_{N_g -N_m q} \, C^{L \ j_i \ j}_{-q m_i m} \, C^{l \ \frac{1}{2} \ j}_{m_l m_s m} Y^*_{l m_l}(\hat{p}) \,.$$

Substituting (1.12) in (1.3) and using the orthogonality relations for spherical functions and Clebsch-Gordan coefficients we obtain the following expression for the IC rate

$$\Gamma_{\text{IC}} = \frac{2\pi}{(2I_m + 1)(2j_i + 1)} \sum_{\lambda L, \kappa} \frac{\left| \langle \alpha_g I_g \| \hat{\mathcal{M}}_{\lambda L} \| \alpha_m I_m \rangle \langle \varepsilon \kappa \| \hat{\mathcal{T}}_{\lambda L} \| n_i \kappa_i \rangle \right|^2}{2L + 1} \,. \tag{1.13}$$

As shown in Appendix C, the electronic RME for different types of the operator $\hat{\mathcal{T}}_{\lambda L}$ is given by the expressions

$$
\langle \varepsilon \kappa \| \hat{\mathcal{T}}_{EL} \| n_i \kappa_i \rangle = (-1)^{L+\frac{1}{2}-j_i} \Pi_{l+l_i+L} \sqrt{(2j_i+1)(2j+1)}
$$
$$
\times \begin{pmatrix} j_i & j & L \\ \frac{1}{2} & -\frac{1}{2} & 0 \end{pmatrix} R_{\varepsilon\kappa}^{EL} , \tag{1.14}
$$

$$
\langle \varepsilon \kappa \| \hat{\mathcal{T}}_{ML} \| n_i \kappa_i \rangle = (-1)^{L+\frac{1}{2}+j_i} \Pi_{l+l_i+L+1} \frac{\sqrt{(2j_i+1)(2j+1)}}{L}
$$
$$
\times (\kappa_i + \kappa) \begin{pmatrix} j_i & j & L \\ \frac{1}{2} & -\frac{1}{2} & 0 \end{pmatrix} R_{\varepsilon\kappa}^{ML} , \tag{1.15}
$$

where the function Π is defined as

$$
\Pi_k = \begin{cases} 1, & \text{for even } k , \\ 0, & \text{for odd } k , \end{cases} \tag{1.16}
$$

and assures the proper parity for the electronic states. The electronic radial integrals $R_{\varepsilon\kappa}^{EL}$ and $R_{\varepsilon\kappa}^{ML}$ are given by

$$
R_{\varepsilon\kappa}^{EL} = \int_0^\infty \frac{dr}{r^{L+1}} \left(P_{n_i\kappa_i}(r) P_{\varepsilon\kappa}(r) + Q_{\varepsilon\kappa}(r) Q_{n_i\kappa_i}(r) \right) , \tag{1.17}
$$

$$
R_{\varepsilon\kappa}^{ML} = \int_0^\infty \frac{dr}{r^{L+1}} \left(P_{n_i\kappa_i}(r) Q_{\varepsilon\kappa}(r) + P_{\varepsilon\kappa}(r) Q_{n_i\kappa_i}(r) \right) , \tag{1.18}
$$

where $P_{\gamma\kappa}$ and $Q_{\gamma\kappa}$ are the radial wave functions of the initial (bound) and final (continuum) one-electron states, respectively. The total wave function for the electron is given by

$$
|\gamma \kappa m\rangle = \frac{1}{r} \begin{pmatrix} P_{\gamma\kappa}(r) \Omega_{\kappa m}(\hat{r}) \\ iQ_{\gamma\kappa}(r) \Omega_{-\kappa m}(\hat{r}) \end{pmatrix} , \tag{1.19}
$$

where the functions $\Omega_{\kappa m}(\hat{r})$ of the argument $\hat{r} = \vec{r}/r$ are the spherical spinors. The generic notation γ stands for the principal quantum number n for bound electron orbitals and for the continuum electron energy ε for free electron wave-functions, respectively. Using (1.13)—(1.15) and (1.5), we obtain finally the IC rate

$$
\Gamma_{\text{IC}}^{EL} = 8\pi^2 \sum_L \frac{B_\downarrow^{EL}}{(2L+1)^2} \sum_\kappa \Pi_{l+l_i+L} (2j+1) \begin{pmatrix} j_i & j & L \\ \frac{1}{2} & -\frac{1}{2} & 0 \end{pmatrix}^2 \left| R_{\varepsilon\kappa}^{EL} \right|^2 , \tag{1.20}
$$

$$
\Gamma_{\text{IC}}^{ML} = 8\pi^2 \sum_L \frac{B_\downarrow^{ML}}{L^2(2L+1)^2} \sum_\kappa \Pi_{l+l_i+L+1} (2j+1)(\kappa_i+\kappa)^2 \begin{pmatrix} j_i & j & L \\ \frac{1}{2} & -\frac{1}{2} & 0 \end{pmatrix}^2 \left| R_{\varepsilon\kappa}^{ML} \right|^2 . \tag{1.21}
$$

Configuration $6d^2 7s^2$

We consider at this point the configuration $6d^2 7s^2$ for the initial electronic state. The electronic shells lying in energy below the shells $6d$ and $7s$ we assume to be closed. On the one hand, this configuration is an important case as it corresponds to a Th atom in the ground state. On the other hand, it allows us to demonstrate a calculation of the IC rates for a many-electron system. We write the electronic states in second quantization

with fermionic creation (annihilation) operators $a^\dagger$ (a) and the vacuum $|0\rangle$ corresponding to the closed core of Rn-like ion Th^{4+} (see e.g. [41]). The normalized wave-function in the LS-coupling is

$$|\beta_i J_i M_i\rangle = \frac{1}{\sqrt{2}} \sum_{m_\bullet \mu_\bullet} C^{2\ 2\ L_i}_{m_a m_b m_i} C^{\frac{1}{2}\ \frac{1}{2}\ S_i}_{\mu_a \mu_b \mu_i} C^{L_i\ S_i\ J_i}_{m_i \mu_i M_i} a^\dagger_{m_a \mu_a} a^\dagger_{m_b \mu_b} a^\dagger_{\frac{1}{2}} a^\dagger_{-\frac{1}{2}} |0\rangle \ , \qquad (1.22)$$

where the dot near the summation index $\gamma_\bullet$ means summation over all indices γ having different subscripts (including the case when there is no subscript). Here the orbital momenta and the spins of the d-electrons are coupled first to the orbital momentum L_i and the spin S_i respectively, which in turn are coupled to the total angular momentum J_i. Note that the $7s$-shell in this state is closed and its presence can be depicted just by the product of creation operators with possible magnetic quantum numbers $a^\dagger_{\frac{1}{2}} a^\dagger_{-\frac{1}{2}}$. As will be shown later, in a Th atom IC takes place predominantly via conversion of a $7s$-electron, so the electronic state of the Th$^+$ ion after IC has the configuration $6d^2 7s$. The corresponding normalized wave function is

$$|\beta_f J_f M_f\rangle = \frac{1}{\sqrt{2}} \sum_{m_\bullet \mu_\bullet} C^{2\ 2\ L_f}_{m_a m_b m_f} C^{\frac{1}{2}\ \frac{1}{2}\ S_0}_{\mu_a \mu_b \mu_0} C^{S_0\ \frac{1}{2}\ S_f}_{\mu_0 \mu \mu_f} C^{L_f\ S_f\ J_f}_{m_f \mu_f M_f} a^\dagger_{m_a \mu_a} a^\dagger_{m_b \mu_b} a^\dagger_\mu |0\rangle \ . \quad (1.23)$$

The latter operator $a^\dagger_\mu$ creates a $7s$-electron with magnetic quantum number μ. The $7s$-shell is open now, so there is another intermediate spin S_0 in the coupling.

The operator $\hat{\mathcal{T}}_{\lambda L, q}$ in second quantization has the form

$$\hat{\mathcal{T}}_{\lambda L, q} = \sum_{\nu \kappa' m'} \int d\varepsilon' \langle \varepsilon' \kappa' m'| \hat{\mathcal{T}}_{\lambda L, q} |7s, \nu\rangle a^\dagger_{\varepsilon' \kappa' m'} a_\nu \ . \qquad (1.24)$$

The operator $a^\dagger_{\varepsilon' \kappa' m'}$ creates an electron in the continuum state $|\varepsilon' \kappa' m'\rangle$ and a_ν annihilates an electron with magnetic quantum number ν in the $7s$-shell. Taking into account (1.22)—(1.24), we obtain the electronic matrix element for the partial wave $|\varepsilon \kappa m\rangle$ in the form

$$\langle \beta_f J_f M_f, \varepsilon \kappa m| \hat{\mathcal{T}}_{\lambda L, q} |\beta_i J_i M_i\rangle = \delta_{L_i L_f} \delta_{S_i S_0} \sum_{m_\bullet \mu_\bullet} C^{L_f\ S_i\ J_i}_{m_i \mu_i M_i} C^{S_i\ \frac{1}{2}\ S_f}_{\mu_i \mu \mu_f} C^{L_f\ S_f\ J_f}_{m_i \mu_f M_f} \quad (1.25)$$

$$\times \sum_{\nu \kappa' m'} \int d\varepsilon' \langle 0| a_{\varepsilon \kappa m} a_\mu a^\dagger_{\varepsilon' \kappa' m'} a_\nu a^\dagger_{\frac{1}{2}} a^\dagger_{-\frac{1}{2}} |0\rangle \langle \varepsilon' \kappa' m'| \hat{\mathcal{T}}_{\lambda L, q} |7s, \nu\rangle \ .$$

The matrix element of the creation and annihilation operators' product can be simplified as

$$\langle 0| a_{\varepsilon \kappa m} a_\mu a^\dagger_{\varepsilon' \kappa' m'} a_\nu a^\dagger_{\frac{1}{2}} a^\dagger_{-\frac{1}{2}} |0\rangle = \delta(\varepsilon - \varepsilon') \delta_{\kappa \kappa'} \delta_{mm'} \left(\delta_{\mu, \frac{1}{2}} \delta_{\nu, -\frac{1}{2}} - \delta_{\mu, -\frac{1}{2}} \delta_{\nu, \frac{1}{2}} \right) \qquad (1.26)$$

$$= \sqrt{2} \delta(\varepsilon - \varepsilon') \delta_{\kappa \kappa'} \delta_{mm'} C^{\frac{1}{2}\ \frac{1}{2}\ 0}_{\mu \nu 0} \ ,$$

where δ_{ab} is the Kronecker delta-symbol for the discrete variables a and b. Taking this

into account and using (1.11) for the matrix element $\langle \varepsilon' \kappa' m' | \hat{\mathcal{T}}_{\lambda L, q} | 7s, \nu \rangle$, we obtain

$$\langle \beta_f J_f M_f, \varepsilon \kappa m | \hat{\mathcal{T}}_{\lambda L, q} | \beta_i J_i M_i \rangle = \sqrt{2} \delta_{L_i L_f} \delta_{S_i S_0} (-1)^{L - \frac{1}{2} + j} \frac{\langle \varepsilon \kappa \| \hat{\mathcal{T}}_{\lambda L} \| 7s \rangle}{\sqrt{2L+1}} \qquad (1.27)$$
$$\times \sum_{m_\bullet \mu_\bullet \nu} C^{L_f S_i J_i}_{m_i \mu_i M_i} \, C^{S_i \frac{1}{2} S_f}_{\mu_i \mu \mu_f} \, C^{L_f S_f J_f}_{m_i \mu_f M_f} \, C^{\frac{1}{2} \frac{1}{2} 0}_{\mu \nu 0} \, C^{L \frac{1}{2} j}_{q \nu m} \, .$$

Using this matrix element, we find the following expressions for the IC rate

$$\Gamma^{EL}_{\mathrm{IC}} = 8\pi^2 \delta_{L_i L_f} \delta_{S_i S_0} \Lambda \sum_L \frac{B^{EL}_\downarrow}{(2L+1)^2} \sum_\kappa \Pi_{l+L} (2j+1) \begin{pmatrix} \frac{1}{2} & j & L \\ \frac{1}{2} & -\frac{1}{2} & 0 \end{pmatrix}^2 \left| R^{EL}_{\varepsilon \kappa} \right|^2 , \quad (1.28)$$

$$\Gamma^{ML}_{\mathrm{IC}} = 8\pi^2 \delta_{L_i L_f} \delta_{S_i S_0} \Lambda \sum_L \frac{B^{ML}_\downarrow}{L^2 (2L+1)^2} \sum_\kappa \Pi_{l+L+1} (2j+1)(\kappa-1)^2 \begin{pmatrix} \frac{1}{2} & j & L \\ \frac{1}{2} & -\frac{1}{2} & 0 \end{pmatrix}^2 \left| R^{ML}_{\varepsilon \kappa} \right|^2 ,$$
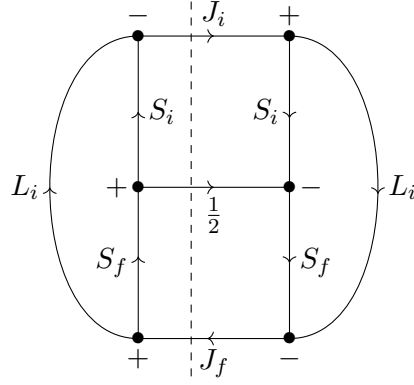$$(1.29)$$

which differ from the one-electron case by the Kronecker delta-symbols and by the additional coefficient Λ, containing the summation over the Clebsch-Gordan coefficients. The Kronecker delta-symbols impose the selection rules allowing only those final electronic states for which the subconfiguration $6d^2$ is in the same state as prior to IC. We will omit these delta-symbols in the following and will always consider only final states satisfying this condition. The coefficient Λ is defined as

$$\Lambda = \frac{1}{2J_i + 1} \sum_\bullet C^{L_i S_i J_i}_{m_i \mu_i M_i} \, C^{L_i S_i J_i}_{\widetilde{m}_i \widetilde{\mu}_i M_i} \, C^{S_i \frac{1}{2} S_f}_{\mu_i \mu \mu_f} \, C^{S_i \frac{1}{2} S_f}_{\widetilde{\mu}_i \mu \widetilde{\mu}_f} \, C^{L_i S_f J_f}_{m_i \mu_f M_f} \, C^{L_i S_f J_f}_{\widetilde{m}_i \widetilde{\mu}_f M_f} , \qquad (1.30)$$

where the summation is carried out over all magnetic quantum numbers appearing in the expression in the sum. In the graphical representation described in Appendix B, the sum in the expression (1.30) is the product of the following diagrams and numerical coefficients:
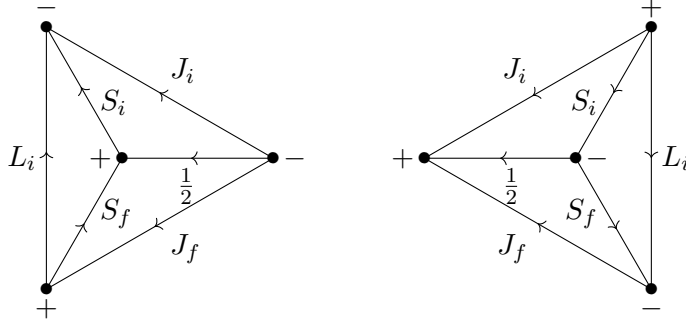

Connecting the lines with the same angular momenta we obtain the graph

with a coefficient

$$(2J_i + 1)(2J_f + 1)(2S_f + 1) \, . \tag{1.31}$$

Changing the direction of the upper and the middle line and cutting the graph as shown in the figure by the dashed line we obtain

Changing the line directions and the signs of the nodes we reduce the two graphs to the same graph representing a $6j$-symbol. The final expression for Λ is

$$\Lambda = (2J_f + 1)(2S_i + 1) \begin{Bmatrix} S_i & S_f & \frac{1}{2} \\ J_f & J_i & L_i \end{Bmatrix}^2 \, . \tag{1.32}$$

The $6j$-symbol in this expression imposes restrictions on possible values of the angular momenta, namely the four sets $(S_i, S_f, \frac{1}{2})$, (S_i, J_i, L_i), $(J_f, S_f, \frac{1}{2})$, $(J_f, J_i, \frac{1}{2})$ have to satisfy the triangle rule. As we assume $S_i = S_0$ and $L_i = L_f$, the first three conditions reflect consistency of the initial and final electronic states and are automatically fulfilled. The condition $(J_f, J_i, \frac{1}{2})$ in turn assures the angular momentum conservation in the IC process.

The expressions (1.28)—(1.29) describe the IC process for arbitrary multipolarity. As we will show later in the Chapter, for IC of a $7s$-electron in ^{229}Th we can restrict the calculation to the dominant $M1$ component. IC for a Th atom in the configuration $6d^2 7s^2$ can be thus calculated with the formula

$$\Gamma_{\mathrm{IC}} \left[6d^2 7s^2 \right] = \frac{8\pi^2}{9} \Lambda B_\downarrow^{M1} \sum_\kappa \Pi_l (2j + 1)(\kappa - 1)^2 \begin{pmatrix} \frac{1}{2} & j & 1 \\ \frac{1}{2} & -\frac{1}{2} & 0 \end{pmatrix}^2 \left| R_{\varepsilon\kappa}^{M1} \right|^2 \, . \tag{1.33}$$

Configuration $6d^3 7s$

Another important case is IC for the $6d^3 7s$ electronic configuration in a Th atom. This corresponds to a number of excited states in the Th atom, which can play a role of the

initial electronic state for the IC process. The IC takes place predominantly via conversion of a 7s-electron and has the $M1$ type. Similarly to the case of the configuration $6d^2 7s^2$ it can be shown that the IC rate is given by the expression

$$\Gamma_{\text{IC}}\left[6d^3 7s\right] = \frac{8\pi^2}{9} B_\downarrow^{M1} \sum_\kappa \Pi_l (2j+1)(\kappa-1)^2 \begin{pmatrix} \frac{1}{2} & j & 1 \\ \frac{1}{2} & -\frac{1}{2} & 0 \end{pmatrix}^2 \left| R_{\varepsilon\kappa}^{M1} \right|^2 . \qquad (1.34)$$

This expression has the same form as for the case of IC in one-electron case. It can be accounted for by the fact that IC does not break any internal coupling of the angular momenta in the initial electronic configuration. Breaking of the internal coupling can be taken into account by an additional coefficient Λ as in the case for the configuration $6d^2 7s^2$.

Closed shell

We also consider here the case of IC from a closed electronic shell, i.e., a shell where the states with all possible magnetic quantum numbers are occupied. Although it does not take place in ^{229}Th, for the nuclear excitations in the keV range it becomes the dominant case, as electrons from the inner shells are converted. It can be shown that the rate of IC from a closed shell is given by the expressions

$$\Gamma_{\text{IC}}^{EL} = 8\pi^2 (2j_i+1) \sum_L \frac{B_\downarrow^{EL}}{(2L+1)^2} \sum_\kappa \Pi_{l+l_i+L}(2j+1) \begin{pmatrix} j_i & j & L \\ \frac{1}{2} & -\frac{1}{2} & 0 \end{pmatrix}^2 \left| R_{\varepsilon\kappa}^{EL} \right|^2 , \quad (1.35)$$

$$\Gamma_{\text{IC}}^{ML} = 8\pi^2 (2j_i+1) \sum_L \frac{B_\downarrow^{ML}}{L^2 (2L+1)^2} \sum_\kappa \Pi_{l+l_i+L+1}(2j+1)(\kappa_i+\kappa)^2 \begin{pmatrix} j_i & j & L \\ \frac{1}{2} & -\frac{1}{2} & 0 \end{pmatrix}^2 \left| R_{\varepsilon\kappa}^{ML} \right|^2 ,$$
$$(1.36)$$

which differ from the expressions in the one-electron case by the factor $2j_i + 1$, where j_i is in this case the total angular momentum of the closed shell involved in IC. The appearance of this factor is natural due to the fact that a shell with the angular momentum j_i contains $2j_i + 1$ electrons increasing thus the IC rate by approx. $2j_i + 1$ times with respect to the one-electron case.

1.2 Dipole and quadrupole IC channels in ^{229}Th

The $E2$ IC channel has been widely disregarded based on calculations assuming the values for nuclear transition probabilities $B_\downarrow^{M1}$ and $B_\downarrow^{E2}$ which are obsolete today [42, 43]. Here we consider the actual values $B_\downarrow^{M1} = 0.0076$ W.u. and $B_\downarrow^{E2} = 29$ W.u. [44] and demonstrate that the contribution of the $E2$ channel is dominant or at least of the same order of magnitude for IC involving the atomic orbitals 7p, 6d and 5f, whereas for the 7s-orbital the $E2$ channel can be neglected. These results are published in our works [38, 45].

We consider the isomeric decay via IC in a neutral Th atom for different electronic configurations containing the orbitals 7s, 7p, 6d and 5f. At this point we are interested first of all in the ratio of the IC rates for the $M1$ and $E2$ channels and omit the coupling coefficient Λ (see previous Section) as it does not depend on the type of the transition. We use thus the expressions (1.20)—(1.21) for the one-electron case. We note that as the coefficient Λ is of the order of unity, the results in this Section can serve at the same time as a preliminarily estimate of the order of magnitude of the IC rates.

At this point we choose the commonly accepted value $E_m = 7.8$ eV for the nuclear transition energy. The calculation requires knowledge of electronic level energies and wave functions. The spectrum of the valence electron is taken from atomic spectroscopy database [46] which provides precise values as opposed to the limited accuracy of atomic structure calculations for atoms or ions with many electrons. The relativistic electronic wave functions for the bound electron are obtained from a multi-configurational Dirac-Hartree-Fock (DHF) method using the GRASP2K package [47]. The continuum wave functions are calculated with the program *xphoto* from the RATIP package [48] (see Chapter 4 for details).

As reported in Ref. [38], we have validated our calculation method and numerical results by comparing IC coefficients with theoretical values tabulated in the literature [49, 50] for a number of test cases. The compilations in Refs. [49, 50] use the relativistic DHF method for the calculation of electronic wave functions. In addition, Ref. [50] takes into account the effect of atomic vacancies created in the conversion process. In Fig. 1.1 we depict the calculated IC coefficients as a function of the nuclear transition energy together with data from Refs. [49, 50]. We consider a fictitious nuclear transition of multipolarity $M1$ which ionizes the $6d$- and $7s$-electronic orbitals in the neutral Th atom. In all cases good agreement with at least one of the tabulated values is achieved.
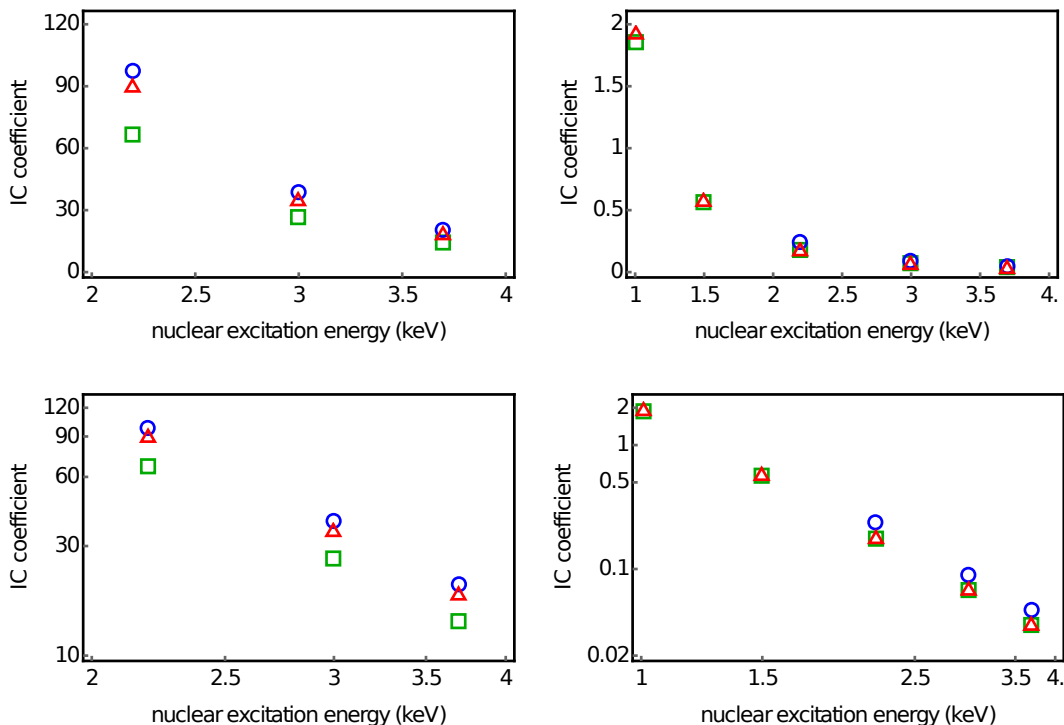
Figure 1.1: IC coefficients for the $7s$-electron (the left two graphs) and $6d$-electron (the right two graphs) of thorium calculated in the present work (red triangles), in Ref. [50] (green squares) and in Ref. [49] (blue circles) as a function of nuclear transition energy. The lower graphs present the same values on a logarithmic scale to check the expected linear slope in the IC coefficient [49].

We proceed with the IC rates calculated for different electronic shells in ^{229}Th and presented in Table 1.2. For completeness we also give the IC coefficients $\alpha_{\mathrm{IC}}^{M1}$ and $\alpha_{\mathrm{IC}}^{E2}$ calculated with respect to the corresponding γ-decay channels. Our results show that

Orbital	Γ_{IC}^{M1} (s^{-1})	α_{IC}^{M1}	Γ_{IC}^{E2} (s^{-1})	α_{IC}^{E2}	$\frac{\Gamma_{\text{IC}}^{E2}}{\Gamma_{\text{IC}}^{M1}}$
$7s$	$1.3 \cdot 10^5$	$1.1 \cdot 10^9$	$3.8 \cdot 10^2$	$4.8 \cdot 10^{15}$	$2.9 \cdot 10^{-3}$
$7p_{1/2}$	$4.2 \cdot 10^3$	$3.7 \cdot 10^7$	$5.1 \cdot 10^3$	$6.4 \cdot 10^{16}$	1.2
$7p_{3/2}$	$3.5 \cdot 10^2$	$3.0 \cdot 10^6$	$8.2 \cdot 10^3$	$1.0 \cdot 10^{17}$	23
$6d_{3/2}$	$2.3 \cdot 10^2$	$2.0 \cdot 10^6$	$3.4 \cdot 10^2$	$4.3 \cdot 10^{15}$	1.5
$6d_{5/2}$	$1.8 \cdot 10^2$	$1.6 \cdot 10^6$	$4.9 \cdot 10^2$	$6.2 \cdot 10^{15}$	2.7
$5f_{5/2}$	$1.3 \cdot 10^2$	$1.1 \cdot 10^6$	79	$1.0 \cdot 10^{15}$	0.61
$5f_{7/2}$	65	$5.7 \cdot 10^5$	61	$7.7 \cdot 10^{14}$	0.94

Table 1.2: The $M1$ and $E2$ IC rates Γ_{IC}^{M1} and Γ_{IC}^{E2}, corresponding IC coefficients α_{IC}^{M1} and α_{IC}^{E2} and the ratio of the IC rates $\Gamma_{\text{IC}}^{E2}/\Gamma_{\text{IC}}^{M1}$.

for all electronic orbitals but $7s$, the $E2$ IC channel either dominates or is comparable to the $M1$ IC channel. For the $7p_{3/2}$ orbital the rate Γ_{IC}^{E2} becomes an order of magnitude larger than Γ_{IC}^{M1}. For the $7s$ electrons, however, the IC rate for the $E2$ channel is 3 orders of magnitude smaller than the $M1$ one. This happens because the s-wave for the continuum electron, which is the largest contribution in the sum over κ in Eq. (1.20), becomes forbidden by the selection rules. Our results confirm thus that whenever the $7s$ electron is available for IC, the $M1$ IC decay channel will dominate.

1.3 IC in a neutral ^{229}Th atom

In this Section we show numerical results for IC in a Th atom and envisage the experimental scenario presented at the beginning of the Chapter. We start from the situation when the electronic shell is initially in its ground state. The IC process depends qualitatively on the energy of the isomeric state, as the energy conservation law imposes the restriction on allowed final states. The commonly accepted value for the energy of the isomer ^{229}Th is $E_m = 7.8$ eV [14, 15], but the accuracy of this value is in doubt at present [32, 43]. Moreover, another measurement resulting in $E_m = 7.1$ eV has been reported recently [51]. Due to this reason we consider here the values $E_m = 7.1$ eV, $E_m = 7.8$ eV, $E_m = 8.5$ eV and $E_m = 9.2$ eV for completeness of our analysis. For each E_m we carry out the IC calculation for every final electronic state allowed by energy conservation and selection rules. We characterize the distribution over the final states by distribution of the IC electrons by energy. For a final electronic state with the energy E_f corresponding energy of the IC electron is

$$E_e = E_m + E_i - E_f \; , \tag{1.37}$$

where E_i is the energy of the initial electronic level. As the configuration of the electronic ground state is $6d^2 7s^2$, we calculate the IC rates according to the expression (1.33). In this case and in the other IC calculations in this Section we take into account the first and the second LS-components for each electronic state. The information about the components together with their contribution in % is available in the database [46]. In Fig. 1.2 we show the IC electron spectra assuming that the Th atom is initially in the ground state. With increasing of E_m the spectrum shifts to the right and more lines appear due to opening of new IC channels. The total IC rates and corresponding half-lives for different values of E_m are shown in Table 1.3.

We proceed by considering the electronic shell of the Th atom to be excited before IC
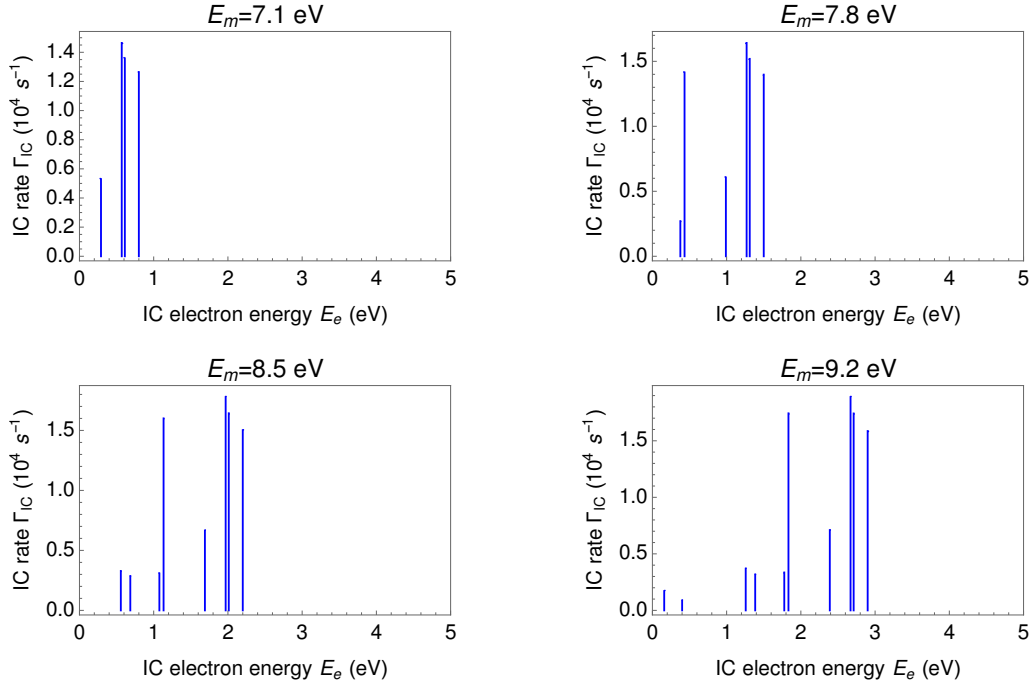
Figure 1.2: The spectra of the IC electron for different values of the isomer energy E_m. The Th atom is initially in its ground electronic state.

E_m (eV)	7.1	7.8	8.5	9.2
Γ_{IC} (10^4 s^{-1})	4.6	6.8	8.1	8.9
T_{IC} (μs)	15.0	10.1	8.5	7.7

Table 1.3: The IC rate Γ_{IC} and corresponding half-life T_{IC} for different values of the isomer energy E_m. The Th atom is initially in its ground electronic state.

occurs. In this case, either IC will take place directly from the excited electronic state or the latter decays radiatively prior to IC. Which process takes place first, is defined by the ratio of the radiative lifetime of the electronic level and the IC characteristic time. The population of excited electronic states depends strongly on the preparation procedure of the Th atom and can not be predicted in the general case. In order to facilitate the further analysis, we take into account electronic levels with energy below 20000 cm^{-1} and lifetime larger than 3 μs (the IC characteristic time is $\sim$ 10 μs). These states shown in Table 1.4 are obtained based on the energy levels database [46] and the lifetimes estimated using the GRASP2K [47] package for low-lying states and the database [52] containing relative intensities of the electric dipole radiative decay. We assume the relative populations of the levels to be $2J_i + 1$, where J_i is the total angular momentum of the electronic state.

We calculate the IC rates for the initial electronic states with the configurations $6d^2 7s^2$ and $6d^3 7s$ with the expressions (1.33) and (1.34), respectively. Analogously to the derivation in Section 1.1, it can be obtained that the same expressions can be applied correspondingly to the configurations $5f6d7s^2$ and $5f6d^2 7s$. The IC rate is evaluated via the wave functions of the continuum electron, which depend on the IC electron energy as well as the initial and the final bound electronic states. Instead of considering separately all the pairs of initial and final states, we obtain the continuum wave functions only for

J_i	Configuration	E_i (cm^{-1})	J_i	Configuration	E_i (cm^{-1})
2	$6d^27s^2$	0	5	$6d^37s$	14204.264
0	$6d^27s^2$	2558.057	0	$6d^37s$	14226.822
3	$6d^27s^2$	2869.259	6	$5f6d7s^2$	14481.869
2	$6d^27s^2$	3687.987	4	$6d^37s$	15493.221
1	$6d^27s^2$	3865.475	3	$5f6d^27s$	15618.984
4	$6d^27s^2$	4961.659	2	$6d^37s$	15863.891
1	$6d^37s$	5563.142	3	$6d^37s$	15970.095
2	$6d^37s$	6362.396	4	$5f6d^27s$	16346.651
2	$6d^27s^2$	7280.124	0	$6d^27s^2$	16351.943
3	$6d^37s$	7502.288	6	$6d^37s$	16554.245
4	$5f6d7s^2$	7795.275	4	$5f6d^27s$	16783.847
4	$6d^27s^2$	8111.005	1	$6d^37s$	17073.811
4	$6d^37s$	8800.251	5	$6d^37s$	17166.108
5	$6d^37s$	9804.807	3	$6d^37s$	17398.398
4	$5f6d7s^2$	10414.136	4	$6d^37s$	17959.898
5	$5f6d7s^2$	11197.031	5	$5f6d^27s$	18011.38
1	$6d^37s$	11601.031	2	$6d^37s$	18549.405
2	$6d^37s$	11802.934	1	$6d^37s$	18574.608
3	$6d^37s$	12847.971	6	$5f6d^27s$	19227.336
3	$6d^37s$	13088.563	4	$6d^37s$	19532.419
4	$6d^37s$	13297.434	3	$6d^37s$	19713.031
2	$6d^37s$	13847.771	0	$6d^37s$	19832.116
1	$6d^37s$	13962.522	6	$5f6d^27s$	19986.166

Table 1.4: Electronic levels of a Th atom with the energy below 20000 cm^{-1} and the lifetime exceeding 3 μs.

the configurations $6d^37s$ and $6d^27s^2$ and use them for the initial electronic levels with one and two $7s$ electrons, respectively. This approximation should affect the result only on a level of few %. In Fig 1.5 we show the obtained IC electron spectra. The total IC rates and corresponding half-lives for different E_m are given in Table 1.5.

E_m (eV)	7.1	7.8	8.5	9.2
Γ_{IC} (10^4 s^{-1})	11.4	13.1	13.9	14.5
T_{IC} (μs)	6.1	5.3	5.0	4.8

Table 1.5: The IC rate Γ_{IC} and corresponding half-life T_{IC}. The initial electronic states are the states listed in Table 1.4 and considered to be populated with probabilities proportional to $2J_i + 1$.

In Fig. 1.4 and Fig. 1.5 we represent the obtained results also in the form of so-called cumulative spectra, which refer to the experimental scheme [28, 35] described later on page 22. A stopping voltage U_s is applied to the outcoming IC electrons and those electrons which have passed through this barrier are detected. The cumulative spectrum shows the number of the passed electrons for each value of the stopping potential U_s, which equals to the number of the IC events with the continuum electron at energy exceeding the stopping energy $E_s = eU_s$, where e is the absolute value of the electron charge. The plots in Fig. 1.4 show the rates considering *only* the Th atom in the electronic ground state. If the initial electronic states are the states listed in Table 1.4
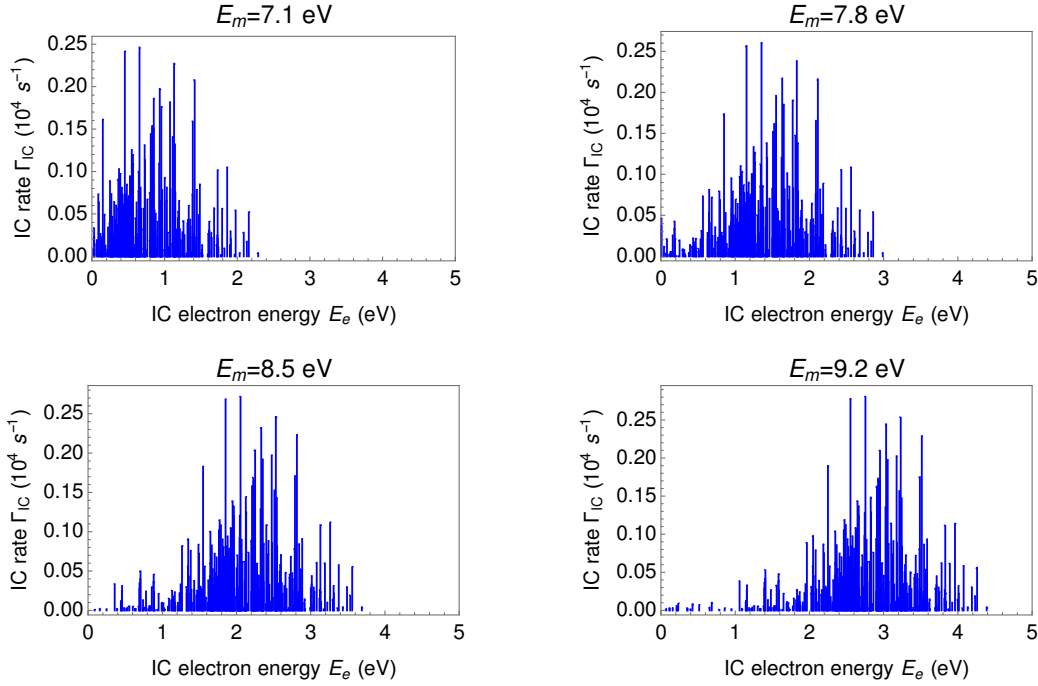
Figure 1.3: The spectra of the IC electron for different values of the isomer energy E_m. The initial electronic states are the states listed in Table 1.4 and considered to be populated with probabilities proportional to $2J_i + 1$.

populated with probabilities proportional to $2J_i + 1$, the cumulative spectra become smoother. As can be seen in Fig. 1.5, the energies of the IC electrons are concentrated within a 1-eV-width range in this case.

From Table 1.3 and Table 1.5 it appears that the IC rate depends both on the isomeric state energy and on the initial conditions. This dependence reflects the change of the distribution between the IC channels corresponding to different initial and final states. At the same time, the individual IC rates in each channel depend on E_m relatively weakly. This can be seen from Fig. 1.6, where we show the IC rates for the configurations $6d^2 7s^2$ and $6d^3 7s$ at different E_m obtained with the expressions (1.33)—(1.34) without taking into account the Λ coefficient. These rates correspond to the situation with no angular momenta couplings of the IC electron with the spectator electrons. For each considered configuration we then include the actual couplings by multiplying the generic values plotted in Fig. 1.6 with the appropriate Λ value.

At this point it is possible to make only a rough comparison of the IC rates to the experimental results [28, 29] giving $T_{IC} = 7 \pm 1$ μs, as (a) the isomeric state energy E_m is not known accurately today; (b) the initial state of the Th atom in the experiment [28] is not well defined; (c) the IC process is observed in Ref. [28] for Th atoms on the detector surface (see below) which may influence the IC rate. Nevertheless, the IC electron spectra may be helpful for determination of the actual value E_m using the IC electron spectroscopy [35], as will be explained in the following.

Experimental scheme

We describe here a possible experimental scheme for determination of the nuclear isomeric state energy E_m proposed and analyzed in Ref. [28, 35]. The scheme is based on the experimental setup used for direct detection of the nuclear transition between the
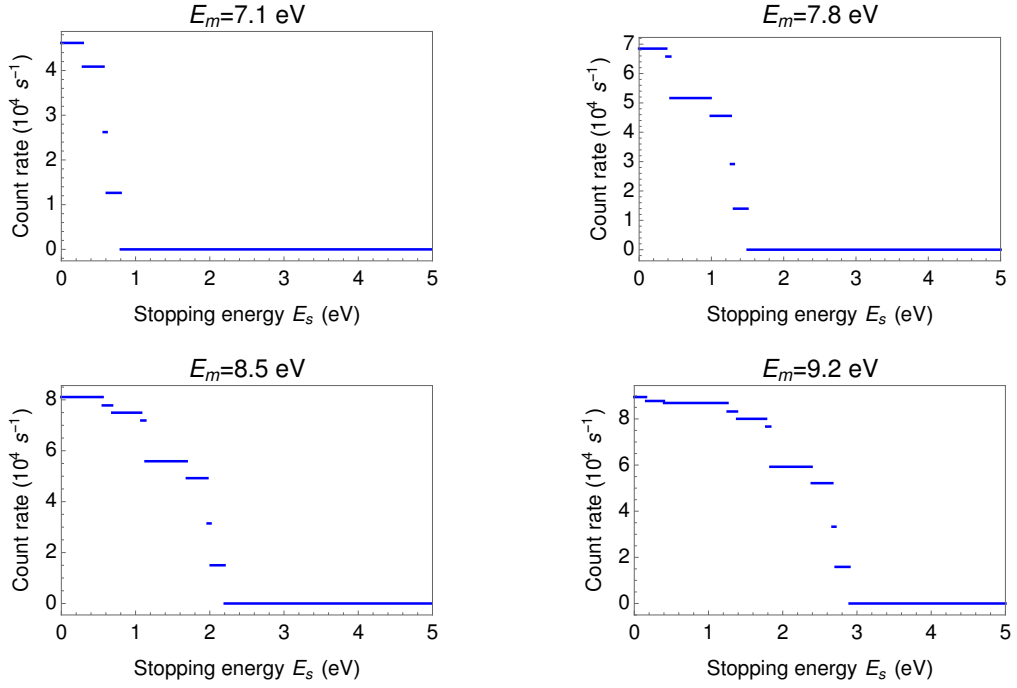
Figure 1.4: The cumulative spectra of the IC electrons for different values of the isomer energy E_m. The Th atom is initially in its ground electronic state. Compare with Fig. 1.5.
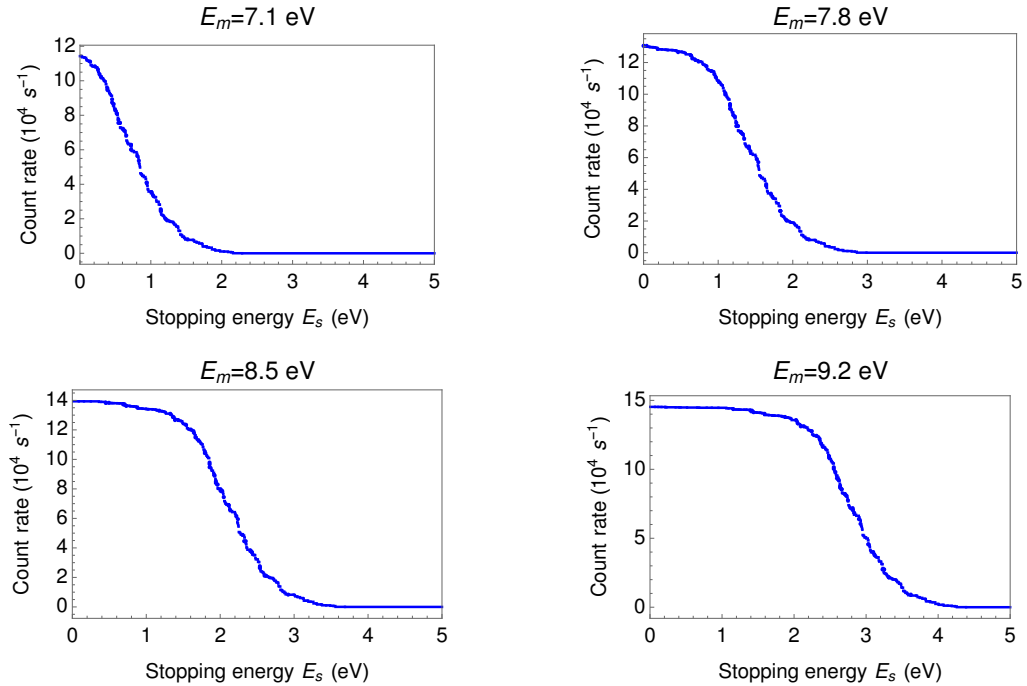

Figure 1.5: The cumulative spectra of the IC electrons for different values of the isomer energy E_m. The initial electronic states are the states listed in Table 1.4 and considered to be populated with probabilities proportional to $2J_i + 1$. Compare with Fig. 1.4.

isomeric and the ground states in a nucleus ^{229}Th [28]. The setup is illustrated in Fig 1.7 (taken from [28]). In this experiment ^{229}Th is obtained from a ^{233}U sample undergoing
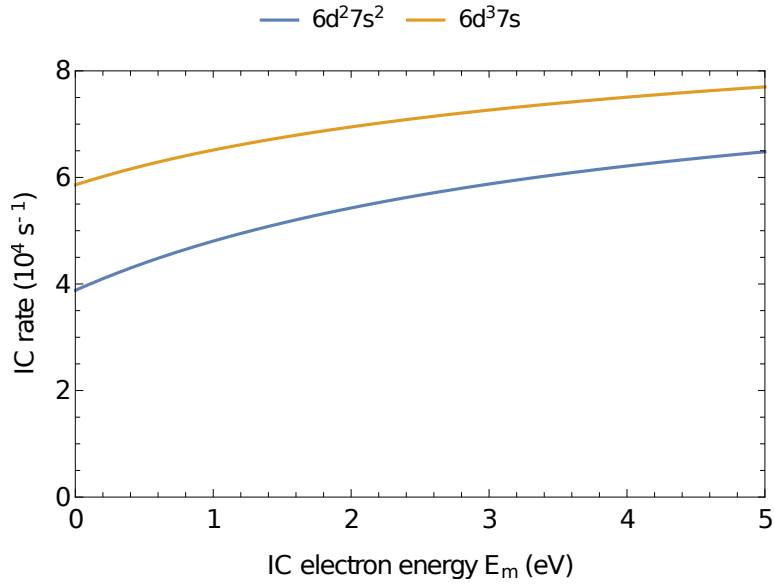
21

Figure 1.6: IC rates for for the configurations $6d^2 7s^2$ and $6d^3 7s$ obtained with the expressions (1.33)—(1.34) without taking into account the Λ coefficient.

α-decay with producing ^{229}Th recoil ions, approx. 2% of which are in the nuclear isomeric state [53, 54]. We note that this approach remains today the only reliable way for obtaining ions with the nuclear isomer ^{229m}Th. The recoil ions are guided by an electric field through a cell filled with a buffer gas, where they loose their initial kinetic energy of 84 keV. After extraction by the Laval nozzle, the ions are guided through a radio-frequency quadrupole-ion system (RFQ) towards a quadrupole mass-separator (QMS), which allows filtering out of Th ions in a particular charge states. The ions are then collected on the surface of a microchannel plate detector (MCP), where they neutralize. The nuclear isomeric state in neutral ^{229}Th decays within ~ 10 μs via IC, producing electrons which are multiplied by the MCP, accelerated towards a phosphor screen and detected by a charge-coupled device (CCD) camera. The successful detection of the IC electrons in the described experiment is considered as the first direct observation of the ^{229}Th nuclear isomeric state.
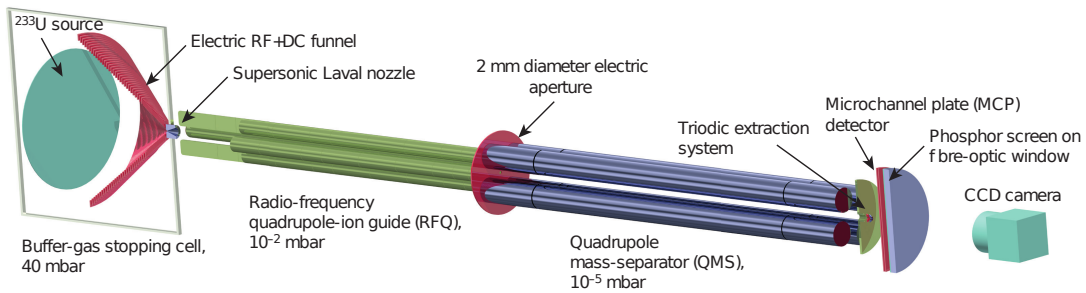
Figure 1.7: The scheme of the experimental setup used for direct detection of the nuclear transition between the isomeric and the ground states in ^{229}Th (taken from [28]).

Collecting the ions on an MCP detector does not allow to measure the kinetic energy of the IC electrons. For energy determination it is advantageous to neutralize the ions in-flight and generate free atoms decaying via IC. The IC electrons can be then collected

and guided with magnetic fields towards a retarding field electron spectrometer where a stopping potential is applied [35]. Only those electrons are detected and counted which have passed the stopping potential, that is, which have energy higher than the stopping energy eU_s. Varying the potential U_s, one can obtain a cumulative spectrum for the IC electrons and extract the energy of the isomeric state E_m by matching to the theoretical predictions. Depending on the involved neutralization process, the Th atoms can be in excited states listed in Table. 1.4. Although the electronic state prior to IC is not well defined in this experiment, we believe that the obtained cumulative spectra may allow an extraction of the value E_m due to the following reason. As our calculations have shown, the change of the population distribution between the states listed in Table. 1.4 affects the low- and high-energy parts of the spectrum, whereas the shape in the 1-eV range of the strong inflection does not change significantly if none of the initial states is preferred. The energy E_m can be then obtained by a horizontal matching of the theoretical and experimental spectra within this 1-eV range. This would allow an accurate determination of the ^{229}Th isomer energy even is spite of the lack of the experimental information on the initial electronic state.

1.4 IC from excited electronic states of ^{229}Th ions

We describe here a possible approach for characterization of the isomeric state ^{229m}Th based on the process of IC from excited electronic states of Th ions. These results were published in Ref. [38] including a proposal for a possible experimental implementation at the IGISOL facility, Jyväskylä, Finland. At the time different values for the nuclear transition probabilities $B^{M1}_\downarrow$ and $B^{E2}_\downarrow$ were considered. In this work we show the results recalculated for the newest theoretically predicted values $B^{M1}_\downarrow = 0.0076$ W.u. and $B^{E2}_\downarrow = 29$ W.u. [44].

IC is energetically allowed in the neutral atom, but should be forbidden in Th ions, as shown by the ionization potential values tabulated in Table 1.1. Thus, IC from the electronic ground state becomes energetically forbidden for higher degrees of ionization so that *only* IC from excited states remains allowed. We stress once more that this is a peculiar and rather unique situation, since for the otherwise common nuclear transition energies in the keV range, IC always occurs from the ground state. If a ^{229m}Th ion prepared in an excited electronic state undergoes IC at a rate fast enough compared with the spontaneous decay of the electronic excited state, ions of a higher charge state will be produced in the process. Detection of such ions can be performed with close-to-unity efficiency and direct comparison with the case of ^{232}Th (which does not possess any nuclear states at optical energies) will indicate the presence of the isomeric state. Based on the observation of occurring IC-induced ionization, one can estimate the isomeric energy and compare the IC rate with theoretical predictions. A schematic illustration of the IC from an excited electronic state of Th$^+$ leading to the formation of Th^{2+} ions is presented in Fig. 1.8.

In this Section we carry out the IC calculations in the jj coupling scheme for the outer electrons in contrast to Section 1.1, where the LS scheme was adopted. The advantage of relative simplicity of the LS coupling for a neutral Th atom with four valence electrons had to be compensated by taking into account a few LS-components. In the case of Th ions with not more than three valence electrons, the jj scheme leads to analogous expressions for the IC rates as we obtained in Section 1.1. One should distinguish again between the cases when the internal angular momentum coupling is conserved or broken by IC. In the first case the IC rate is non-zero only if the electronic configuration of the
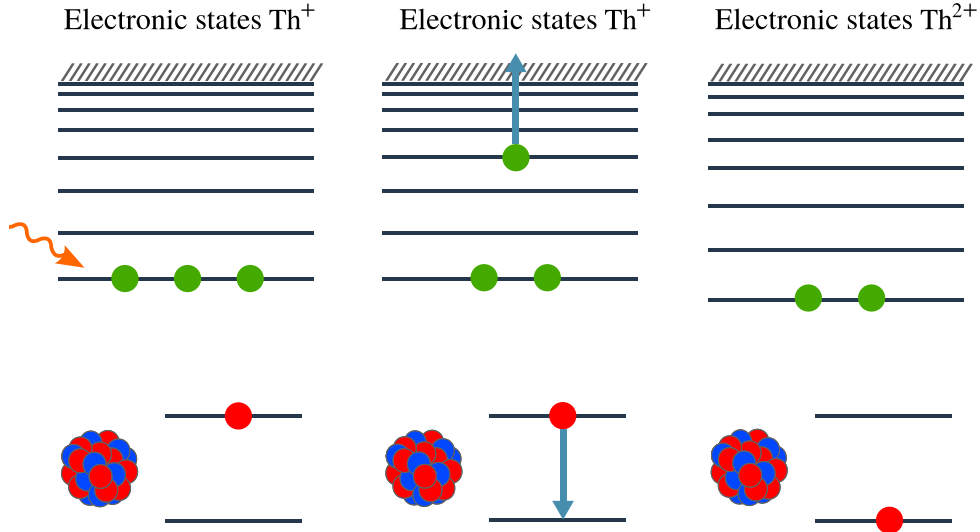
Figure 1.8: A schematic illustration of IC from an excited electronic state of Th^+ leading to the formation of Th^{2+} ions. The generic electronic level scheme of the outermost three electrons is depicted in the upper part of the figure, while the lower part illustrates the ground and isomeric nuclear states. Photoexcitation creates the excited electronic state in Th^+ (left graph). This opens the IC channel for the isomeric state, such that an electron is ionized (middle graph) producing Th^{2+} ions (right graph).

spectator electrons remains the same in the IC process. Breaking of the initial coupling possible only for three electrons in the outer shell should be taken into account by the equivalent of the Λ-coefficient in Eq. (1.30), now given by the expression

$$\Lambda = (2J_0 + 1)(2J_f + 1) \begin{Bmatrix} j_1 & j_2 & J_f \\ j_i & J_i & J_0 \end{Bmatrix}^2 , \qquad (1.38)$$

where J_f is the total angular momentum of the final electronic state and the initial electronic configuration consists of electrons with individual total angular momenta j_1, j_2, j_i (the latter denoting the electron which undergoes IC) such that

- j_2, j_i are first coupled to the momentum J_0;

- J_0 and j_1 are then coupled to the total momentum J_i.

We analyze possible excited states as candidates for the initial IC configuration assuming that the value of E_m may also lie outside the range 7.8 ± 0.5 eV. As upper limit we choose 20.0 eV which is the ionization potential of Th^{2+}. Comparing the IC rates and the rates of radiative decay for the electronic levels, we show that this detection scheme is applicable for Th^+ in the case when E_m lies between approx. 9.0 and 12.0 eV, while Th^{2+} can be used only in the rather unlikely case that E_m is higher than 19.1 eV, but less than 20.0 eV.

We now proceed with numerical results for IC from excited electronic states of Th^+ and Th^{2+}. In the following Tables we list the calculated total IC rates for a number of relevant cases. The minimum isomeric energy required for the respective IC channel to be open is labeled as E_m^{min}. In particular we focus on Th^+ configurations and two Th^{2+} excited states that are of interest for the experimental investigation of the electron bridge process [34, 55]. We present the IC rate as a function of the possible nuclear isomeric

state energy and take into account all available final states within the considered energy range. Note that the number of digits to represent the IC rates is chosen in each case to be sufficient to depict the dependence of the result on the isomeric state energy within the framework of the calculation model. With increasing charge state, the required electronic excitation and ionization energies are also increasing. Thus, we note that due to the large ionization potential of Th^{2+}, the required isomeric energy to render IC from the chosen excited electronic configuration is approx. 19 eV, which is according to present knowledge highly unlikely. We conclude that the most interesting ionization state for IC from an excited electronic state is Th^+.

Results for Th^+

The choice of the excited states is unfortunately limited by the available electronic energy data in the experimental database [46] and by the short radiative lifetimes of the excited states. Based on the radiative decay rates calculated with the GRASP2K package [47], we choose to consider two suitable initial excited electronic states: $5f6d^2$ at 30223 cm^{-1} with $J = 15/2$ and the $7s^27p$ at 31626 cm^{-1} with $J = 1/2$. In Table 1.6 we show the calculated radiative lifetimes for the excited electronic states of interest for the IC schemes in Th^+ and Th^{2+}. The IC rates for the two configurations in Th^+ are presented in Tables 1.7 and 1.8. The excited state $5f6d^2$ has no electric-dipole decay channels; its calculated radiative lifetime is 0.4 s. IC from the $5f6d^2$ state becomes possible provided that the isomeric state energy would be higher than 9.0 eV, in which case the characteristic decay time becomes considerably shorter than the level lifetime. Provided that the isomeric energy indeed lies higher than 7.8 eV as speculated at present, this opportunity seems to be unique, as the other states at such high excitation energies typically decay very fast (see Table 1.6, the case for the $7s^27p$ state at 31626 cm^{-1}). On the other hand, in case the isomer energy is higher than 12 eV, the excitation method would no longer be applicable since the ground state $6d^27s$ electrons could undergo IC. We are therefore focusing on the range of 9.0 eV to 12.0 eV isomeric state energy. We note here that the laser excitation of this particular electronic configuration is not straightforward due to the large difference of its total angular momentum and the angular momentum of the ground state: $\frac{15}{2} - \frac{3}{2} = 6$. Several possible experimental approaches are addressed in the following.

A graphical representation of the values in Table 1.7 is given in Fig. 1.9. We depict the IC rates for the initial $5f6d^2$ state as a function of the possible nuclear isomeric state energy and take into account all available final states within the considered energy range. The step-like jumps represent openings of new channels of decay corresponding to different electronic states of the final ion Th^{2+}.

Ion charge	Configuration	Energy (cm^{-1})	Lifetime
1+	$5f6d^2$	30223	0.4 s
	$7s^27p$	31626	40 ns
2+	$5f7s$	7501	20 μs
	$6d7s$	16038	100 ns

Table 1.6: Lifetimes of the considered excited electronic states.

Final state		$E_m^{\min}$ (eV)	E_m (eV)	Rate (s^{-1})		
Config.	E (cm^{-1})			$M1$	$E2$	Total
6d^2	6538	9.2	9.2	41	38	80
			9.5	41	38	79
			10.0	41	37	78
			10.5	40	36	77
			11.0	40	35	75
			11.5	39	35	75
	10543	9.7	9.7	38	40	78
			10.0	37	39	76
			10.5	37	38	75
			11.0	36	37	74
			11.5	36	37	73
5f6d	4490	9.0	9.0	37	96	133
			9.5	38	101	140
			10.0	40	106	146
			10.5	41	112	153
			11.0	43	116	159
			11.5	44	121	165
	8437	9.4	9.4	225	405	630
			10.0	224	407	631
			10.5	223	408	631
			11.0	223	409	631
			11.5	222	410	632
	11277	9.8	9.8	35	121	156
			10.0	36	122	158
			10.5	38	126	164
			11.0	40	130	170
			11.5	42	133	175
	19010	10.8	10.8	54	159	213
			11.0	54	161	215
			11.5	56	164	220

Table 1.7: Internal conversion rates for the state $5f6d^2$ at 30223 cm^{-1} in Th$^+$. The total angular momentum of this state is $J = 15/2$.

Results for Th^{2+}

With increasing charge state, the required electronic excitation is also increasing in energy. The value of E_m at which one can apply the same method for Th^{2+} lies in the range from 19.1 eV to 20.0 eV (the Th^{2+} ionization potential). Due to the relatively simple structure of the Th^{2+} spectrum, there is no opportunity for a highly excited state to not decay through fast $E1$ transitions. However, if E_m is close enough to the Th^{2+} ionization threshold such that the excited level does not have to be very high in order to observe IC, one can expect moderate $E1$ decay rates due to their proportionality to the third power of the photon frequency. On the other hand, we can choose a level undergoing IC at a rate high enough to compete with the $E1$ decay.

We consider two levels of Th^{2+}, namely $5f7s$ at 7501 cm^{-1} and $6d7s$ at 16038 cm^{-1}. IC from these states becomes energetically allowed at the lowest values of E_m among the other states (19.1 eV and 19.2 eV, respectively). The calculated rate of IC from the

Final state		$E_m^{\min}$ (eV)	E_m (eV)	Rate (s^{-1})		
Config.	E (cm^{-1})			$M1$	$E2$	Total
$7s^2$	11961	9.7	9.7	7410	9221	16631
			10.0	7435	9247	16682
			10.5	7474	9288	16762
			11.0	7512	9329	16841
			11.5	7548	9369	16917

Table 1.8: Internal conversion rates for the state $7s^27p$ at 31626 cm^{-1} in Th$^+$. The total angular momentum of this state is $J = 1/2$.
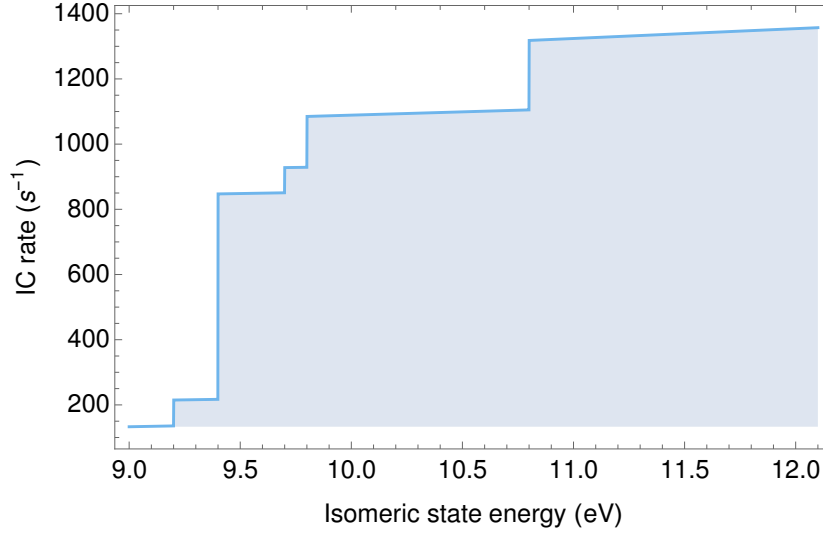

Figure 1.9: Internal conversion rates for the state $5f6d_2$ at 30223 cm^{-1} of Th$^+$. For comparison, the half-life of the electronic excited state was calculated to be 0.4 s.

level at 7501 cm^{-1} is equal to 10^5 s^{-1} and is twice higher than the radiative decay rate $5 \cdot 10^4$ s^{-1} calculated with GRASP2K, see Table 1.6. The rate of IC from the state at 16038 cm^{-1} is calculated to be $3 \cdot 10^4$ s^{-1} and is at least two orders of magnitude less than the radiative decay of 10^7 s^{-1}, see Tables 1.9 and 1.10. It is worth noting that the difference of angular momenta between the level $5f7s$ at 7501 cm^{-1} and the ground state equals $4 - 3 = 1$ and, contrary to the case of Th$^+$, this allows a more straightforward excitation scheme.

Final state		$E_m^{\min}$ (eV)	E_m (eV)	Rate (s^{-1})		
Config.	E (cm^{-1})			$M1$	$E2$	Total
$5f$	0	19.1	19.1	101583	107	101690
			19.5	101595	107	101702
			19.9	101608	107	101715

Table 1.9: Internal conversion rates for the state $5f7s$ at 7501 cm^{-1} in Th^{2+}. The total angular momentum of this state is $J = 3$.

The IC process considered in this Section involves the $7s$-, $7p$-, $6d$- and $5f$-orbitals. The calculated IC rates confirm again that the $E2$ channel can be safely neglected only in the case of IC for a $7s$-electron.

Final state		$E_m^{\min}$ (eV)	E_m (eV)	Rate (s^{-1})		
Config.	E (cm^{-1})			$M1$	$E2$	Total
			19.2	28428	27	28455
$6d$	9193	19.2	19.5	28435	27	28462
			19.9	28444	27	28471

Table 1.10: Internal conversion rates for the state $6d7s$ at 16038 cm^{-1} in Th^{2+}. The total angular momentum of this state is $J = 2$.

Possible methods to excite the *5f6d*^{2} level of Th$^+$ at 30223 cm^{-1}

The experimental population of the $5f6d^2$ state of Th$^+$ at 30223 cm^{-1} is, at first sight, not straightforward due to the difference of the total angular momentum with respect to the ground state: $\frac{15}{2} - \frac{3}{2} = 6$. In addition, if one were to excite from the ground state using six resonant photon transitions, one also needs to introduce a change in parity, that is one of these transitions would need to have $M1$ multipolarity. In the following we therefore consider other possible ways to reach the level.

Firstly, the state of interest can be reached via three $E1$ excitation/de-excitation steps from the $6d^27s$ excited level at 6213 cm^{-1} as indicated in the possible laser excitation scheme in Fig. 1.10. The levels at 30310 cm^{-1} and 42645 cm^{-1} can serve as intermediate stages, so that one can use two laser excitations with wavelengths of 415 nm and 811 nm, followed by one induced de-excitation at 805 nm. All of the wavelengths are easily produced using Ti:sapphire lasers [56], one of which is frequency doubled. The $6d^27s$ state at 6213 cm^{-1} has only one $E1$ decay channel at the extremely low photon energy of $5.6 \cdot 10^{-3}$ eV and very low decay rate of 10^{-4} s^{-1}, so it can be considered as metastable.

The electronic level at 6213 cm^{-1} has a total angular momentum 9/2 and even parity. It can be reached with four laser (de)excitations in the following manner: an excitation from the ground state to an odd parity 3/2 level at 26965 cm^{-1} (371 nm), a second excitation step to an even parity 5/2 state at 40644 cm^{-1} (731 nm), a stimulated de-excitation to an odd parity 7/2 state at 18974 cm^{-1} (461 nm) and finally a de-excitation to the even parity 9/2 level at 6213 cm^{-1} (784 nm), all of which are suitable for Ti:sapphire lasers. Nevertheless, such an excitation scheme would require 4 different lasers and though possible, subsequent optical excitation from the metastable level towards the state of interest at 30223 cm^{-1} is simply impractical.

Alternative means to populate the 6213 cm^{-1} state will require experimental investigation and thus we simply highlight them here:

- Following the α-decay of a source of ^{233}U (which proceeds, following gamma-ray de-excitation, primarily to the ground state of ^{229}Th with a 2% branching to the low-energy isomeric state [53, 54]) the ^{229}Th recoils may be stopped in a buffer gas cell [28, 57]. Excitation of the 6213 cm^{-1} state may occur via collisions in the gas cell;

- Excitation of the nuclear isomeric state of the ion ^{229}Th$^+$ through an electron bridge scheme chosen such that the final electronic level is not the ground state, but the state at 6213 cm^{-1} (this would work for particular values of E_m);

- Thermal excitation to the metastable level via laser ablation of ^{229}Th from a dried thorium nitrate solution deposited on a tungsten or tantalum substrate. This has recently been realized for the study of isotope shifts and hyperfine structures of resonance lines in ^{229}Th$^+$, with a low pressure argon buffer gas used to cool the

ions to room temperature and quench the population of metastable states optically pumped by the laser excitation [58]. In the current proposal however population of the metastable state is a requirement.
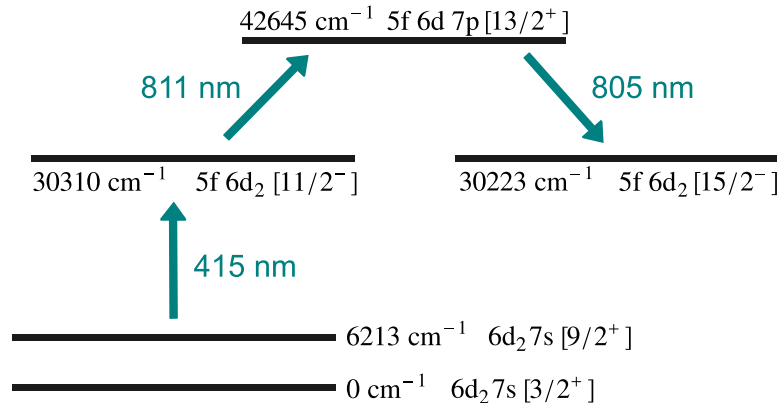

Figure 1.10: Possible laser excitation scheme of the $5f6d^2$ state starting from the $6d^27s$ state at 6213 cm^{-1}.

Proposed experimental implementation

We propose to perform an experimental verification of the IC from the aforementioned excited state of ^{229}Th$^+$ at the IGISOL facility, Jyväskylä, Finland [59]. Fig. 1.11 illustrates the layout of the facility of specific relevance to our proposal. The ^{229}Th ion beam with 2% in the nuclear isomeric state is produced at IGISOL via α-decay of ^{233}U. Following population of the metastable level at 6213 cm^{-1} in ^{229}Th$^+$ (see previous Section), the ion beam is injected into the radiofrequency (rf) quadrupole cooler-buncher [60]. Inside this device, the ions lose their residual energy through viscous collisions with low pressure ($\sim$1 mbar) helium gas, and a weak axial field is applied to the segmented electrodes in order to guide the ions to the exit region within 1 ms. Here the ions may be accumulated with a trapping potential and are bunched before extraction into a low-energy transfer line operating at 800 V before re-acceleration by the platform potential ($\sim$30 kV) towards the experimental setups. The time structure of a typical ion bunch is $\sim$10 μs. The ions are optically pumped to the 30223 cm^{-1} state within the rf cooler-buncher using laser light generated from high power pulsed tunable Ti:sapphire lasers [61]. Importantly, the state survives extraction from the cooler, acceleration and delivery to the collinear set-up, the general beamline layout of which is shown in Fig. 1.11. When the ions are released from the cooler in bunches, their time-of-flight to the detection region with an MCP detector depends on the mass-to-charge ratio m/q. Ions ^{229}Th^{2+} produced via IC from the excited 30223 cm^{-1} state will leave the cooler more quickly. The doubly-charged ion bunch will rapidly become spatially separated from the bunch of contaminant singly-charged ions thus allowing the latter to be electrostatically deflected from the beam path. The typical flight time from the ion beam cooler-buncher to the MCP detector shown in Fig. 1.11 for a mass A=100 singly-charged ion is 100 μs. This flight time scales with the square root of m/q and thus for singly-charged ^{229}Th$^+$ the expected flight time increases to approx. 1.5 ms. The corresponding flight time for doubly-charged ^{229}Th^{2+} is approx. 1.1 ms. This difference in the ion bunch arrival time is sufficient for a simple electrostatic deflection of one species and therefore a clear identification of the presence of the isomeric state can be made. It is expected
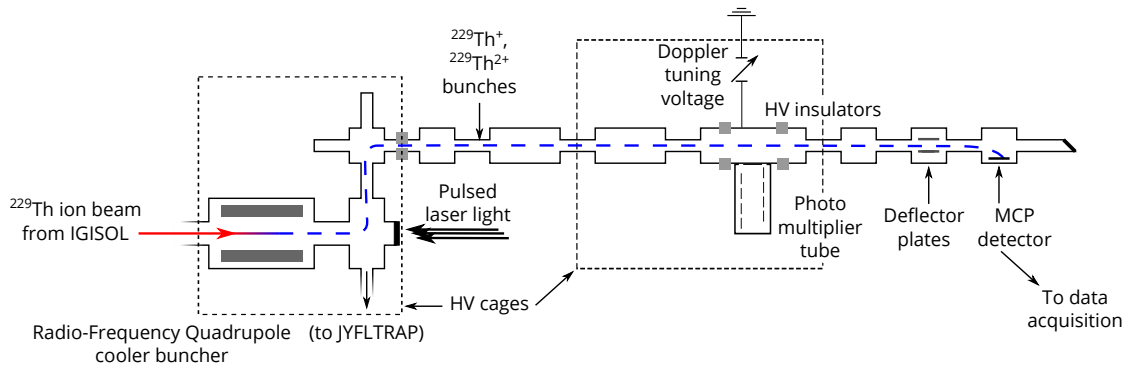
Figure 1.11: Schematic diagram of the radiofrequency (rf) quadrupole cooler-buncher device connected to the collinear laser spectroscopy beamline at the JYFL Accelerator Laboratory in Jyväskylä. Relevant details for the isomeric state detection of ^{229}Th$^+$ are discussed in the text.

that background doubly-charged ions may be formed inside the cooler-buncher via resonant excitation and ionization of singly-charged thorium. This process will be studied in detail using stable ^{232}Th$^+$ which does not possess any nuclear states at optical energies. We note that a recent experimental result sets a limitation on the isomeric state lifetime in Th$^+$ ions of < 10 ms [29]. This poses additional technical challenges in adopting fast procedures for isomer production, transport, extraction and excitation of the ions.

The described experimental scheme may allow to observe for the first time IC from excited electronic states of ^{229}Th ions and apply it for an estimate of the energy E_m and an experimental determination of the strength of the nuclear transition from the isomeric state ^{229m}Th to the ground state. The main challenge here appears to be the laser excitation of the electronic shell to states which live long enough to allow for IC to efficiently depopulate the isomeric state. In addition, we note that new laser spectroscopy data for ^{229}Th$^+$ and ^{229}Th^{2+} electronic excited states above 60000 cm^{-1} might enlarge the choice of states that can be used for the proposed scheme, if additional longer-lived excited electronic states are found. We note again that the isotope ^{229}Th due to the very low transition energy E_m is a unique case when energetically forbidden IC from the ground electronic state can be opened by means of an optical excitation of the electronic shell.

Chapter 2

Electronic bridge (EB)

The EB is a process in which the decay of the nuclear excited state happens via bound states of the atomic shell with the additional involvement of a photon [62–65]. It takes place when the nuclear excitation energy is less than the ionization potential and IC is forbidden by the energy conservation laws. If the nuclear transition is energetically close to an electronic transition between two bound states, the EB process may occur. A schematic illustration of EB is provided in Fig. 2.1. The nuclear excitation is transferred to the electronic shell promoting a bound outer electron to a virtual state which decays to a real bound state with the emission of a photon. The EB rate becomes especially large when the virtual electronic level happens to be close to a real bound electronic state. Depending on the actual value of E_m, the EB process may lead to a significant enhancement of the decay of the nuclear isomeric state in ^{229}Th ions, where the IC channel is energetically closed [30, 31]. Since the value E_m is known today with very limited accuracy $E_m = 7.8 \pm 0.5$ eV [14, 15], it is not possible to predict the contribution of the EB channel to the isomer decay. At the same time the EB process can be in principle utilized for improvement of the knowledge about the nuclear isomeric state in ^{229}Th.
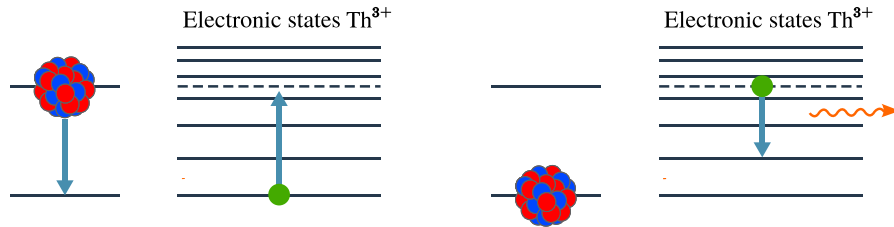

Figure 2.1: A schematic illustration of EB in a univalent ion Th^{3+}. The excited nucleus transfers its energy to a bound electron, which undergoes a transition to a virtual state (dashed line). The latter decays to a real bound state with the emission of a photon.

In this Chapter we propose an EB-based experimental scheme which allows a precise determination of the energy of the nuclear isomer ^{229}Th and a measurement of the strength of the isomeric nuclear transition [66]. In this approach the EB decay in the $^{229}\mathrm{Th}^{3+}$ ion is induced by radiation of a tunable optical or UV laser. In such laser-induced EB (LIEB), the virtual-state electron instead of spontaneous radiative de-excitation, is promoted by an external laser photon to a bound state at a higher energy. The energy of the photon E_phot has to be chosen such that it compensates the energy difference between the final electronic state and the virtual level. If E_i and E_f are the energies of the initial and final electronic states, respectively, the energy E_phot sufficient for the LIEB process is given by the expression

$$E_\mathrm{phot} = E_f - (E_m - E_i) \,. \tag{2.1}$$

Once this energy is found by scanning with the tunable laser, the LIEB process is observed and the energy of the nuclear isomeric state E_m can be obtained from the simple condition (2.1). The strength of the nuclear transition can be found by matching the measured LIEB rate to the theoretical predictions. The calculations in this Chapter show that depending on the actual value of E_m, a high LIEB rate of 10^4 s^{-1} can be achieved using a commercially available tunable laser.

The inverse process of EB can be used as a tool for excitation of the nuclear isomer in ^{229}Th [34, 55, 67, 68]. Whereas the direct excitation is complicated by the fact that the value E_m lies in the VUV range, the EB excitation mechanism involving the electronic shell would allow a usage of optical lasers. The EB excitation is schematically illustrated in Figure 2.2. The electronic shell is initially in an excited state, which can be reached by a laser excitation from the ground state or electronic collisions as discussed later in this Chapter. An external optical photon promotes the outer electrons to a virtual state, which decays to another real state with simultaneous excitation of the nucleus ^{229}Th to the isomeric state. It has been shown [34] that the EB excitation scheme in
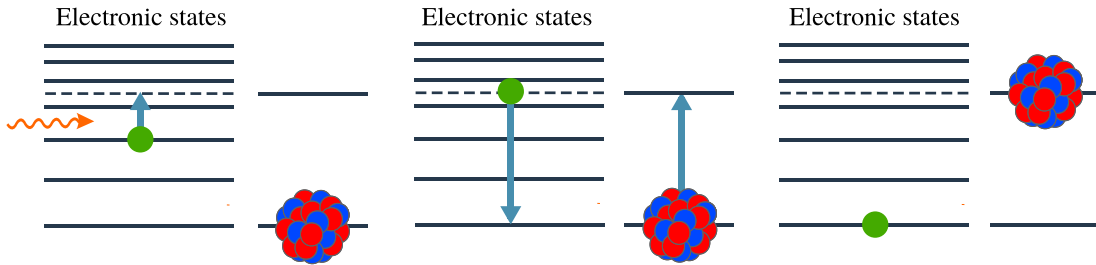

Figure 2.2: A schematic illustration of the EB excitation scheme. The atomic shell being initially in an excited state absorbs an external laser photon and is promoted to a virtual state (dashed line). The latter decays to a real state transferring its energy to the nucleus and exciting it to the isomeric state.

ions ^{229}Th$^+$ may be implemented using conventional laser sources. The excitation rate depends strongly on availability of proper electronic transitions close to the energy E_m. At the same time, the applied laser power is limited due to multi-photon ionization of ^{229}Th$^+$.

In this Chapter we investigate the possibility to use highly charged ions (HCI) of ^{229}Th with open d and f shells for the nuclear excitation. Due to their large ionization potential, HCI would allow the use of high-power lasers for EB. We present a particular EB scheme in the ^{229}Th^{35+} ion (electronic configuration $4f^9$) which would allow the excitation at a significant rate over the entire range $E_m = 7.8 \pm 0.5$ eV. In the case when the value E_m is higher, this scheme can be extended still providing a considerable excitation rate up to $E_m = 9.5$ eV. We show also another EB scheme in the ^{229}Th^{17+} ion (electronic configuration $5d^5$), which would allow to cover the energies E_m up to 10 eV. We anticipate that when the value E_m is known with a better accuracy, it would be possible to choose a particular EB scheme providing an efficient excitation of the nuclear isomeric state in ^{229}Th.

2.1 EB theory

In this Section we develop a formalism for description of the decay of the ^{229}Th isomeric state via EB, following the derivation outlined in Ref. [30]. The process of EB involves

the interaction of the nuclear multipole moments with the atomic shell and analogously to the case of IC in Section 1.1 can be described by the coupling operator $\hat{H}_{\text{int}}$ obtained in Appendix A. The states of the Th atom prior to EB and after EB can be represented as

$$
\begin{aligned}
|\alpha_m I_m N_m; \beta_i J_i M_i\rangle &= |\alpha_m I_m N_m\rangle |\beta_i J_i M_i\rangle \ , \\
|\alpha_g I_g N_g; \beta_f J_f M_f\rangle &= |\alpha_g I_g N_g\rangle |\beta_f J_f M_f\rangle \ ,
\end{aligned}
\tag{2.2}
$$

where we neglect again the hyperfine mixing and split the states into the products of nuclear and electronic parts. The difference in comparison to IC is that in this case both states involve only bound electrons.

The EB process can be represented by two Feynman diagrams shown in Fig. 2.3. We assume that the real emitted photon is an electric dipole photon, so that the process as a whole can be effectively considered as an electric dipole decay. The rate in this case
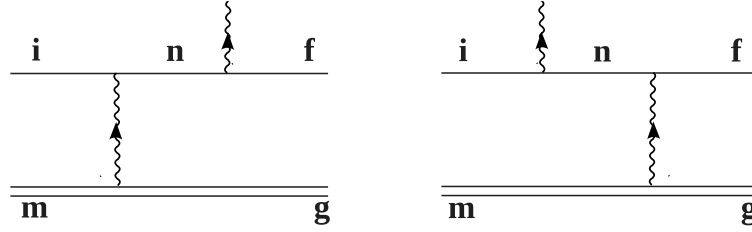

Figure 2.3: The Feynman diagrams of the EB process. The solid lines correspond to the electronic states, the double-lines represent the nuclear state and the wiggly lines depict the photons.

can be calculated as [41]

$$
\begin{aligned}
\Gamma_{\text{EB}} &= \frac{4\alpha^3 E_{\text{phot}}^3}{3(2I_m + 1)(2J_i + 1)} \\
&\times \sum_{N_m, M_i, N_g, M_f} \left| \langle \alpha_g I_g N_g; \beta_f J_f M_f | \hat{\mathbf{D}}^{\text{eff}} | \alpha_m I_m N_m; \beta_i J_i M_i \rangle \right|^2 \ ,
\end{aligned}
\tag{2.3}
$$

where we average over the initial states and sum over the final states with different magnetic quantum numbers. Here E_{phot} is the energy of the emitted photon, α is the fine structure constant and $\hat{\mathbf{D}}^{\text{eff}}$ is the effective electric dipole vector operator given by the expression

$$
\hat{\mathbf{D}}^{\text{eff}} = \sum_n \hat{\mathbf{D}} \frac{|\beta_n J_n M_n\rangle \langle \beta_n J_n M_n|}{E_{in} + E_m + \frac{i}{2}\Gamma_n} \hat{H}_{\text{int}} + \sum_n \hat{H}_{\text{int}} \frac{|\beta_n J_n M_n\rangle \langle \beta_n J_n M_n|}{E_{fn} - E_m + \frac{i}{2}\Gamma_n} \hat{\mathbf{D}}
\tag{2.4}
$$

corresponding to the diagrams in Fig. 2.3. Here $\hat{\mathbf{D}} = -\mathbf{r}$ is the ordinary electric dipole operator. The summation is extended over all intermediate electronic states $|\beta_n J_n M_n\rangle$ allowed by the selection rules. The quantities $E_{in} = E_i - E_n$ and $E_{fn} = E_f - E_n$ denote the energy differences of the corresponding electronic states. We have checked that the widths of the intermediate states Γ_n are small and can be neglected in the considered case as a coincidence of the isomer energy E_m with the energy difference of any two bound electronic states at the scale Γ_n is highly unlikely. Taking into account the form

of the operator $\hat{H}_{\text{int}}$ given by the expression (1.1), we obtain

$$\hat{\mathbf{D}}^{\text{eff}} = \sum_{\lambda L,q} (-1)^q \hat{\mathcal{M}}_{\lambda L,q} \left[\sum_n \hat{\mathbf{D}} \frac{|\beta_n J_n M_n\rangle \langle \beta_n J_n M_n|}{E_{in} + E_m} \hat{\mathcal{T}}_{\lambda L,-q} \right.$$
$$\left. + \sum_n \hat{\mathcal{T}}_{\lambda L,-q} \frac{|\beta_n J_n M_n\rangle \langle \beta_n J_n M_n|}{E_{fn} - E_m} \hat{\mathbf{D}} \right] . \qquad (2.5)$$

With (2.2), (2.3) and (2.5) the EB rate Γ_{EB} can be expressed via the nuclear matrix elements $\langle \alpha_g I_g N_g | \hat{\mathcal{M}}_{\lambda L,q} | \alpha_m I_m N_m \rangle$ and the electronic matrix elements of the form $\langle \beta_a J_a M_a | \hat{\mathcal{T}}_{\lambda L,q} | \beta_b J_b M_b \rangle$ and $\langle \beta_a J_a M_a | \hat{\mathbf{D}} | \beta_b J_b M_b \rangle$, where the generic indices a and b should be replaced by i, f or n for the initial, final and intermediate electronic states respectively. Instead of the x-, y- and z-projections of the electric dipole operator, we consider in the following its spherical components $\hat{D}_q$ defined as [39]

$$\hat{D}_{\pm 1} = \mp \frac{\hat{D}_x \pm i\hat{D}_y}{\sqrt{2}} , \quad \hat{D}_0 = \hat{D}_z . \qquad (2.6)$$

Using the Wigner-Eckart theorem [39], the considered matrix elements can be rewritten via the corresponding RME and Clebsch-Gordan coefficients as

$$\langle \alpha_g I_g N_g | \hat{\mathcal{M}}_{\lambda L,q} | \alpha_m I_m N_m \rangle = (-1)^{I_m - N_m} \frac{\langle \alpha_g I_g \| \hat{\mathcal{M}}_{\lambda L} \| \alpha_m I_m \rangle}{\sqrt{2L+1}} C^{I_g \ I_m \ L}_{N_g \ -N_m \ q} , \quad (2.7)$$

$$\langle \beta_a J_a M_a | \hat{\mathcal{T}}_{\lambda L,q} | \beta_b J_b M_b \rangle = (-1)^{L - J_b + J_a} \frac{\langle \beta_a J_a \| \hat{\mathcal{T}}_{\lambda L} \| \beta_b J_b \rangle}{\sqrt{2J_b+1}} C^{L \ J_b \ J_a}_{q \ m_b \ m_a} , \qquad (2.8)$$

$$\langle \beta_a J_a M_a | \hat{D}_q | \beta_b J_b M_b \rangle = (-1)^{J_b - M_b} \frac{\langle \beta_a J_a \| \hat{D} \| \beta_b J_b \rangle}{\sqrt{3}} C^{J_a \ J_b \ 1}_{M_a \ -M_b \ q} . \qquad (2.9)$$

After simplification of the nuclear part using (2.7) and the orthogonality relations for the Clebsch-Gordan coefficients, the EB rate takes the form

$$\Gamma_{\text{EB}} = \frac{4\alpha^3 E^3_{\text{phot}}}{3(2I_m+1)(2J_i+1)} \sum_{\lambda L} \frac{\left| \langle \alpha_g I_g \| \hat{\mathcal{M}}_{\lambda L} \| \alpha_m I_m \rangle \right|^2}{2L+1} G^{\lambda L} , \qquad (2.10)$$

where we have introduced the quantity $G^{\lambda L}$ defined as

$$G^{\lambda L} = \sum_{q,p,M_i,M_f} \left| \sum_n \frac{\langle \beta_f J_f M_f | \hat{D}_p | \beta_n J_n M_n \rangle \langle \beta_n J_n M_n | \hat{\mathcal{T}}_{\lambda L,-q} | \beta_i J_i M_i \rangle}{E_{in} + E_m} \right.$$
$$\left. + \sum_n \frac{\langle \beta_f J_f M_f | \hat{\mathcal{T}}_{\lambda L,-q} | \beta_n J_n M_n \rangle \langle \beta_n J_n M_n | \hat{D}_p | \beta_i J_i M_i \rangle}{E_{fn} - E_m} \right|^2 . \qquad (2.11)$$

After squaring, $G^{\lambda L}$ splits into a sum of three components $G^{\lambda L} = G^{\lambda L}_1 + G^{\lambda L}_{12} + G^{\lambda L}_2$ given by the expressions

$$G^{\lambda L}_1 = \sum_{q,p,M_i,M_f} \left| \sum_n \frac{\langle \beta_f J_f M_f | \hat{D}_p | \beta_n J_n M_n \rangle \langle \beta_n J_n M_n | \hat{\mathcal{T}}_{\lambda L,-q} | \beta_i J_i M_i \rangle}{E_{in} + E_m} \right|^2 , \quad (2.12)$$

$$G_2^{\lambda L} = \sum_{q,p,M_i,M_f} \left| \sum_n \frac{\langle \beta_f J_f M_f | \hat{\mathcal{T}}_{\lambda L,-q} | \beta_n J_n M_n \rangle \langle \beta_n J_n M_n | \hat{D}_p | \beta_i J_i M_i \rangle}{E_{fn} - E_m} \right|^2, \quad (2.13)$$

$$G_{12}^{\lambda L} = 2\,\mathrm{Re}\left[\sum_{q,p,M_i,M_f} \sum_n \frac{\langle \beta_f J_f M_f | \hat{D}_p | \beta_n J_n M_n \rangle \langle \beta_n J_n M_n | \hat{\mathcal{T}}_{\lambda L,-q} | \beta_i J_i M_i \rangle}{E_{in} + E_m} \right.$$
$$\left. \times \sum_k \frac{\langle \beta_f J_f M_f | \hat{\mathcal{T}}_{\lambda L,-q} | \beta_k J_k M_k \rangle^* \langle \beta_k J_k M_k | \hat{D}_p | \beta_i J_i M_i \rangle^*}{E_{fk} - E_m} \right], \quad (2.14)$$

where z^* is the complex conjugate of a complex number z and $\mathrm{Re}(z)$ denotes its real part. The component $G_1^{\lambda L}$ is completely related to the left diagram in Fig. 2.3, the part $G_2^{\lambda L}$ can be attributed to the right diagram in Fig. 2.3, whereas the combined term $G_{12}^{\lambda L}$ corresponds to interference between the two diagrams. After decomposition of the matrix elements using (2.8)—(2.9) and application of the orthogonality conditions for the Clebsch-Gordan coefficients, we obtain

$$G_1^{\lambda L} = \sum_{J_n} \frac{1}{2J_n + 1} \left| \sum_{\beta_k} \frac{\langle \beta_f J_f \| \hat{D} \| \beta_k J_n \rangle \langle \beta_k J_n \| \hat{\mathcal{T}}_{\lambda L} \| \beta_i J_i \rangle}{E_{ik} + E_m} \right|^2, \quad (2.15)$$

$$G_2^{\lambda L} = \sum_{J_n} \frac{1}{2J_n + 1} \left| \sum_{\beta_k} \frac{\langle \beta_f J_f \| \hat{\mathcal{T}}_{\lambda L} \| \beta_k J_n \rangle \langle \beta_k J_n \| \hat{D} \| \beta_i J_i \rangle}{E_{fk} - E_m} \right|^2, \quad (2.16)$$

$$G_{12}^{\lambda L} = 2 \sum_{J_t J_n} (-1)^{J_t + J_n} \left\{ \begin{array}{ccc} J_i & J_t & 1 \\ J_f & J_n & L \end{array} \right\} \sum_{\beta_k} \frac{\langle \beta_f J_f \| \hat{D} \| \beta_k J_n \rangle \langle \beta_k J_n \| \hat{\mathcal{T}}_{\lambda L} \| \beta_i J_i \rangle}{E_{ik} + E_m}$$
$$\times \sum_{\beta_s} \frac{\langle \beta_f J_f \| \hat{\mathcal{T}}_{\lambda L} \| \beta_s J_t \rangle \langle \beta_s J_t \| \hat{D} \| \beta_i J_i \rangle}{E_{fs} - E_m}. \quad (2.17)$$

In the expression for $G_{12}^{\lambda L}$ we have used the relation

$$\sum_{m_1,m_2,m_3,m_{12},m_{23}} C_{m_1 m_2 m_{12}}^{j_1\ j_2\ j_{12}}\, C_{m_{12} m_3 m}^{j_{12}\ j_3\ j}\, C_{m_2 m_3 m_{23}}^{j_2\ j_3\ j_{23}}\, C_{m_1 m_{23} m'}^{j_1\ j_{23}\ j'}$$
$$= \delta_{jj'} \delta_{mm'} (-1)^{j_1+j_2+j_3+j} \sqrt{(2j_{12}+1)(2j_{23}+1)} \left\{ \begin{array}{ccc} j_1 & j_2 & j_{12} \\ j_3 & j & j_{23} \end{array} \right\}, \quad (2.18)$$

which can be considered as the definition of the $6j$-coefficient [69]. Using instead of the nuclear RME the reduced transition probability $B_\downarrow^{\lambda L}$ defined by (1.5), the EB rate can be now written as

$$\Gamma_{\mathrm{EB}} = \frac{16\pi \alpha^3 E_{\mathrm{phot}}^3}{3(2J_i + 1)} \sum_{\lambda L} \frac{B_\downarrow^{\lambda L} G^{\lambda L}}{(2L+1)^2}. \quad (2.19)$$

The ratio $\beta_{\mathrm{EB}}^{\lambda L}$ of the EB rate and radiative decay rate for a fixed λ and L is often used in order to obtain a result independent of the value $B_\downarrow^{\lambda L}$. The radiative decay rate can be written as [30]

$$\Gamma_{\mathrm{rad}}^{\lambda L} = 8\pi \frac{\alpha^{2L+1} E_m^{2L+1}}{[(2L+1)!!]^2} \frac{L+1}{L} B_\downarrow^{\lambda L}. \quad (2.20)$$

Then we obtain the expression for $\beta_{\text{EB}}^{\lambda L} = \Gamma_{\text{EB}}^{\lambda L} / \Gamma_{\text{rad}}^{\lambda L}$

$$\beta_{\text{EB}}^{\lambda L} = \frac{2L[(2L+1)!!]^2}{3(L+1)(2L+1)^2} \cdot \frac{E_{\text{phot}}^3}{\alpha^{2L-2} E_m^{2L+1}} \cdot \frac{G^{\lambda L}}{2J_i + 1} \ . \tag{2.21}$$

This quantity was used e.g. in Refs. [30, 31] for description of the EB decay in ^{229}Th ions.

The electronic RME in one-electron case

The electronic RME of the form $\langle \beta_a J_a \| \hat{D} \| \beta_b J_b \rangle$ and $\langle \beta_a J_a \| \hat{\mathcal{T}}_{\lambda L} \| \beta_b J_b \rangle$ depend on the electronic configurations of the involved states. In the case of one electron above closed shells we reduce these RME to the radial integrals, which are evaluated based on the wave functions obtained numerically using the DHF approach. Some RME are then improved using the method of random phase approximation (RPA). We consider in this Chapter also more complicated electronic configurations, for which in the context of the considered problems the whole RME can be obtained directly with the GRASP2K package [47]. The used numerical methods are discussed later in this Chapter and in more detail in Chapter 4.

In the one-electron case the states are described by the principal quantum number n of the electron and its relativistic quantum number κ defined by (1.8). The RME of the operator $\hat{\mathcal{T}}_{\lambda L}$ of the form $\langle n_a \kappa_a \| \hat{\mathcal{T}}_{\lambda L} \| n_b \kappa_b \rangle$ for can be written using the Appendix. C as

$$\langle n_a \kappa_a \| \hat{\mathcal{T}}_{EL} \| n_b \kappa_b \rangle = (-1)^{L + \frac{1}{2} - j_b} \Pi_{l_a + l_b + L} \sqrt{(2j_a + 1)(2j_b + 1)} \tag{2.22}$$

$$\times \begin{pmatrix} j_a & j_b & L \\ \frac{1}{2} & -\frac{1}{2} & 0 \end{pmatrix} R_{ab}^{EL} \ ,$$

$$\langle n_a \kappa_a \| \hat{\mathcal{T}}_{ML} \| n_b \kappa_b \rangle = (-1)^{L + \frac{1}{2} + j_b} \Pi_{l_a + l_b + L + 1} \frac{\sqrt{(2j_a + 1)(2j_b + 1)}}{L} \tag{2.23}$$

$$\times (\kappa_a + \kappa_b) \begin{pmatrix} j_a & j_b & L \\ \frac{1}{2} & -\frac{1}{2} & 0 \end{pmatrix} R_{ab}^{ML} \ ,$$

where we distinguish between the electric and magnetic types of the operator $\hat{\mathcal{T}}_{\lambda L}$. The function Π defined by (1.16) assures the proper parity of the electronic states. The radial integrals R_{ab}^{EL} and R_{ab}^{ML} are given by the expressions

$$R_{ab}^{EL} = \int_0^\infty \frac{dr}{r^{L+1}} \Big(P_{n_a \kappa_a}(r) P_{n_b \kappa_b}(r) + Q_{n_a \kappa_a}(r) Q_{n_b \kappa_b}(r) \Big) , \tag{2.24}$$

$$R_{ab}^{ML} = \int_0^\infty \frac{dr}{r^{L+1}} \Big(P_{n_a \kappa_a}(r) Q_{n_b \kappa_b}(r) + P_{n_b \kappa_b}(r) Q_{n_a \kappa_a}(r) \Big) , \tag{2.25}$$

containing the bound radial wave functions P and Q defined by (1.19). The RME of the operator $\hat{D}$ can be found using its spherical representation

$$\hat{D}_q = -r_q = -C_{1q} r \ , \tag{2.26}$$

where the function C_{lm} can be expressed via the spherical function Y_{lm} with the orbital

momentum l and its projection m as

$$C_{lm} = \sqrt{\frac{4\pi}{2l+1}} Y_{lm} \,. \tag{2.27}$$

Taking into account the RME for C_{lm} [41]

$$\langle \kappa_a \| C_l \| \kappa_b \rangle = (-1)^{j_a + \frac{1}{2}} \Pi_{l_a + l_b + l} \sqrt{(2j_a + 1)(2j_b + 1)} \begin{pmatrix} j_a & j_b & l \\ -\frac{1}{2} & \frac{1}{2} & 0 \end{pmatrix} \tag{2.28}$$

we obtain the RME for the operator $\hat{D}$

$$\langle n_a \kappa_a \| \hat{D} \| n_b \kappa_b \rangle = (-1)^{j_b - \frac{1}{2}} \Pi_{l_a + l_b + 1} \sqrt{(2j_a + 1)(2j_b + 1)} \begin{pmatrix} j_a & j_b & 1 \\ \frac{1}{2} & -\frac{1}{2} & 0 \end{pmatrix} R_{ab}^{E1} \,, \tag{2.29}$$

with the radial integral

$$\widetilde{R}_{ab}^{E1} = \int_0^\infty dr\, r \left(P_{n_a \kappa_a}(r) P_{n_b \kappa_b}(r) + Q_{n_a \kappa_a}(r) Q_{n_b \kappa_b}(r) \right) \,. \tag{2.30}$$

We use here the notation $\widetilde{R}$ instead of R since the form of the integrand differs from that in the equations (2.24)—(2.25).

2.2 Dipole and quadrupole EB channels in ^{229}Th

In this Section we present our results for the EB enhancement factors β_{EB} in a univalent ion ^{229}Th^{3+} for $M1$ and $E2$ isomer decay channels, published also in [45]. We show that the $E2$ EB channel, which has been usually neglected based on the older predictions for the nuclear transition probabilities $B_\downarrow^{M1}$ and $B_\downarrow^{E2}$ [30], turns out in most cases to play an important role for the newest predicted values $B_\downarrow^{M1} = 0.0076$ W.u. and $B_\downarrow^{E2} = 29$ W.u. [44]. We carry out calculations for different initial and final electronic states and show that in the case when the nuclear transition is coupled to an electronic transition involving the $7s$-orbital, the $E2$ contribution can be safely neglected, whereas if only the orbitals $7p$, $6d$ and $5f$ participate, the contribution of the $E2$ channel is dominant or at least of the same order of magnitude as the $M1$ one.

For calculation of β_{EB} we use the expression (2.21) and the electronic RME calculated with (2.22)—(2.25) and (2.29)—(2.30). The involved bound radial wave functions cannot be evaluated using the GRASP2K package due to the following reason. The expressions for the quantities $G^{\lambda L}$ in Eqs. (2.11)—(2.14) contain summations over all intermediate electronic states allowed by the corresponding selection rules, including summation over highly excited bound states and integration over continuum states. The GRASP2K package is however limited in evaluation of excited states already with principal quantum numbers approaching $n = 10$ and cannot provide all needed wave functions. On the other hand, integration over continuum wave functions obtained from the RATIP package applied for the IC calculations in Chapter 1 is not straightforward. We use instead the following scheme for evaluation of the required matrix elements. As a first step we calculate a few low-lying states of the valence electron using the DHF method in the frozen-core approximation. Secondly, we consider the ion to be placed into a cavity of radius $R = 90$ a.u. and build virtual orbitals with the principal quantum number up to $n = 30$ via expansion in a B-spline basis set [41]. The result of the DHF calculation

serves as an input for this second step. This procedure allows us to work with a discrete spectrum at positive energies and due to the large size of the cavity does not affect the accuracy of the calculated matrix elements considerably. While the values for the $E2$ matrix elements obtained at this stage are satisfactory, the values for the $M1$ matrix elements require further improvement [70, 71]. To achieve adequate accuracy, we take into account correlation effects between the valence electron and the frozen core using the RPA method [41]. In contrast to the case of electric matrix elements, the obtained RPA corrections for magnetic matrix elements are often significantly larger than the corresponding DHF values. We double-checked our computation method for the $M1$ matrix elements by calculating the hyperfine structure constant A for various orbitals of the Na valence electron and comparing them with existing values in literature for combined DHF and RPA calculations [41]. The results show a good agreement. In Chapter 4 we discuss the used numerical approach in more detail.

In order to directly compare our results with available theoretical values in Ref. [30], we have considered here the same nuclear transition energy $E_m = 7.6$ eV as assumed there. The agreement is satisfactory except for the value of $\beta_{\rm EB}^{M1}$ for EB from the initial state $5f_{5/2}$ to the final state $7s_{1/2}$, where the values differ by a factor 2.5. We consider this issue not critical for our purposes especially taking into account the significant disagreement in RPA calculations for $M1$ matrix elements present in literature [70, 71]. The small deviations of the $E2$ rates can be attributed to the RPA corrections included in Ref. [30] but missing in the present calculations.

Init.	Fin.	Present work			From [30]	
		$\beta_{\rm EB}^{M1}$	$\beta_{\rm EB}^{E2}$	ρ	$\beta_{\rm EB}^{M1}$	$\beta_{\rm EB}^{E2}$
$5f_{5/2}$	$7s_{1/2}$	0.082	$3.4 \cdot 10^7$	0.29	0.032	$5 \cdot 10^7$
$7s_{1/2}$	$7p_{1/2}$	23	$6.6 \cdot 10^8$	0.020	19	$7 \cdot 10^8$
$7s_{1/2}$	$7p_{3/2}$	5.2	$9.3 \cdot 10^7$	0.012	4.4	$1 \cdot 10^8$
$6d_{3/2}$	$7p_{1/2}$	0.0022	$1.2 \cdot 10^7$	3.8	-	-
$6d_{5/2}$	$7p_{1/2}$	0.013	$3.6 \cdot 10^7$	1.9	-	-
$6d_{5/2}$	$7p_{3/2}$	$2.4 \cdot 10^{-5}$	$2.4 \cdot 10^5$	6.9	-	-

Table 2.1: Enhancement factors $\beta_{\rm EB}^{M1}$ and $\beta_{\rm EB}^{E2}$ and the ratio $\rho = \Gamma_{\rm EB}^{E2}/\Gamma_{\rm EB}^{M1}$ for $M1$ and $E2$ EB channels between different initial and final electronic states in a univalent Th^{3+} ion. For comparison we also present the $\beta_{\rm EB}^{M1}$ and $\beta_{\rm EB}^{E2}$ results based on DHF+RPA calculations from Ref. [30] where available. The nuclear isomeric state energy is assumed to be $E_m = 7.6$ eV to match the value used in Ref. [30].

Our results in Table 2.1 show that $\Gamma_{\rm EB}^{E2}$ is smaller than $\Gamma_{\rm EB}^{M1}$ for the transitions involving the $7s_{1/2}$ orbital. In particular, $\Gamma_{\rm EB}^{E2}$ is two orders of magnitude smaller than $\Gamma_{\rm EB}^{M1}$ for the EB scheme between the electronic states $7s_{1/2}$ and $7p_{1/2,3/2}$, where $\beta_{\rm EB}^{M1}$ is largest. This can be explained by the presence of a strong $M1$ transition between the initial state $7s_{1/2}$ and the intermediate state $8s_{1/2}$. At the same time the $E2$ transition between these states is forbidden by selection rules. For all other cases the $E2$ contribution is comparable (for instance a third of the $M1$ contribution for EB between the electronic states $5f_{5/2}$ and $7s_{1/2}$) or even dominating with respect to the $M1$ channel.

2.3 Laser-induced EB (LIEB)

In this Section we propose a EB-based approach aiming for a measurement of the energy of the ^{229}Th nuclear isomeric state at a precision typical to laser atomic spectroscopy

and which would also improve knowledge of its radiative lifetime. The results discussed here are published in Ref. [66]. The method is based on nuclear de-excitation by the laser-induced process of LIEB. Especially for a nuclear transition energy E_m around 12 eV, this process has an especially high rate and could be very efficient to characterize the nuclear transition with the help of a tunable optical laser. LIEB is a version of the EB process in which the additional photon is not emitted, but absorbed by the electronic shell from an externally applied laser field. The process is thus equivalent to the excitation of the electronic shell with two photons, one of which is provided by the laser source and the other one from the nuclear de-excitation. This process was first considered for atomic ^{229}Th in 1992 by F. Karpeshin *et al.* [72]. It was shown that an enhancement factor of the decay of the isomeric state ^{229m}Th of the order 10^3 can be achieved. We note that at the time, the isomeric energy was believed to lie around 3.5 eV, such that IC of the neutral thorium atom wouldn't have been possible. Meanwhile it is known today that the isomeric nuclear state in a neutral atom decays very fast via IC [28], rendering the scheme proposed in Ref. [72] obsolete. We consider LIEB in the ^{229}Th^{3+} ion and show that with up-to-date laser technology the enhancement can reach the order 10^8 if the value E_m is close to the ionization threshold of Th$^+$. This would allow for a measurement of the transition energy and decay rate by using a tunable optical laser. ^{229}Th^{3+} ions allow high controllability as far as trapping and cooling are concerned and possess a simple electronic spectrum, rendering a reliable experimental implementation possible.

The LIEB process can be represented by two Feynman diagrams shown on the left-hand side of Fig. 2.4. As in the case of the usual EB process, the intermediate electronic state $|n\rangle$ runs over all the levels allowed by the selection rules (in the entire spectrum, including the continuum). We make use of the fact (also considered in Ref. [72]) that the coupling of the nuclear transition is maximal to an $M1$ electronic transition between s-orbitals and considerable for transitions between $p_{1/2}$-orbitals. At the same time the $E2$ transition between these orbitals is forbidden by the selection rules. We consider therefore the excited $7s$-state as the initial electronic state $|i\rangle$ and the $8p_j$- and $9p_j$-states with the total angular momentum $j \in \{1/2, 3/2\}$ in the role of the state $|f\rangle$. With this choice the channels $7s \rightarrow ns \rightarrow |f\rangle$ with $n = 8, 9$ and $7s \rightarrow 7p_{1/2} \rightarrow |f\rangle$ would then play the dominating role. These two channels are described by the two different Feynman diagrams in Fig. 2.4, corresponding to different absorption sequences of the two photons by the electron. A further advantage of using the $7s$-state as the initial state is its metastability, i.e. very long lifetime of 0.6 s [73]. Note that since $|n\rangle$ is actually a virtual state, the energy of the $M1$ photon does not necessarily have to coincide with the energy of the $M1$ electronic transition, though the overall transition energy $|i\rangle \rightarrow |f\rangle$ has to be equal to the sum of the energies of the two photons (see Fig. 2.4).

The nuclear isomer energy E_m can be found via scanning with a tunable laser for a LIEB resonance, i.e., for the population and decay of the upper state $|f\rangle$. The decay observation of the $|f\rangle$ state would correspond to the sum of the nuclear excitation energy and the energy of the laser photon equaling the overall electronic transition energy. If the resonant laser photon energy is E_{phot}, then E_m can be calculated as $E_m = E_f - E_i - E_{\text{phot}}$, where E_i and E_f are the energies of the electronic state $|i\rangle$ and $|f\rangle$, respectively. The height of the measured LIEB resonances would provide information about the magnitude of the nuclear γ-decay rate.
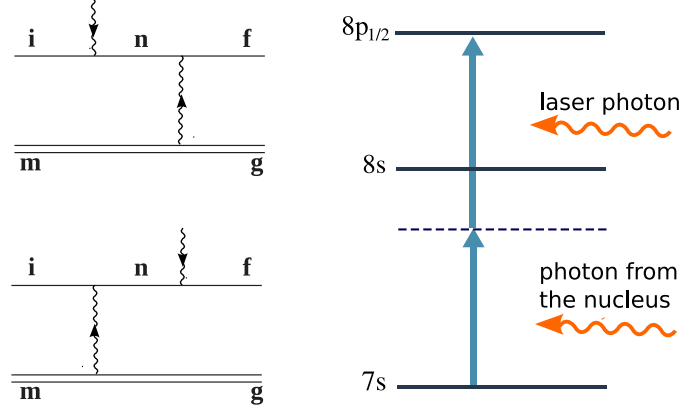
Figure 2.4: Example of LIEB process (right) and its Feynman diagrams (left). The solid lines in the Feynman diagrams correspond to the electronic states, the double-lines represent the nuclear state and the wiggly lines depict the photons. See text for further explanations.

The LIEB rate

We calculate the LIEB rate Γ_{LIEB} by relating to the rate of the inverse spontaneous process Γ_{spont} via the expression [74]

$$\Gamma_{\text{LIEB}} = \Gamma_{\text{spont}} \frac{4\pi^3 c^2 \hbar^2}{E_{\text{phot}}^3} P_\omega \delta \ , \tag{2.31}$$

where P_ω is the the spectral intensity of the laser field, c is the speed of light, $\hbar$ is Planck constant and

$$\delta = \frac{(2I_g + 1)(2J_f + 1)}{(2I_m + 1)(2J_i + 1)} \tag{2.32}$$

denotes the ratio of magnetic quantum number degeneracies of the initial states in the case of the direct and the inverse processes. For calculation of Γ_{spont} we adopt the formalism for the traditional EB scenario, taking into account the different direction of the nuclear process, i.e. excitation instead of de-excitation. The Feynman diagrams of this process can be obtained from the diagrams in Fig. 2.4 by mirror reflection and inversion of the photon lines. The resulting diagrams are the same as the diagrams for the usual EB process shown in Fig. 2.3 up to the direction of the line representing the nucleus. The rate can be thus obtained as

$$\Gamma_{\text{spont}} = \Gamma_{\text{EB}}^{M1} \frac{2I_m + 1}{2I_g + 1} \ , \tag{2.33}$$

where Γ_{EB}^{M1} is given by the expression (2.19) for $\lambda L = M1$.

Numerical results

The graphs in Fig. 2.5 show the LIEB rate Γ_{LIEB} as a function of the nuclear isomer energy for different final electronic states. We depict also the energy of the resonant laser photon E_{phot}, considering values in the range from 1.2 to 2.2 eV available with modern high power tunable lasers. If the energy E_m is close to the electronic $M1$ transition, then a large enhancement $\Gamma_{\text{LIEB}}/\Gamma_{\text{rad}}$ up to 10^8 can be achieved. The large peak appearing in all the four cases corresponds to the resonance in the lower diagram in Fig. 2.4 for the $M1$ electronic transition between the initial state $|i\rangle = |7s\rangle$ and the intermediate state
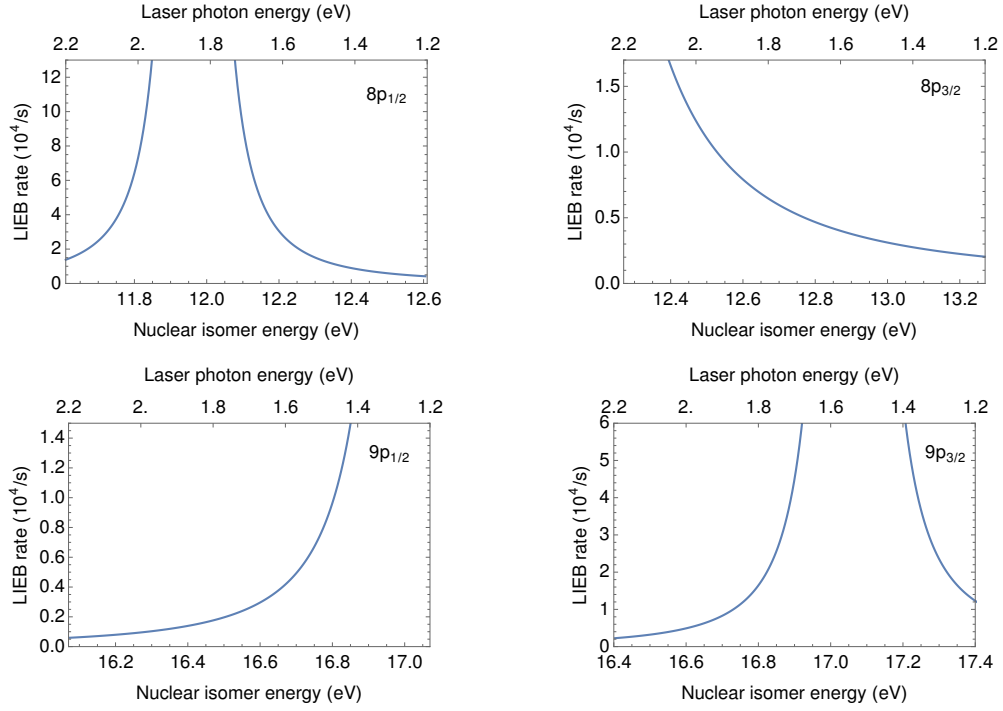
Figure 2.5: The LIEB rate Γ_{LIEB} as a function of the nuclear isomeric state energy (lower axis) and the corresponding laser photon energy (upper axis). The final electronic states are $8p_{1/2}$, $8p_{3/2}$, $9p_{1/2}$ and $9p_{3/2}$, respectively. The considered laser spectral intensity is $P_\omega = 1 \, \frac{\mathrm{W}}{\mathrm{m^2 \cdot Hz}}$.
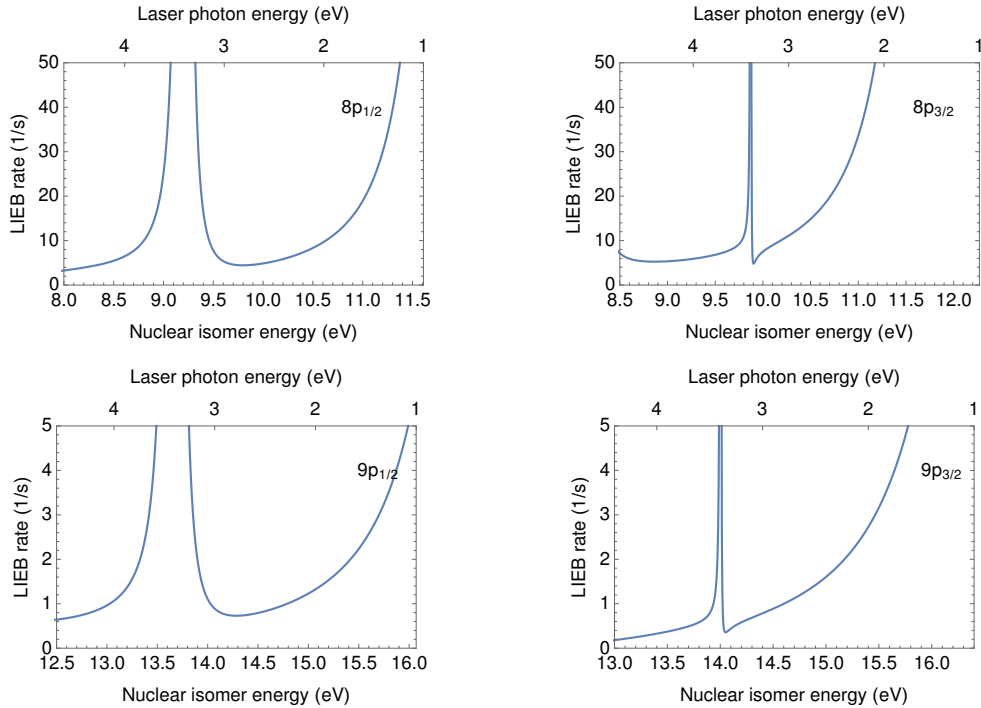

Figure 2.6: The LIEB rate Γ_{LIEB} as a function of the nuclear isomeric state energy (lower axis) and the corresponding laser photon energy (upper axis). The final electronic states are $8p_{1/2}$, $8p_{3/2}$, $9p_{1/2}$ and $9p_{3/2}$, respectively. The considered laser spectral intensity is $P_\omega = 10^{-2} \, \frac{\mathrm{W}}{\mathrm{m^2 \cdot Hz}}$.

$|n\rangle = |8s\rangle$ or $|n\rangle = |9s\rangle$. We note however that this substantial enhancement would only be present if the isomer energy lies around 12 or 17 eV.

In case E_m is closer to the presently accepted value of 7.8 ± 0.5 eV [14, 15], a laser with higher photon energy is required. In Fig. 2.6 we show the LIEB rate Γ_{LIEB} calculated using the value $P_\omega = 10^{-2} \frac{\text{W}}{\text{m}^2 \cdot \text{Hz}}$ for laser photon energies higher than 2.2 eV, as obtainable with an average laser power of 0.01 W in a 1 MHz linewidth and a 1 mm^2 focus area. This might be a too conservative estimate for 2.5 eV, but simultaneously already demanding for 4.5 eV photon energies, respectively. We observe new peaks, which correspond to the case of resonances in the upper Feynman diagram in Fig. 2.4, when E_m coincides with the energy between the final state and an intermediate state among $7p_j$ and $8p_j$ with $j \in \{1/2, 3/2\}$. In this case the strongest peaks occur for electronic $M1$ transitions between $p_{1/2}$-states. Provided the spectral intensity $P_\omega = 10^{-2} \frac{\text{W}}{\text{m}^2 \cdot \text{Hz}}$ in the depicted region of laser photon energy can be reached, the described method would be applicable for lower values of E_m as low as 8 eV under conditions of good detection efficiency.

Discussion

Using the described scheme, the energy of the nuclear isomeric state ^{229m}Th can be determined with a tunable optical laser. The rate of the LIEB process can be measured by means of detection of the spontaneous decay photons of the final electronic state $|f\rangle$. Comparing the value of the resonant LIEB rate to the theoretical predictions, it is possible to find Γ_{rad}. Note that among various charge states of thorium, the univalent ^{229}Th^{3+} ion allows particularly accurate *ab initio* calculations for the electronic shell. The ^{229}Th^{2+} ions which would also fulfill this requirement cannot be used for the described method, as no metastable states with either s- or $p_{1/2}$-electrons involved are available. The described scheme in ^{229}Th^{3+} is therefore a unique reliable way for determination of the Th nuclear isomeric state parameters via laser-induced nuclear de-excitation involving the electronic shell.

The LIEB scheme requires production and trapping of ^{229m}Th in the 3+ ionization state and the excitation of the electronic shell to the $7s$-initial state. Regarding the production of the isomeric state, the direct nuclear photoexcitation of the ground-state thorium has failed so far due to the poor knowledge of the transition energy. Instead, one typically takes advantage of the 2% branching ratio to the low-energy isomeric state [53, 54] in the process of α-decay of ^{233}U and subsequent gamma-ray de-excitation. Inevitably a mixture of mostly ground state and just few isomeric state ^{229}Th^{3+} ions would then be loaded in the ion trap. We anticipate that $10^4 - 10^5$ ions could be produced and trapped at the Munich setup [28, 29] where a cryogenic Paul trap is being built [75]. This setup will keep ^{229}Th^{3+} ions in the absence of charge exchange and chemical reactions for a storage time longer than the time of isomer radiative decay. The electronic shell can be effectively transferred from the ground state $5f_{5/2}$ to the $7s$-state making use of the Stimulated Raman Adiabatic Passage (STIRAP) method [76] via the intermediate state $6d_{3/2}$. Note that the second transition in the STIRAP scheme is an electric quadrupole ($E2$) transition and thus requires higher driving laser intensity. Once reached, the $7s$-state has a long lifetime (0.6 s) allowing for applying the LIEB scheme.

Upon interaction with the tunable optical or ultra-violet laser, the isomeric state which otherwise has a long radiative lifetime of approx. 10^4 s may decay via the LIEB process. Population and radiative decay of the upper electronic states np_j with $n =$

8, 9 and $j \in \{1/2, 3/2\}$ could be observed by detection of fluorescence photons. We present the calculated radiative decay rates for the electric dipole channels together with experimental photon energy values from Ref. [46] in Table 2.2. Since the energy of the emitted photon in the dominant decay channels is mostly in the range 15–20 eV, i.e. significantly higher than that of the laser photons that are used for the excitation, the selection of a suitable photocathode material (like CsI) for photoelectron production inside the vacuum system will ensure a detection that is free from background of laser stray light. The background due to the absorption of the laser radiation by the electron in thorium ions with the nucleus in the ground state is expected to be small since the envisaged electronic transitions are energetically much higher than the laser photon energy. A direct comparison with the case of ^{232}Th which does not possess any nuclear states at optical energies should help to identify the signal stemming from the isomeric state decay.

Init. state	Final state	Phot. energy (eV)	Rate (10^8 s^{-1})
$8p_{1/2}$	$7s_{1/2}$	13.8	0.26
	$8s_{1/2}$	1.85	4.96
	$6d_{3/2}$	15.5	19.4
	$7d_{3/2}$	1.84	5.81
$8p_{3/2}$	$7s_{1/2}$	14.5	5.05
	$8s_{1/2}$	2.51	11.3
	$6d_{3/2}$	16.2	3.12
	$6d_{5/2}$	15.6	24.9
	$7d_{3/2}$	2.50	1.15
	$7d_{5/2}$	2.29	8.76
$9p_{1/2}$	$7s_{1/2}$	18.3	0.57
	$8s_{1/2}$	6.31	0.045
	$9s_{1/2}$	1.21	3.30
	$6d_{3/2}$	20.0	11.5
	$7d_{3/2}$	6.30	1.36
	$8d_{3/2}$	1.06	3.13
$9p_{3/2}$	$7s_{1/2}$	18.6	1.76
	$8s_{1/2}$	6.64	1.30
	$9s_{1/2}$	1.54	6.01
	$6d_{3/2}$	20.3	1.80
	$6d_{5/2}$	19.68	14.5
	$7d_{3/2}$	6.63	0.42
	$7d_{5/2}$	6.42	3.02
	$8d_{3/2}$	1.39	0.56
	$8d_{5/2}$	1.32	4.73

Table 2.2: Radiative decay channels of the states $8p_{1/2}$, $8p_{3/2}$, $9p_{1/2}$, $9p_{3/2}$.

2.4 EB excitation in HCI

The process inverse to the EB decay can be used for excitation of the ^{229}Th nucleus to its isomeric state in Th ions with an optical laser. It was shown in Ref. [34] that the EB enhancement factor $\beta \approx 30$ for the ion Th$^+$ can be achieved in an excitation scheme

which can be implemented using commercially available lasers. For the radiative decay rate of the ^{229}Th nuclear isomer of 10^4 s^{-1}, the value $\beta \approx 30$ corresponds to an excitation rate $3 \cdot 10^{-3}$ s^{-1} per ion, which results in a considerable rate for a cloud of ions. The scheme depends strongly on availability of proper electronic transitions with energies close to the nuclear isomer energy E_m. This can be a limitation if the actual value E_m happens to lie in between of the energies for the effective EB excitation. On the other hand, the applicable laser power is limited due to possible many-photon ionization to the next charge state.

We consider in this Section a possibility to use highly charged ^{229}Th ions with open d and f electronic shells. The advantages of this approach are the following. Since all states in the low-energy part of the electronic spectrum of each ion belong to the same configuration, there are numerous $M1$ and $E2$ transitions, which couple to the nuclear transition between the isomeric and the ground states. Moreover, the very high ionization threshold of HCI allows application of higher laser intensities. Tables 2.3—2.4 show low-energy parts of the electronic spectra of the ions Th^{17+} and Th^{35+} with the configurations $5d^5$ and $4f^9$, respectively. The levels were obtained using the package GRASP2K [47], which in contrast to the case of Th ions with a low charge, provides now energy values with a good accuracy.

E (eV)	J	E (eV)	J
0.00	5/2	18.76	9/2
5.61	5/2	19.32	5/2
8.42	7/2	19.39	7/2
8.53	3/2	20.08	3/2
9.10	11/2	20.80	1/2
9.83	9/2	20.90	7/2
10.19	5/2	22.68	9/2
10.49	1/2	23.32	5/2
11.52	7/2	25.29	7/2
13.87	5/2	25.69	3/2
13.89	3/2	25.97	5/2
15.50	7/2	26.07	11/2
16.05	11/2	26.08	3/2
16.35	9/2	27.61	9/2
16.59	1/2	28.46	5/2
16.91	3/2	29.07	7/2
17.45	13/2	31.00	1/2
17.51	5/2	33.87	3/2

Table 2.3: The low-energy part of the electronic spectrum of the Th^{17+} ion containing the configuration $5d^5$. Here E is the energy of the level and J is its total angular momentum.

Figure 2.7 shows a possible EB excitation scheme in the ion ^{229}Th^{35+}. An $M1$ laser photon is absorbed by the atomic shell, which is promoted from the state at $E = 10.70$ eV to a virtual electronic level close to the real level at $E = 11.77$ eV. The successive electronic $M1 + E2$ transition to the state at $E = 3.90$ eV is coupled to the nuclear transition between the ground and the isomeric states. Since the transition energy $10.70 - 3.90 = 7.87$ eV is close to the energy of the nuclear isomer $E_m = 7.8 \pm 0.5$ eV accepted today, we can expect a considerable excitation rate in this scheme.

We proceed by deriving the expression for the EB excitation rate using the same

E (eV)	J	E (eV)	J	E (eV)	J	E (eV)	J
0.00	15/2	18.20	7/2	24.85	13/2	29.13	11/2
3.90	9/2	18.36	15/2	24.93	5/2	29.22	15/2
4.69	11/2	18.65	11/2	25.02	1/2	29.46	23/2
7.07	3/2	19.07	9/2	25.41	15/2	29.47	5/2
8.28	13/2	19.85	3/2	25.45	7/2	30.08	11/2
10.67	15/2	20.00	7/2	26.19	9/2	30.53	13/2
10.70	5/2	20.24	5/2	26.35	13/2	30.88	3/2
10.73	11/2	20.39	9/2	26.39	21/2	31.03	15/2
10.82	7/2	21.11	11/2	26.67	19/2	31.10	11/2
11.64	9/2	21.46	13/2	26.89	11/2	31.63	9/2
11.77	7/2	21.94	15/2	27.44	3/2	31.72	9/2
13.63	17/2	22.32	17/2	27.55	15/2	32.18	7/2
13.71	1/2	22.73	5/2	27.58	7/2	32.25	1/2
13.92	5/2	22.76	7/2	28.04	9/2	32.26	5/2
14.03	21/2	23.04	3/2	28.07	5/2	32.37	7/2
14.39	19/2	23.14	13/2	28.13	7/2	32.51	17/2
16.19	13/2	23.68	17/2	28.16	11/2	32.66	13/2
16.45	5/2	23.78	19/2	28.42	5/2	32.75	7/2
16.99	11/2	24.22	11/2	28.72	9/2	33.06	3/2
17.17	9/2	24.53	9/2	29.07	3/2	33.24	13/2
17.86	3/2	24.84	7/2	29.12	17/2	33.25	9/2

Table 2.4: The low-energy part of the electronic spectrum of the Th^{35+} ion containing the configuration $4f^9$. Here E is the energy of the level and J is its total angular momentum.
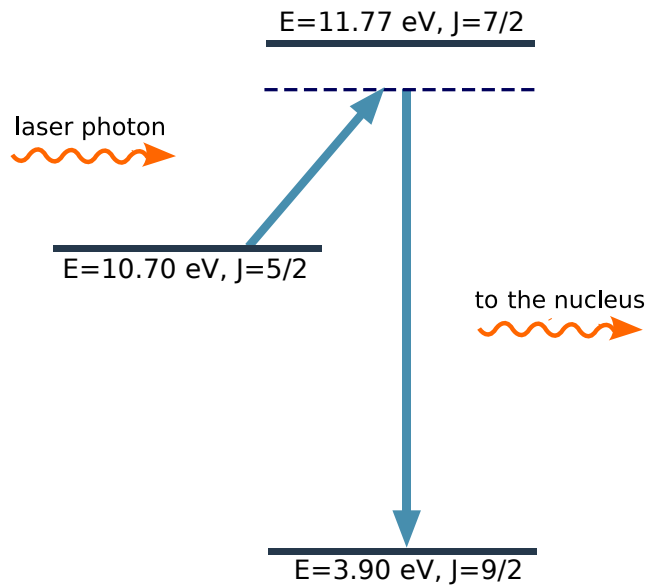

E=11.77 eV, J=7/2

laser photon

E=10.70 eV, J=5/2

to the nucleus

E=3.90 eV, J=9/2

Figure 2.7: A possible scheme of EB excitation in the $^{229}Th^{35+}$ ion. The atomic shell being initially in a state at $E = 10.70$ eV absorbs an $M1$ laser photon and is promoted to a virtual state (dashed line) close to the real level at $E = 11.77$ eV. The latter decays to a real state at $E = 3.90$ eV transferring its energy to the nucleus and exciting it to the isomeric state.

approach as for the LIEB scheme. The rate Γ_{excit} of the excitation with the initial and final electronic levels $|i\rangle$ and $|f\rangle$, respectively, can be obtained from the rate of the inverse spontaneous process Γ_{spont} with the help of the expression [74]

$$\Gamma_{\text{excit}} = \Gamma_{\text{spont}} \frac{4\pi^3 c^2 \hbar^2}{E_{\text{phot}}^3} P_\omega \delta \,, \tag{2.34}$$

where Γ_{spont} is in this case the rate of the traditional EB decay with the electronic transition from $|f\rangle$ to $|i\rangle$. The results obtained in Section 2.1 describe this spontaneous process with the only difference that the real photon has now the $M1$ type and the electric dipole operator should be replaced by the magnetic dipole operator

$$\hat{\mathbf{M}} = \frac{\alpha}{2}(\hat{\mathbf{L}} + 2\hat{\mathbf{S}}) \,, \tag{2.35}$$

where $\hat{\mathbf{L}}$ and $\hat{\mathbf{S}}$ are the orbital momentum and the spin operators, respectively. We assume that the excitation process is resonant and there is an intermediate electronic level $|n\rangle$ such that the transition energy $E_{ni} = E_n - E_i$ is close to E_m. For a first estimate of the process, we omit the contribution of other electronic (non-resonant) levels. Obviously at least the possible intermediate states within the open shell should be included at a later time for a more accurate calculation. We note that due to the higher charges involved, the sum over intermediate states is quickly converging. From the technical point of view, considering just the near resonant intermediate state allows to apply the GRASP2K package for evaluation of necessary matrix elements, which due to presence of many electrons in the outer shell cannot be obtained by direct application of the procedure described in Section 2.3 where we investigated the LIEB process. We obtain the spontaneous decay rate in the form

$$\Gamma_{\text{spont}} = \frac{4\pi\alpha^5 E_{\text{phot}}^3}{3(2J_f + 1)} \sum_{\lambda L} \frac{B_\downarrow^{\lambda L} G^{\lambda L}}{(2L + 1)^2} \,, \tag{2.36}$$

where

$$G^{\lambda L} = \frac{1}{2J_n + 1} \left| \frac{\langle \beta_i J_i \| \hat{L} + 2\hat{S} \| \beta_n J_n \rangle \langle \beta_n J_n \| \hat{\mathcal{T}}_{\lambda L} \| \beta_f J_f \rangle}{E_{ni} - E_m} \right|^2 \,. \tag{2.37}$$

The matrix element with the operator $\hat{\mathcal{T}}_{\lambda L}$ can be reduced to radial integrals of the form (2.24)—(2.25) with the integrand containing the factor $1/r^{L+1}$. As the wave functions of the outer electrons in HCI are more compact in comparison to the Th$^+$ ion, the radial integrals are larger leading to a higher EB excitation rate. On the other hand, the radial integrals corresponding to the matrix element of the operator $\hat{L} + 2\hat{S}$ in (2.35) do not contain r explicitly and do not show significant change with the charge state of the ion.

Fig. 2.8 shows the EB excitation rate Γ_{excit} as a function of the nuclear isomer energy for the scheme shown in Fig. 2.7. The matrix elements of the operator $\hat{\mathcal{T}}_{\lambda L}$ in (2.37) are calculated with the help of the program *rhfs* from the package GRASP2K. The purpose of this code is the calculation of diagonal and off-diagonal hyperfine structure constants [77] which involve diagonal and off-diagonal matrix elements of the operator $\hat{\mathcal{T}}_{\lambda L}$. The matrix elements of the operator $\hat{L} + 2\hat{S}$, responsible also for the radiative $M1$ transition between the corresponding states, are evaluated using the program *rtransition* from the GRASP2K package. In Fig. 2.8 we also depict the energy of the resonant laser photon E_{phot}. For the considered range of E_{phot} we assume the spectral power to be

$P_\omega = 2\pi \cdot 10 \ \frac{\text{W}}{\text{m}^2 \cdot \text{Hz}}$. This value can be achieved by a 30 mW laser with 100 kHz bandwidth focused to a spot of radius $\sim 10 \ \mu$m.

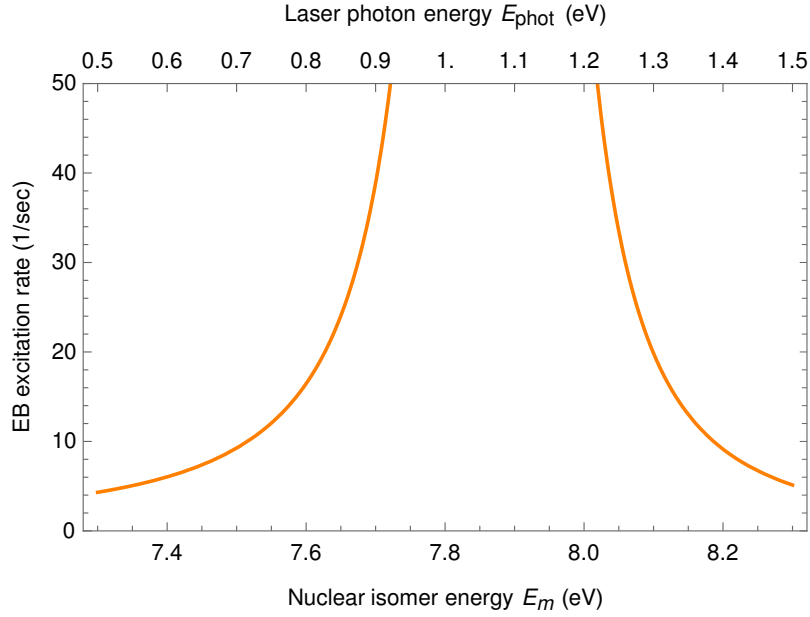**Figure 2.8:** EB excitation rate Γ_{excit} as a function of the nuclear isomer energy for the scheme 10.70 eV $\rightarrow$ 11.77 eV $\rightarrow$ 3.90 eV in the ion $^{229}\text{Th}^{35+}$ with the electronic configuration $4f^9$ (see also Fig. 2.7). The considered spectral power is $P_\omega = 2\pi \cdot 10 \ \frac{\text{W}}{\text{m}^2 \cdot \text{Hz}}$.

The scheme provides a significant excitation rate per ion in the whole range 7.8±0.5 eV, where the nuclear isomeric state energy E_m is supposed to lie. If the value of E_m happens to be higher, the considered scheme can be still applied up to the energy 9.5 eV giving a considerable excitation rate $> 0.2 \ \text{s}^{-1}$. We note that the initial electronic state here is not the ground state of $^{229}\text{Th}^{35+}$ but the sixth excited state at 10.70 eV. Our calculations with the GRASP2K package show that this state decays radiatively with the rate $\approx 40 \ \text{s}^{-1}$, which is two orders less than typical decay rate for the states in this spectrum. A possible population mechanism of this level based on long-lived electronic states of $^{229}\text{Th}^{35+}$ will be discussed later in this Section.

We present now another EB excitation scheme in the $^{229}\text{Th}^{17+}$ ion with the electronic configuration $5d^5$. The process goes subsequently through the electronic levels at the energies 9.10 eV, 9.83 eV and the ground state (see Table 2.3). The transition between the latter two levels due to the difference of the total angular momenta $9/2 - 5/2 = 2$ has the multipolarity $E2$ and couples only to the $E2$ transition in the nucleus. The EB excitation rate Γ_{excit} as a function of the nuclear isomer energy is shown in Fig. 2.9. The scheme allows to achieve a considerable excitation rate in the case when the energy E_m of the nuclear isomeric state in ^{229}Th is larger than 9.5 eV and cannot be covered by the scheme in $^{229}\text{Th}^{35+}$ considered before. The initial electronic state is the fourth excited state, which due to the difference of the total angular momenta with the lower-lying levels larger than 1, does not decay via the $M1$ radiative channel and can be considered metastable.

We consider at this point a possible way of production and trapping of HCI in the electron beam ion trap (EBIT) at the Max Planck Institute for Nuclear Physics in Heidelberg, Germany [78, 79]. Being relatively compact, this type of traps is an efficient tool for both generating and trapping ions in very high charge states by means of a focused
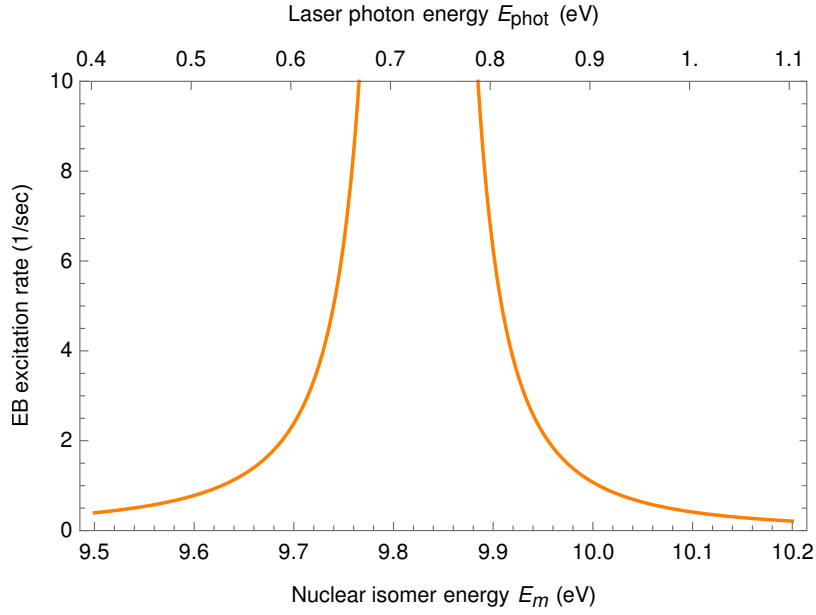
Figure 2.9: EB excitation rate Γ_{excit} as a function of the nuclear isomer energy for the scheme 9.10 eV $\rightarrow$ 9.83 eV $\rightarrow$ 0.00 eV in the ion $^{229}\text{Th}^{17+}$ with the electronic configuration $5d^5$. The considered spectral power is $P_\omega = 2\pi \cdot 10 \, \frac{\text{W}}{\text{m}^2 \cdot \text{Hz}}$.

highly energetic electron beam (see Fig. 2.10). The beam creates positively charged ions in the trap and at the same time confines them radially due to the attractive Coulomb force. The longitudinal confinement is achieved by means of three tube electrodes as shown in Fig. 2.10. The trap is placed in a strong magnetic field of superconductive coils, which compresses the electron beam in the radial direction. In this mechanism, the electronic excited states of the resulting HCI ions are populated. The states which decay fast contribute to the population of low-lying long-lived states, some of which can be used for the EB excitation schemes.

The initial relative state population of HCI in the EBIT can be evaluated with the FAC package [80] and was taken from [81]. In this calculation the electron beam density of 10^{11} cm^{-3} and the mean kinetic energy of the electrons of 1.5 keV typical for EBIT to produce Th^{35+} were considered. The results are shown in Table 2.5. The listed electronic levels have total population exceeding 99.5 %. The level at 10.70 eV used for the EB excitation scheme in $^{229}\text{Th}^{35+}$ has 1.2% of population. This value can be increased by transferring the population from the electronic state at 7.07 with laser light at the NUV wavelength of 342 nm. The described way of production and trapping of HCI would provide thus at the same time a mechanism of reaching the initial electronic states in the EB excitation schemes.

Due to the different spins and multipole moments in the nuclear ground and isomeric states, the EB excitation event is followed by a change in the hyperfine structure of the electronic levels. This feature renders possible the identification of the nuclear isomer in Th ions via an optical measurement resolving the transitions between the hyperfine sublevels. Such a direct optical identification of the ^{229}Th nuclear isomeric state in the $^{229}\text{Th}^{2+}$ ion was only recently accomplished for the first time [54]. In Table 2.6 we present the hyperfine constants A and B for the electronic levels involved in the EB excitation scheme for the $^{229}\text{Th}^{35+}$ ion, obtained using the GRASP2K package. The indices "gr" and "iso" correspond to the nucleus in the ground and the isomeric states,
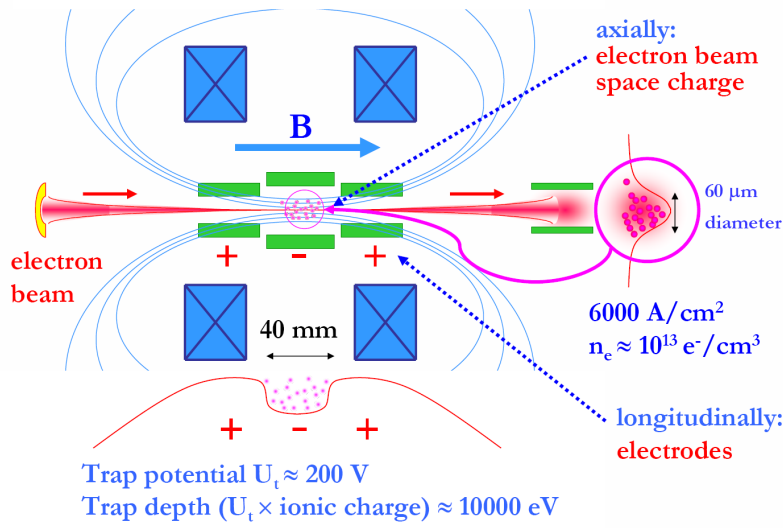
Figure 2.10: A schematic illustration of the EBIT setup at the Max Planck Institute for Nuclear Physics in Heidelberg, Germany (taken from [79]).

Energy (eV)	J	Population in %
0.00	15/2	42.4
3.90	9/2	17.9
4.69	11/2	17.4
7.07	3/2	7.1
10.70	5/2	1.2
14.03	21/2	7.7
14.39	19/2	5.7

Table 2.5: Relative population of the electronic states of ^{229}Th^{35+} ion in EBIT. The electron beam density of 10^{11} cm^{-3} and the mean kinetic energy of the electrons of 1.5 keV are considered. The shown levels have total population $> 99.5\%$.

respectively. We consider here also the electronic state at 7.07 eV as it can be used for population of the initial state in the EB scheme as mentioned above. The values of the

Energy, eV	J	A_{gr} (μeV)	B_{gr} (μeV)	A_{iso} (μeV)	B_{iso} (μeV)
3.90	9/2	2.93	-42.81	-5.02	-23.80
7.07	3/2	3.08	-65.28	-5.27	-36.29
10.70	5/2	3.58	101.83	-6.14	56.61
11.77	7/2	3.73	-15.73	-6.39	-8.74

Table 2.6: The hyperfine constants A and B for the electronic levels in the EB excitation scheme for the ^{229}Th^{35+} ion. The indices "gr" and "iso" correspond to the nucleus in the ground and the isomeric states, respectively.

hyperfine splittings allow for the identification of the nuclear isomeric state. HCI offer thus a new and efficient opportunity for EB excitation of the isomer ^{229}Th.

Chapter 3

Laser-assisted nuclear excitation by electron capture (LANEEC)

The only reliable way of production of ^{229}Th in its nuclear isomeric state remains at the moment the α-decay of ^{233}U. The produced ^{229}Th nuclei are in excited states at keV energy, which after the cascade decay result in approx. 2% population of the isomeric state [53, 54]. In the experiment described in Ref. [14, 15] the keV photons from the nuclear transitions between the levels shown in Fig. 3.1 were detected and resolved using a state-of-art X-ray microcalorimeter spectrometer, providing in this way an indirect evidence of existence of the low-lying nuclear isomer in ^{229}Th and a measurement of its energy $E_m = 7.8 \pm 0.5$ eV.
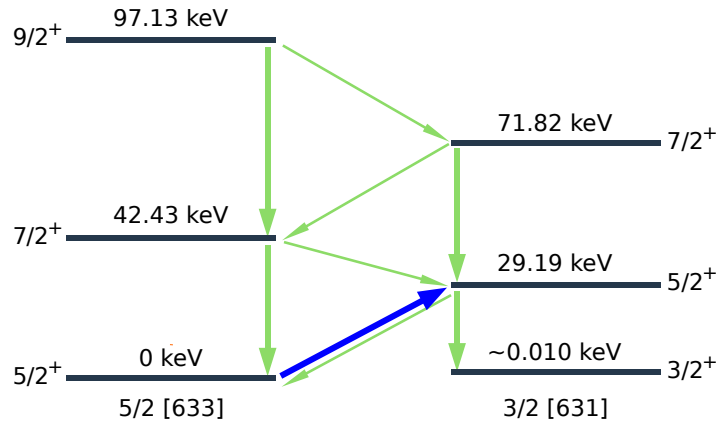
Figure 3.1: The low-lying nuclear levels of ^{229}Th shown with their energies in keV, spins and parities. The levels belong to two rotational bands denoted by their Nilsson quantum numbers. The green arrows correspond to strong intraband (thick arrows) and weaker interband (thin arrows) decays. The thick blue arrow shows the transition from the ground state to the state at 29.19 keV used in [82].

The isomeric state in this scheme is produced predominantly from the decay of the state at 29.19 keV. It has been recently proposed to excite the 29.19-keV level directly from the nuclear ground state as shown in Fig.3.1 by the thick blue arrow, using high-brilliance synchrotron radiation [82]. Taking into account the predominant decay of this level to the isomeric state, this would lead to an effective population of the nuclear isomer. The authors of Ref. [82] have demonstrated feasibility of this method for the aforementioned purpose by excitation of a similar transition in the nucleus ^{201}Hg from the ground state to the 26.27-keV level and detection of the corresponding decay signal [83].

In this Chapter we investigate an excitation scheme of the nuclear state at 29.19 keV in ^{229}Th based on the process of laser-assisted nuclear excitation by electron capture (LANEEC) illustrated in Fig. 3.2. An atomic electron absorbs an external X-ray photon and is promoted to a continuum state. As the next step the electron is captured

to a bound state with simultaneous excitation of the nucleus. The LANEEC can be schematically represented as a sequence of the photoionization process and the ordinary NEEC excitation [84–86]. On the other hand, this process is similar to the EB excitation considered in Chapter 2 with the difference that the intermediate electronic state is now not virtual but a real continuum state.
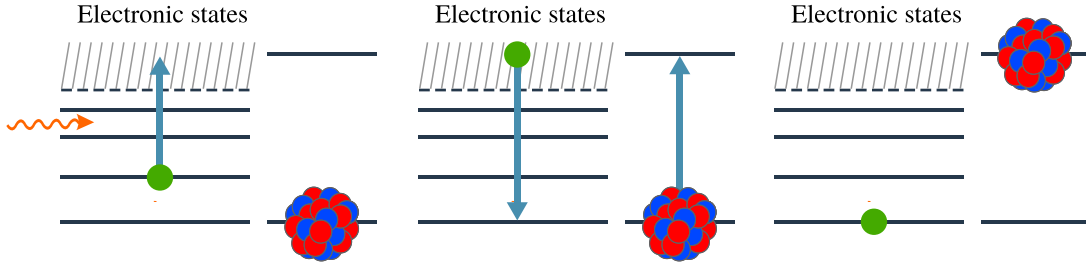

Figure 3.2: A schematic illustration of the LANEEC process. An atomic electron absorbs an X-ray photon and is promoted to a continuum state. Next, the electron is captured to a bound inner-shell state with simultaneous excitation of the nucleus.

The recombination of the continuum electron should provide sufficient energy for excitation of the nuclear state at 29.19 keV. Due to this reason, the final bound electronic state should belong to one of the inner atomic orbitals. A second X-ray beam is therefore applied in the proposed scheme in order to create a vacancy in this orbital. The considered excitation mechanism involves thus two X-ray beams at different energies.

The LANEEC process as proposed here was to the best of our knowledge never considered before. We therefore provide a rigorous analysis of LANEEC using the Feshbach projection operator formalism. The theoretical results are then applied to calculate the LANEEC excitation rate in a concrete experimental implementation at the X-ray free-electron laser SACLA located in Harima, Japan [87]. Although the calculated excitation rate turns out to be below the practical interest at the moment, a comparison to the alternative direct nonlinear excitation of the nucleus with two X-ray beams renders this scheme a demonstration of a nuclear excitation process strongly enhanced by the electronic shell and may be useful in the future in the quickly developing area of X-ray quantum optics with nuclei.

3.1 LANEEC Theory

In this Section we develop a theory of the LANEEC process. The description is based on matrix elements of the transition operator, which are obtained using the Feshbach projection operator formalism in the form described in Ref. [88], where it was applied for the dielectronic recombination process [89]. We assume that the nuclear state excited by the LANEEC decays radiatively and the final state of the system is its ground state.

Feshbach projection operator formalism

We start by introducing all possible states of an atom involved in LANEEC. In the context of the considered process, the atom is completely described by the following orthogonal sets of states.

- The subspace $\mathcal{R}$ consists of states with one photon and all electrons bound. The basis states in $\mathcal{R}$ are denoted as $|f\omega\rangle$, where ω is the total energy of the system

including the photon energy. The generic notation f contains all discrete electronic and nuclear quantum numbers representing states in the subspace $\mathcal{R}$.

- The subspace $\mathcal{P}$ includes states with no photons, one electron in a continuum state and the other electrons bound. The basis states $|\alpha\varepsilon\rangle$ are described by the total energy of the system including the energy of the continuum electron. The notation α includes all discrete electronic and nuclear quantum numbers.

- The subspace $\mathcal{Q}$ contains states with no photons and all electrons bound. The basis we denote by $|\beta\rangle$ with the generic notation β incorporating all the electronic and nuclear quantum numbers, which are discrete in this case. In this work we consider a finite number of the states $|\beta\rangle$.

In all introduced subspaces the nuclear state is not specified: the nucleus can be either in the ground or in the excited state. We assume that the discrete states have usual normalization to unity and the continuum states are normalized with respect to energy:

$$\langle\beta|\beta'\rangle = \delta_{\beta\beta'} \, , \tag{3.1}$$
$$\langle f\omega|f'\omega'\rangle = \delta_{ff'}\delta(\omega - \omega') \, , \tag{3.2}$$
$$\langle\alpha\varepsilon|\alpha'\varepsilon'\rangle = \delta_{\alpha\alpha'}\delta(\varepsilon - \varepsilon') \, . \tag{3.3}$$

In order to clearly separate the states in the derivation, we will use the projection operators onto the introduced subspaces

$$\mathcal{R} = \sum_f \int d\omega \, |f\omega\rangle \, \langle f\omega| \, , \tag{3.4}$$

$$\mathcal{P} = \sum_\alpha \int d\varepsilon \, |\alpha\varepsilon\rangle \, \langle\alpha\varepsilon| \, , \tag{3.5}$$

$$\mathcal{Q} = \sum_\beta |\beta\rangle \, \langle\beta| \tag{3.6}$$

denoted for simplicity in the same way as the corresponding subspaces. We assume that no other states participate in the considered process and thus the subspaces $\mathcal{P}, \mathcal{Q}, \mathcal{R}$ form the complete space of the states of the system, so that the unity operator can be represented as $\mathbb{1} = \mathcal{R} + \mathcal{P} + \mathcal{Q}$. We will use in the following characteristic property of projection operators: $\mathcal{R}^2 = \mathcal{R}$, $\mathcal{P}^2 = \mathcal{P}$, $\mathcal{Q}^2 = \mathcal{Q}$.

The total Hamiltonian of the system can be written as $\hat{H} = \hat{H}_0 + \hat{V}$, where $\hat{V}$ describes the interactions mixing the states from the subspaces $\mathcal{R}$, $\mathcal{P}$ and $\mathcal{Q}$, that is the coupling of the nucleus to the electronic shell and interaction of the nucleus and the electrons with the radiation field. The unperturbed Hamiltonian $\hat{H}_0$ describes the system in absence of the aforementioned interactions. The states from the subspaces $\mathcal{R}$, $\mathcal{P}$ and $\mathcal{Q}$ are the eigenstates of $\hat{H}_0$. The corresponding projection operators commute therefore with $\hat{H}_0$. We introduce Green's operator

$$\hat{G}(z) = [z - \hat{H}]^{-1} = [z - \hat{H}_0 - \hat{V}]^{-1} \, , \tag{3.7}$$

satisfying the Lippmann-Schwinger equation

$$\hat{G}(z) = \hat{G}_0(z) + \hat{G}_0(z)\hat{V}\hat{G}(z) \, , \tag{3.8}$$

where $\hat{G}_0(z)$ is Green's operator corresponding to the Hamiltonian $\hat{H}_0$

$$\hat{G}_0(z) = [z - \hat{H}_0]^{-1} \tag{3.9}$$

and z is the complex energy variable. After multiplication of the equation (3.8) by $(z - \hat{H}_0)$ from the left-hand side, it takes the equivalent form

$$(z - \hat{H}_0)\hat{G}(z) = \mathbb{1} + \hat{V}\hat{G}(z) \ . \tag{3.10}$$

We proceed by introducing another operator $\mathcal{C} = \mathcal{R} + \mathcal{Q}$, which is also a projection operator as $\mathcal{C}^2 = \mathcal{C}$ due to the orthogonality of the subspaces $\mathcal{R}$ and $\mathcal{Q}$. Acting subsequently with the operators $\mathcal{P}$ and $\mathcal{C}$ on Eq. (3.10) from the left and from the right, we obtain the following four relations

$$\begin{align}
(z - \hat{H}_0)\mathcal{P}\hat{G}(z)\mathcal{C} &= \mathcal{P}\hat{V}\hat{G}(z)\mathcal{C} \ , \tag{3.11} \\
(z - \hat{H}_0)\mathcal{C}\hat{G}(z)\mathcal{P} &= \mathcal{C}\hat{V}\hat{G}(z)\mathcal{P} \ , \tag{3.12} \\
(z - \hat{H}_0)\mathcal{P}\hat{G}(z)\mathcal{P} &= \mathcal{P} + \mathcal{P}\hat{V}\hat{G}(z)\mathcal{P} \ , \tag{3.13} \\
(z - \hat{H}_0)\mathcal{C}\hat{G}(z)\mathcal{C} &= \mathcal{C} + \mathcal{C}\hat{V}\hat{G}(z)\mathcal{C} \ , \tag{3.14}
\end{align}$$

which after inserting the unity operator $\mathbb{1} = \mathcal{R} + \mathcal{P} + \mathcal{Q} = \mathcal{P} + \mathcal{C}$ between $\hat{V}$ and $\hat{G}(z)$ become

$$\begin{align}
(z - \hat{H}_0)\mathcal{P}\hat{G}(z)\mathcal{C} &= \mathcal{P}\hat{V}\mathcal{P}\hat{G}(z)\mathcal{C} + \mathcal{P}\hat{V}\mathcal{C}\hat{G}(z)\mathcal{C} \ , \tag{3.15} \\
(z - \hat{H}_0)\mathcal{C}\hat{G}(z)\mathcal{P} &= \mathcal{C}\hat{V}\mathcal{P}\hat{G}(z)\mathcal{P} + \mathcal{C}\hat{V}\mathcal{C}\hat{G}(z)\mathcal{P} \ , \tag{3.16} \\
(z - \hat{H}_0)\mathcal{P}\hat{G}(z)\mathcal{P} &= \mathcal{P} + \mathcal{P}\hat{V}\mathcal{P}\hat{G}(z)\mathcal{P} + \mathcal{P}\hat{V}\mathcal{C}\hat{G}(z)\mathcal{P} \ , \tag{3.17} \\
(z - \hat{H}_0)\mathcal{C}\hat{G}(z)\mathcal{C} &= \mathcal{C} + \mathcal{C}\hat{V}\mathcal{P}\hat{G}(z)\mathcal{C} + \mathcal{C}\hat{V}\mathcal{C}\hat{G}(z)\mathcal{C} \ . \tag{3.18}
\end{align}$$

Next, we rewrite the equations (3.15)—(3.16) as

$$\begin{align}
\mathcal{P}\hat{G}(z)\mathcal{C} &= [\mathcal{P}\hat{G}(z)\mathcal{P}]V[\mathcal{C}\hat{\Phi}(z)\mathcal{C}] \ , \tag{3.19} \\
\mathcal{C}\hat{G}(z)\mathcal{P} &= [\mathcal{C}\hat{\Phi}(z)\mathcal{C}]\hat{V}[\mathcal{P}\hat{G}(z)\mathcal{P}] \ , \tag{3.20}
\end{align}$$

where the operator $\hat{\Phi}(z)$ is defined as

$$\hat{\Phi}(z) = \mathcal{C}[\mathcal{C}(z - \hat{H}_0 - \hat{V})\mathcal{C}]^{-1}\mathcal{C} \ . \tag{3.21}$$

Then substituting (3.19)—(3.20) into (3.17)—(3.18), we find

$$\begin{align}
\mathcal{P}\hat{G}(z)\mathcal{P} &= \mathcal{P}[\mathcal{P}(z - \hat{H}_0 - \hat{\Lambda}(z))\mathcal{P}]^{-1}\mathcal{P} \ , \tag{3.22} \\
\mathcal{C}\hat{G}(z)\mathcal{C} &= \mathcal{C}\hat{\Phi}(z)\mathcal{C}[\mathbb{1} + \hat{V}\mathcal{P}\hat{G}(z)\mathcal{C}] \ , \tag{3.23}
\end{align}$$

where

$$\hat{\Lambda}(z) = \hat{V} + \hat{V}\mathcal{C}\hat{\Phi}(z)\mathcal{C}\hat{V} \ . \tag{3.24}$$

We note that strictly speaking the inverse of the operator $\mathcal{C}(z - \hat{H}_0 - \hat{V})\mathcal{C}$ in (3.21) does not exist in the complete space. Indeed, any two vectors $|\psi_1\rangle$ and $|\psi_2\rangle$ are mapped by this operator to the same vector $|\varphi\rangle$ from the subspace $\mathcal{C}$, if their difference $|\psi_1\rangle - |\psi_2\rangle$ is orthogonal to $\mathcal{C}$. The object $[\mathcal{C}(z - \hat{H}_0 - \hat{V})\mathcal{C}]^{-1}$ maps back each vector $|\phi\rangle$ from $\mathcal{C}$ to an infinite number of vectors $|\psi\rangle$ and is thus not an operator in its common sense. The operator $\hat{\Phi}(z)$ is in turn correctly defined by (3.21) due to presence of the two additional

operators $\mathcal{C}$. The right one insures that the object $[\mathcal{C}(z - \hat{H}_0 - \hat{V})\mathcal{C}]^{-1}$ is applied only to the states from $\mathcal{C}$, whereas the left operator $\mathcal{C}$ projects the infinite number of vectors on a unique vector from the subspace $\mathcal{C}$. In the same way it can be argued that the operator on the right-hand side of the equation (3.22) is correctly defined.

The LANEEC process can be described within this framework by the transition operator

$$\hat{T}(z) = \hat{V} + \hat{V}\hat{G}(z)\hat{V} . \tag{3.25}$$

The excitation rate can be obtained with the help of matrix elements of $\hat{T}(z)$. Using the equations (3.19)—(3.23), $\hat{T}(z)$ can be represented as

$$\hat{T}(z) = \hat{\Lambda}(z) + \hat{\Lambda}(z)\mathcal{P}\hat{G}(z)\mathcal{P}\hat{\Lambda}(z) . \tag{3.26}$$

The initial state of the system and its final state after radiative decay of the nuclear excited state belong to the subspace $\mathcal{R}$. We restrict thus our consideration to the operator $\mathcal{R}\hat{T}(z)\mathcal{R}$, which with (3.26) can be written as

$$\mathcal{R}\hat{T}(z)\mathcal{R} = \mathcal{R}\hat{\Lambda}(z)\mathcal{R} + \mathcal{R}\hat{\Lambda}(z)\mathcal{P}\hat{G}(z)\mathcal{P}\hat{\Lambda}(z)\mathcal{R} . \tag{3.27}$$

The term $\mathcal{R}\hat{\Lambda}(z)\mathcal{R}$ does not contain the projection operator $\mathcal{P}$ onto the subspace containing the states with a continuum electron. We conclude therefore that it corresponds to the absorption of a photon promoting the system only between its bound states. We omit this term as we are interested in the LANEEC process, which involves continuum electronic states. We obtain

$$\mathcal{R}\hat{T}(z)\mathcal{R} = [\mathcal{R}\hat{\Lambda}(z)\mathcal{P}][\mathcal{P}\hat{G}(z)\mathcal{P}][\mathcal{P}\hat{\Lambda}(z)\mathcal{R}] . \tag{3.28}$$

The operator $\mathcal{P}\hat{G}(z)\mathcal{P}$ in (3.28) is given by the equation (3.22) and can be expressed through $\mathcal{P}\hat{\Lambda}(z)\mathcal{P}$. We see thus, that the LANEEC description reduces to the projections of the operator $\hat{\Lambda}(z)$, which with the help of the definition (3.24) can be expressed via $\mathcal{C}\hat{\Phi}(z)\mathcal{C}$. The latter operator in turn splits into four terms as

$$\mathcal{C}\hat{\Phi}(z)\mathcal{C} = \mathcal{Q}\hat{\Phi}(z)\mathcal{Q} + \mathcal{Q}\hat{\Phi}(z)\mathcal{R} + \mathcal{R}\hat{\Phi}(z)\mathcal{Q} + \mathcal{R}\hat{\Phi}(z)\mathcal{R} . \tag{3.29}$$

We assume at this point that the interaction $\hat{V}$ does not couple different continuum states belonging to the same subspace with each other and use in the following $\mathcal{R}\hat{V}\mathcal{R} = 0$ and $\mathcal{P}\hat{V}\mathcal{P} = 0$. This approximation is justified as we do not consider here the processes of photon and electron scattering. Rewriting the expression (3.21) in the form

$$(z - \hat{H}_0)\mathcal{C}\hat{\Phi}(z)\mathcal{C} = \mathcal{C} + \mathcal{C}\hat{V}\mathcal{C}\hat{\Phi}(z)\mathcal{C} , \tag{3.30}$$

acting subsequently with the operators $\mathcal{Q}$ and $\mathcal{R}$ on its left- and right-hand side and taking into account $\mathcal{C} = \mathcal{R} + \mathcal{Q}$, we obtain

$$\begin{aligned}
(z - \hat{H}_0)\mathcal{Q}\hat{\Phi}(z)\mathcal{Q} &= \mathcal{Q} + \mathcal{Q}\hat{V}\mathcal{Q}\hat{\Phi}(z)\mathcal{Q} + \mathcal{Q}\hat{V}\mathcal{R}\hat{\Phi}(z)\mathcal{Q} , \tag{3.31} \\
(z - \hat{H}_0)\mathcal{R}\hat{\Phi}(z)\mathcal{Q} &= \mathcal{R}\hat{V}\mathcal{Q}\hat{\Phi}(z)\mathcal{Q} , \tag{3.32} \\
(z - \hat{H}_0)\mathcal{Q}\hat{\Phi}(z)\mathcal{R} &= \mathcal{Q}\hat{V}\mathcal{Q}\hat{\Phi}(z)\mathcal{R} + \mathcal{Q}\hat{V}\mathcal{R}\hat{\Phi}(z)\mathcal{R} , \tag{3.33} \\
(z - \hat{H}_0)\mathcal{R}\hat{\Phi}(z)\mathcal{R} &= \mathcal{R} + \mathcal{R}\hat{V}\mathcal{Q}\hat{\Phi}(z)\mathcal{R} . \tag{3.34}
\end{aligned}$$

Substituting $\mathcal{R}\hat{\Phi}(z)\mathcal{Q}$ from (3.32) into (3.31) and using the definition (3.9) of Green's

operator $\hat{G}_0(z)$, we find

$$\mathcal{Q}[z - \hat{H}_0 - \hat{V} - \hat{V}\mathcal{R}\hat{G}_0(z)\mathcal{R}\hat{V}][\mathcal{Q}\hat{\Phi}(z)\mathcal{Q}] = \mathcal{Q} . \tag{3.35}$$

By substitution of (3.34) into (3.33) and using (3.35), we obtain

$$\mathcal{Q}\hat{\Phi}(z)\mathcal{R}(z - \hat{H}_0) = [\mathcal{Q}\hat{\Phi}(z)\mathcal{Q}][\mathcal{Q}\hat{V}\mathcal{R}] . \tag{3.36}$$

Expressing $\mathcal{Q}\hat{\Phi}(z)\mathcal{Q}$ from (3.35), it is possible to find the other three operators in (3.29) using subsequently the relations (3.36), (3.32) and (3.34). We follow this line switching first from the operators to their matrix elements.

Matrix elements of the operators $\hat{\Phi}(z)$ and $\hat{\Lambda}(z)$

First, we take matrix element $\langle \beta | \cdot | \beta' \rangle$ from the expression (3.35) obtaining

$$(z - E_\beta^0) \langle \beta | \hat{\Phi}(z) | \beta' \rangle - \langle \beta | \hat{V}\mathcal{Q}\hat{\Phi}(z) | \beta' \rangle - \langle \beta | \hat{V}\hat{G}_0(z)\mathcal{R}\hat{V}\mathcal{Q}\hat{\Phi}(z) | \beta' \rangle = \delta_{\beta\beta'} . \tag{3.37}$$

We have used here that the state $|\beta\rangle$ is the eigenstate of the unperturbed Hamiltonian $\hat{H}_0$ with the eigenvalue E_β^0. Inserting the operators $\mathcal{R}$ and $\mathcal{Q}$ in the form (3.4) and (3.6) respectively, we find

$$(z - E_\beta^0) \langle \beta | \hat{\Phi}(z) | \beta' \rangle - \sum_{\beta''} \langle \beta | \hat{V} | \beta'' \rangle \langle \beta'' | \hat{\Phi}(z) | \beta' \rangle$$

$$-\sum_{\beta''f} \int d\omega \frac{\langle \beta | \hat{V} | f\omega \rangle \langle f\omega | \hat{V} | \beta'' \rangle \langle \beta'' | \hat{\Phi}(z) | \beta' \rangle}{z - \omega} = \delta_{\beta\beta'} , \tag{3.38}$$

where we have taken into account

$$\hat{G}_0(z) |f\omega\rangle = \frac{1}{z - \omega} |f\omega\rangle . \tag{3.39}$$

We are interested in the values z having the form $z = \lim_{\delta \to +0} (\omega_p + i\delta)$ at some energy ω_p. For such z we can use the expression

$$\lim_{\delta \to +0} \frac{1}{\omega_p + i\delta - \omega} = \left(\frac{1}{\omega_p - \omega} \right)_{\text{p.p.}} - i\pi\delta(\omega_p - \omega) , \tag{3.40}$$

relating the integral functional in the left-hand side with its principal part (p.p.) and the corresponding Dirac delta-function. Following Ref. [88], we neglect the contribution of the principal part in this work referring to this approximation as to the pole approximation.

The expression (3.38) in the pole approximation becomes

$$(z - E_\beta^0) \langle \beta | \hat{\Phi}(z) | \beta' \rangle - \sum_{\beta''} \langle \beta | \hat{V} | \beta'' \rangle \langle \beta'' | \hat{\Phi}(z) | \beta' \rangle$$

$$+i\pi \sum_{\beta''f} \langle \beta | \hat{V} | f\omega_p \rangle \langle f\omega_p | \hat{V} | \beta'' \rangle \langle \beta'' | \hat{\Phi}(z) | \beta' \rangle = \delta_{\beta\beta'} . \tag{3.41}$$

Let us define the operators $\hat{U}$ and $\hat{W}$ as

$$\hat{U} = -i\pi\hat{V}\sum_f |f\omega_p\rangle\langle f\omega_p|\hat{V} , \tag{3.42}$$

$$\hat{W} = \hat{V} + \hat{U} . \tag{3.43}$$

Then the equation (3.41) can be rewritten as

$$(z - E_\beta^0)\langle\beta|\hat{\Phi}(z)|\beta'\rangle - \sum_{\beta''}\langle\beta|\hat{W}|\beta''\rangle\langle\beta''|\hat{\Phi}(z)|\beta'\rangle = \delta_{\beta\beta'} \tag{3.44}$$

or in the equivalent form

$$\sum_{\beta''}\langle\beta|z - \hat{H}_0 - \hat{W}|\beta''\rangle\langle\beta''|\hat{\Phi}(z)|\beta'\rangle = \delta_{\beta\beta'} . \tag{3.45}$$

The matrix elements $\langle\beta|\hat{\Phi}(z)|\beta'\rangle$ can be then found as

$$\langle\beta|\hat{\Phi}(z)|\beta'\rangle = \widetilde{G}_{\beta\beta'} , \tag{3.46}$$

where the matrix $\widetilde{G}$ is defined as the inverse of the matrix $z - \hat{H}_0 - \hat{W}$ in the subspace $\mathcal{Q}$. The choice of notation is motivated by the physical meaning of $\widetilde{G}$, namely, it is Green's operator corresponding to the Hamiltonian $\hat{H}_0 + \hat{W}$. We suppose in this work that the atom can be in a finite number of states $|\beta\rangle$. Under this assumption, the restriction of the operator $z - \hat{H}_0 - \hat{W}$ onto the subspace $\mathcal{Q}$ is a finite-dimensional matrix and can be thus inverted in a straightforward way.

We proceed by taking the matrix elements $\langle\beta|\cdot|f\omega\rangle$ and $\langle f\omega|\cdot|\beta\rangle$ from (3.36) and (3.32) respectively obtaining the expressions

$$\langle\beta|\hat{\Phi}(z)|f\omega\rangle = \frac{1}{z-\omega}\sum_{\beta'}\langle\beta|\hat{\Phi}(z)|\beta'\rangle\langle\beta'|\hat{V}|f\omega\rangle , \tag{3.47}$$

$$\langle f\omega|\hat{\Phi}(z)|\beta\rangle = \frac{1}{z-\omega}\sum_{\beta'}\langle f\omega|\hat{V}|\beta'\rangle\langle\beta'|\hat{\Phi}(z)|\beta\rangle , \tag{3.48}$$

which in the pole approximation and after using (3.46) take the form

$$\langle\beta|\hat{\Phi}(z)|f\omega\rangle = -i\pi\delta(\omega-\omega_p)\sum_{\beta'}\widetilde{G}_{\beta\beta'}\langle\beta'|\hat{V}|f\omega_p\rangle , \tag{3.49}$$

$$\langle f\omega|\hat{\Phi}(z)|\beta\rangle = -i\pi\delta(\omega-\omega_p)\sum_{\beta'}\langle f\omega_p|\hat{V}|\beta'\rangle\widetilde{G}_{\beta'\beta} . \tag{3.50}$$

Taking now the matrix elements $\langle f\omega|\cdot|f'\omega'\rangle$ from (3.34), applying again the pole approximation and using the result (3.49), we obtain

$$\langle f\omega|\hat{\Phi}(z)|f'\omega'\rangle = -i\pi\delta(\omega-\omega_p)\delta(\omega'-\omega_p)$$
$$\times\left[\delta_{ff'} - i\pi\sum_{\beta\beta'}\langle f\omega_p|\hat{V}|\beta\rangle\widetilde{G}_{\beta\beta'}\langle\beta'|\hat{V}|f'\omega_p\rangle\right] . \tag{3.51}$$

As mentioned above, the description of the LANEEC process reduces to the projections of the operator $\hat{\Lambda}(z)$, which in turn can be expressed via the operators $\mathcal{Q}\hat{\Phi}(z)\mathcal{Q}$, $\mathcal{Q}\hat{\Phi}(z)\mathcal{R}$,

$\mathcal{R}\hat{\Phi}(z)\mathcal{Q}$ and $\mathcal{R}\hat{\Phi}(z)\mathcal{R}$ determined by their matrix elements given by (3.46) and (3.49)—(3.51). Next, we derive the matrix elements of the operators $\mathcal{R}\hat{\Lambda}(z)\mathcal{P}$, $\mathcal{P}\hat{\Lambda}(z)\mathcal{R}$ and $\mathcal{P}\hat{\Lambda}(z)\mathcal{P}$ necessary for the LANEEC description. We start from the equations

$$
\begin{align}
\mathcal{R}\hat{\Lambda}(z)\mathcal{P} &= \mathcal{R}\hat{V}\mathcal{P} + \mathcal{R}\hat{V}\mathcal{Q}\hat{\Phi}(z)\mathcal{Q}\hat{V}\mathcal{P} + \mathcal{R}\hat{V}\mathcal{Q}\hat{\Phi}(z)\mathcal{R}\hat{V}\mathcal{P} , \tag{3.52} \\
\mathcal{P}\hat{\Lambda}(z)\mathcal{R} &= \mathcal{P}\hat{V}\mathcal{R} + \mathcal{P}\hat{V}\mathcal{Q}\hat{\Phi}(z)\mathcal{Q}\hat{V}\mathcal{R} + \mathcal{P}\hat{V}\mathcal{R}\hat{\Phi}(z)\mathcal{Q}\hat{V}\mathcal{R} , \tag{3.53} \\
\mathcal{P}\hat{\Lambda}(z)\mathcal{P} &= \mathcal{P}\hat{V}\mathcal{Q}\hat{\Phi}(z)\mathcal{Q}\hat{V}\mathcal{P} + \mathcal{P}\hat{V}\mathcal{Q}\hat{\Phi}(z)\mathcal{R}\hat{V}\mathcal{P} \\
&+ \mathcal{P}\hat{V}\mathcal{R}\hat{\Phi}(z)\mathcal{Q}\hat{V}\mathcal{P} + \mathcal{P}\hat{V}\mathcal{R}\hat{\Phi}(z)\mathcal{R}\hat{V}\mathcal{P} \tag{3.54}
\end{align}
$$

obtained from the definition of $\hat{\Lambda}(z)$ in (3.24) and taking into account $\mathcal{R}\hat{V}\mathcal{R} = 0$ and $\mathcal{P}\hat{V}\mathcal{P} = 0$. We consider first the equation (3.52). Taking the matrix element $\langle f\omega| \cdot |\alpha\varepsilon\rangle$, we obtain the expression

$$
\begin{align}
\langle f\omega| \hat{\Lambda}(z) |\alpha\varepsilon\rangle &= \langle f\omega| \hat{V} |\alpha\varepsilon\rangle \\
&+ \langle f\omega| \hat{V}\mathcal{Q}\hat{\Phi}(z)\mathcal{Q}\hat{V} |\alpha\varepsilon\rangle + \langle f\omega| \hat{V}\mathcal{Q}\hat{\Phi}(z)\mathcal{R}\hat{V} |\alpha\varepsilon\rangle , \tag{3.55}
\end{align}
$$

which after substitution of the operators $\mathcal{R}$ and $\mathcal{Q}$ in the representation (3.4) and (3.6) respectively, takes the form

$$
\begin{align}
\langle f\omega| \hat{\Lambda}(z) |\alpha\varepsilon\rangle &= \langle f\omega| \hat{V} |\alpha\varepsilon\rangle \\
&+ \sum_{\beta\beta'} \langle f\omega| \hat{V} |\beta\rangle \langle\beta| \hat{\Phi}(z) |\beta'\rangle \langle\beta'| \hat{V} |\alpha\varepsilon\rangle \\
&+ \sum_{\beta f'} \int d\omega' \langle f\omega| \hat{V} |\beta\rangle \langle\beta| \hat{\Phi}(z) |f'\omega'\rangle \langle f'\omega'| \hat{V} |\alpha\varepsilon\rangle . \tag{3.56}
\end{align}
$$

Using here the matrix elements of the operator $\hat{\Phi}(z)$ given by the expressions (3.46) and (3.49), we obtain

$$
\langle f\omega| \hat{\Lambda}(z) |\alpha\varepsilon\rangle = \langle f\omega| \hat{V} |\alpha\varepsilon\rangle + \sum_{\beta\beta'} \langle f\omega| \hat{V} |\beta\rangle \widetilde{G}_{\beta\beta'} \langle\beta'| \hat{W} |\alpha\varepsilon\rangle , \tag{3.57}
$$

where the operator $\hat{W}$ is defined by (3.42)—(3.43). Analogously we find the matrix elements of the operators $\mathcal{P}\hat{\Lambda}(z)\mathcal{R}$ and $\mathcal{P}\hat{\Lambda}(z)\mathcal{P}$

$$
\begin{align}
\langle\alpha\varepsilon| \hat{\Lambda}(z) |f\omega\rangle &= \langle\alpha\varepsilon| \hat{V} |f\omega\rangle + \sum_{\beta\beta'} \langle\alpha\varepsilon| \hat{W} |\beta\rangle \widetilde{G}_{\beta\beta} \langle\beta'| \hat{V} |f\omega\rangle , \tag{3.58} \\
\langle\alpha\varepsilon| \hat{\Lambda}(z) |\alpha'\varepsilon'\rangle &= \langle\alpha\varepsilon| \hat{U} |\alpha'\varepsilon'\rangle + \sum_{\beta\beta'} \langle\alpha\varepsilon| \hat{W} |\beta\rangle \widetilde{G}_{\beta\beta'} \langle\beta'| \hat{W} |\alpha'\varepsilon'\rangle . \tag{3.59}
\end{align}
$$

Matrix elements of the operators $\hat{G}(z)$ and $\hat{T}(z)$

We have obtained the matrix elements of the operators $\mathcal{R}\hat{\Lambda}(z)\mathcal{P}$ and $\mathcal{P}\hat{\Lambda}(z)\mathcal{R}$ required for the description of the LANEEC process accordingly to the expression (3.28). We proceed by deriving the matrix elements of the other operator $\mathcal{P}\hat{G}(z)\mathcal{P}$ in Eq. (3.28). Let us denote

$$
\hat{\Pi}(z) = \mathcal{P}[z - \hat{H}_0 - \mathcal{P}\hat{\Lambda}(z)\mathcal{P}]\mathcal{P} . \tag{3.60}
$$

Then the operator $\mathcal{P}\hat{G}(z)\mathcal{P}$ in accordance with (3.22) can be found as

$$
\mathcal{P}\hat{G}(z)\mathcal{P} = \mathcal{P}\hat{\Pi}(z)^{-1}\mathcal{P} . \tag{3.61}
$$

We note that in the general case the inverse of the operator $\hat{\Pi}(z)$ does not exist, whereas the object on the right-hand side in (3.61) is a well defined operator. We will refer to the notation $\hat{\Pi}(z)^{-1}$ in the following, taking into account that it is justified only in the context of the equation (3.61).

Using the representation (3.5) of the projector $\mathcal{P}$, we rewrite the operator $\hat{\Pi}(z)$ in the form

$$\hat{\Pi}(z) = \sum_{\alpha\alpha'} \int d\varepsilon d\varepsilon' \pi_{\alpha\alpha'}(\varepsilon, \varepsilon') \ket{\alpha\varepsilon} \bra{\alpha'\varepsilon} \ , \tag{3.62}$$

where the kernel π is given by the expression

$$\pi_{\alpha\alpha'}(\varepsilon, \varepsilon') = (z - \varepsilon)\delta_{\alpha\alpha'}\delta(\varepsilon - \varepsilon') - \bra{\alpha\varepsilon} \hat{\Lambda}(z) \ket{\alpha'\varepsilon'} \ . \tag{3.63}$$

The kernel of the inverse operator $\pi_{\alpha\alpha'}^{-1}(\varepsilon, \varepsilon')$ has to satisfy the condition

$$\sum_{\alpha'} \int d\varepsilon' \pi_{\alpha\alpha'}(\varepsilon, \varepsilon') \pi_{\alpha'\alpha''}^{-1}(\varepsilon', \varepsilon'') = \delta_{\alpha\alpha''}\delta(\varepsilon - \varepsilon'') \ , \tag{3.64}$$

which in our case takes the form

$$(z - \varepsilon)\pi_{\alpha\alpha''}^{-1}(\varepsilon, \varepsilon'') - \sum_{\alpha'} \int d\varepsilon' \bra{\alpha\varepsilon} \hat{\Lambda}(z) \ket{\alpha'\varepsilon'} \pi_{\alpha'\alpha''}^{-1}(\varepsilon', \varepsilon'') = \delta_{\alpha\alpha''}\delta(\varepsilon - \varepsilon'') \ . \tag{3.65}$$

We solve this integral equation using the ansatz

$$\pi_{\alpha\alpha''}^{-1}(\varepsilon, \varepsilon'') = \frac{\delta_{\alpha\alpha''}\delta(\varepsilon - \varepsilon'')}{z - \varepsilon''} + \frac{\phi_{\alpha\alpha''}(\varepsilon, \varepsilon'')}{(z - \varepsilon)(z - \varepsilon'')} \ , \tag{3.66}$$

where the first term is the exact solution in absence of the perturbation $\hat{V}$, that is for $\bra{\alpha\varepsilon} \hat{\Lambda}(z) \ket{\alpha'\varepsilon'} = 0$. Substituting (3.66) into (3.65), we obtain an equivalent integral equation

$$\phi_{\alpha\alpha''}(\varepsilon, \varepsilon'') - \bra{\alpha\varepsilon} \hat{\Lambda}(z) \ket{\alpha''\varepsilon''} = \sum_{\alpha'} \int d\varepsilon' \frac{\bra{\alpha\varepsilon} \hat{\Lambda}(z) \ket{\alpha'\varepsilon'} \phi_{\alpha'\alpha''}(\varepsilon', \varepsilon'')}{z - \varepsilon'} \tag{3.67}$$

which we solve by expansion of the function ϕ in a power series of $\hat{\Lambda}(z)$

$$\phi = \sum_n \phi^{(n)} \ , \tag{3.68}$$

where $\phi^{(n)}$ denotes the term containing $\hat{\Lambda}(z)$ n times. From the definition of the function ϕ given by (3.66) follows that $\phi^{(0)} \equiv 0$. Keeping in (3.67) the terms linear in $\hat{\Lambda}(z)$, we find

$$\phi_{\alpha\alpha''}^{(1)}(\varepsilon, \varepsilon'') = \bra{\alpha\varepsilon} \hat{\Lambda}(z) \ket{\alpha''\varepsilon''} \ . \tag{3.69}$$

For $n \geq 2$, the expression (3.67) can be written in the iterative form

$$\phi_{\alpha\alpha''}^{(n)}(\varepsilon, \varepsilon'') = \sum_{\alpha'} \int d\varepsilon' \frac{\bra{\alpha\varepsilon} \hat{\Lambda}(z) \ket{\alpha'\varepsilon'} \phi_{\alpha'\alpha''}^{(n-1)}(\varepsilon', \varepsilon'')}{z - \varepsilon'} \ , \tag{3.70}$$

where only the terms with $\hat{\Lambda}(z)$ in the n-th power are preserved. Using (3.70), we find

the second term of the expansion (3.68)

$$\phi_{\alpha\alpha''}^{(2)}(\varepsilon, \varepsilon'') = \sum_{\alpha'} \int d\varepsilon' \frac{\langle\alpha\varepsilon|\,\hat\Lambda(z)\,|\alpha'\varepsilon'\rangle\,\langle\alpha'\varepsilon'|\,\hat\Lambda(z)\,|\alpha''\varepsilon''\rangle}{z - \varepsilon'} \;, \tag{3.71}$$

which after application of the pole approximation becomes

$$\phi_{\alpha\alpha''}^{(2)}(\varepsilon, \varepsilon'') = -i\pi \sum_{\alpha'} \langle\alpha\varepsilon|\,\hat\Lambda(z)\,|\alpha'\omega_p\rangle\,\langle\alpha'\omega_p|\,\hat\Lambda(z)\,|\alpha''\varepsilon''\rangle \;. \tag{3.72}$$

Carrying out iteratively the same procedure, we find the general term of the expansion for $n \geq 2$

$$\phi_{\alpha\alpha'}^{(n)}(\varepsilon, \varepsilon') = (-i\pi)^{n-1} \sum_{\alpha_1\alpha_2\ldots\alpha_{n-1}} \langle\alpha\varepsilon|\,\hat\Lambda(z)\,|\alpha_1\omega_p\rangle$$

$$\times \langle\alpha_1\omega_p|\,\hat\Lambda(z)\,|\alpha_2\omega_p\rangle \ldots \langle\alpha_{n-2}\omega_p|\,\hat\Lambda(z)\,|\alpha_{n-1}\omega_p\rangle\,\langle\alpha_{n-1}\omega_p|\,\hat\Lambda(z)\,|\alpha'\varepsilon'\rangle \;. \tag{3.73}$$

Next, we introduce the matrix $\widetilde{X}$ with matrix elements

$$\widetilde{X}_{\alpha_1\alpha_2} = -i\pi\,\langle\alpha_1\omega_p|\,\hat\Lambda(z)\,|\alpha_2\omega_p\rangle \;. \tag{3.74}$$

The general term (3.73) for $n \geq 2$ can be then rewritten in the form

$$\phi_{\alpha\alpha'}^{(n)}(\varepsilon, \varepsilon') = -i\pi \sum_{\alpha_1\alpha_2} \langle\alpha\varepsilon|\,\hat\Lambda(z)\,|\alpha_1\omega_p\rangle \left[\widetilde{X}^{n-2}\right]_{\alpha_1\alpha_2} \langle\alpha_2\omega_p|\,\hat\Lambda(z)\,|\alpha'\varepsilon'\rangle \tag{3.75}$$

and the full solution $\phi_{\alpha\alpha'}(\varepsilon, \varepsilon')$ is given by the expression

$$\phi_{\alpha\alpha'}(\varepsilon, \varepsilon') = \langle\alpha\varepsilon|\,\hat\Lambda(z)\,|\alpha'\varepsilon'\rangle - i\pi \sum_{\alpha_1\alpha_2} \langle\alpha\varepsilon|\,\hat\Lambda(z)\,|\alpha_1\omega_p\rangle$$

$$\times \left[\sum_{n=0}^{\infty} \widetilde{X}^n\right]_{\alpha_1\alpha_2} \langle\alpha_2\omega_p|\,\hat\Lambda(z)\,|\alpha'\varepsilon'\rangle \;, \tag{3.76}$$

which by means of (3.66) determines the inverse kernel π^{-1}. Applying the pole approximation in (3.66), we find

$$\pi_{\alpha\alpha'}^{-1}(\varepsilon, \varepsilon') = -i\pi\delta(\varepsilon - \omega_p)\delta(\varepsilon' - \omega_p)\left[\delta_{\alpha\alpha'} - i\pi\phi_{\alpha\alpha'}(\omega_p, \omega_p)\right] \;. \tag{3.77}$$

Substituting $\phi_{\alpha\alpha'}(\omega_p, \omega_p)$ given by the expression (3.76) at $\varepsilon = \varepsilon' = \omega_p$ into (3.77), we obtain

$$\pi_{\alpha\alpha'}^{-1}(\varepsilon, \varepsilon') = -i\pi\delta(\varepsilon - \omega_p)\delta(\varepsilon' - \omega_p)\left[\sum_{n=0}^{\infty} \widetilde{X}^n\right]_{\alpha\alpha'} \;. \tag{3.78}$$

Taking $\langle\alpha\varepsilon|\cdot|\alpha'\varepsilon'\rangle$ from (3.61), we see that the obtained function $\pi_{\alpha\alpha'}^{-1}(\varepsilon, \varepsilon')$ is the matrix element of the operator $\hat{G}(z)$

$$\langle\alpha\varepsilon|\,\hat{G}(z)\,|\alpha'\varepsilon'\rangle = \pi_{\alpha\alpha'}^{-1}(\varepsilon, \varepsilon') \;. \tag{3.79}$$

Using the obtained results, we find at this point the matrix elements of the operator $\mathcal{R}\hat{T}(z)\mathcal{P}$, completely describing the LANEEC process. Taking the matrix elements $\langle f'\omega'|\cdot|f\omega\rangle$ from (3.28) and substituting the projection operators $\mathcal{R}$ and $\mathcal{P}$ in the

form (3.4)—(3.5), we obtain the expression

$$\langle f'\omega'|\hat{T}(z)|f\omega\rangle = \sum_{\alpha\alpha'}\int d\varepsilon d\varepsilon' \langle f'\omega'|\hat{\Lambda}(z)|\alpha\varepsilon\rangle \pi_{\alpha\alpha'}^{-1}(\varepsilon,\varepsilon') \langle \alpha'\varepsilon'|\hat{\Lambda}(z)|f\omega\rangle \ , \qquad (3.80)$$

which with the help of (3.77) after integration becomes

$$\langle f'\omega'|\hat{T}(z)|f\omega\rangle = -i\pi \sum_{\alpha\alpha'}\langle f'\omega'|\hat{\Lambda}(z)|\alpha\omega_p\rangle \left[\sum_{n=0}^{\infty}\widetilde{X}^n\right]_{\alpha\alpha'} \langle \alpha'\omega_p|\hat{\Lambda}(z)|f\omega\rangle \ . \qquad (3.81)$$

In the following we simplify this very general result taking into account specific properties of the considered system.

The case of diagonal matrix $\widetilde{G}$

We adopt at this point the isolated resonance approximation considering the matrix $\widetilde{G}$ to be diagonal

$$\widetilde{G}_{\beta\beta'} = g_\beta \delta_{\beta\beta'} \ . \qquad (3.82)$$

This assumption reflects the fact that the bound states of the considered physical system are well separated in energy up to the case when the states are degenerate by their magnetic quantum numbers. This degeneracy does not affect the possibility to approximate $\widetilde{G}$ by the diagonal form, since all the interactions included in $\hat{V}$ are invariant with respect to rotations and preserve thus the magnetic quantum numbers of the states $|\beta\rangle$. Using the definition of $\widetilde{G}$ given by the expressions (3.45)—(3.46), we obtain

$$g_\beta = \frac{1}{z - E_\beta^0 - \langle\beta|\hat{W}|\beta\rangle} \ . \qquad (3.83)$$

The diagonal matrix element of the operator $\hat{W}$ can be rewritten with the help of its definition (3.42)—(3.43) as

$$\langle\beta|\hat{W}|\beta\rangle = V_\beta - i\pi \sum_f \left|\langle f\omega_p|\hat{V}|\beta\rangle\right|^2 \ . \qquad (3.84)$$

Here $V_\beta = \langle\beta|\hat{V}|\beta\rangle$ is the energy shift of the state $|\beta\rangle$ caused by the interaction $\hat{V}$, whereas the second term represents the radiative decay of the state $|\beta\rangle$. We introduce the corresponding width $\Gamma_\beta^{\text{rad}}$ in accordance with Fermi's golden rule as

$$\Gamma_\beta^{\text{rad}} = 2\pi \sum_f \left|\langle f\omega_p|\hat{V}|\beta\rangle\right|^2 \ . \qquad (3.85)$$

The diagonal matrix element (3.83) can be then written as

$$g_\beta = \frac{1}{z - E_\beta + \frac{i}{2}\Gamma_\beta^{\text{rad}}} \ , \qquad (3.86)$$

where $E_\beta = E_\beta^0 + V_\beta$ denotes the energy of the state $|\beta\rangle$ shifted by the interaction $\hat{V}$. The matrix elements of $\hat{\Lambda}(z)$ given by (3.57)—(3.59) take now the form

$$\langle f\omega| \hat{\Lambda}(z) |\alpha\varepsilon\rangle = \langle f\omega| \hat{V} |\alpha\varepsilon\rangle + \sum_\beta \frac{\langle f\omega| \hat{V} |\beta\rangle \langle \beta| \hat{W} |\alpha\varepsilon\rangle}{z - E_\beta + \frac{i}{2}\Gamma_\beta^{\text{rad}}} , \qquad (3.87)$$

$$\langle \alpha\varepsilon| \hat{\Lambda}(z) |f\omega\rangle = \langle \alpha\varepsilon| \hat{V} |f\omega\rangle + \sum_\beta \frac{\langle \alpha\varepsilon| \hat{W} |\beta\rangle \langle \beta| \hat{V} |f\omega\rangle}{z - E_\beta + \frac{i}{2}\Gamma_\beta^{\text{rad}}} , \qquad (3.88)$$

$$\langle \alpha\varepsilon| \hat{\Lambda}(z) |\alpha'\varepsilon'\rangle = \langle \alpha\varepsilon| \hat{U} |\alpha'\varepsilon'\rangle + \sum_\beta \frac{\langle \alpha\varepsilon| \hat{W} |\beta\rangle \langle \beta| \hat{W} |\alpha'\varepsilon'\rangle}{z - E_\beta + \frac{i}{2}\Gamma_\beta^{\text{rad}}} . \qquad (3.89)$$

The expression (3.81) for $\langle f'\omega'| \hat{T}(z) |f\omega\rangle$ contains the matrix elements $\langle \alpha'\omega_p| \hat{\Lambda}(z) |f\omega\rangle$ and $\langle f'\omega'| \hat{\Lambda}(z) |\alpha\omega_p\rangle$ given by the expressions (3.87)—(3.88). The first term in Eq. (3.87) describes direct radiative recombination. The second term depicts possible two-step processes in which electron recombination is accompanied by an excitation of the nucleus or the electronic shell (NEEC or dielectronic recombination, respectively), followed by the subsequent emission of a photon. The two terms in Eq. (3.88) represent correspondingly direct photoionization and photoabsorption with simultaneous excitation of a bound state which decays by promoting an electron to a continuum state (IC or Auger decay). Adopting these expressions specifically to the considered LANEEC process, we should keep only the second term in Eq. (3.87) and the first term in Eq. (3.88) obtaining

$$\langle f\omega| \hat{\Lambda}(z) |\alpha\varepsilon\rangle = \sum_\beta \frac{\langle f\omega| \hat{V} |\beta\rangle \langle \beta| \hat{W} |\alpha\varepsilon\rangle}{z - E_\beta + \frac{i}{2}\Gamma_\beta^{\text{rad}}} , \qquad (3.90)$$

$$\langle \alpha\varepsilon| \hat{\Lambda}(z) |f\omega\rangle = \langle \alpha\varepsilon| \hat{V} |f\omega\rangle . \qquad (3.91)$$

We note that the expression (3.90) describes both NEEC and dielectronic recombination and will be further specified later in this Chapter. Substituting these expressions into (3.81), we find

$$\langle f'\omega'| \hat{T}(z) |f\omega\rangle = -i\pi \sum_{\beta\alpha\alpha'} \frac{\langle f'\omega'| \hat{V} |\beta\rangle}{z - E_\beta + \frac{i}{2}\Gamma_\beta^{\text{rad}}}$$
$$\times \langle \beta| \hat{W} |\alpha\omega_p\rangle \left[\sum_{n=0}^\infty \widetilde{X}^n \right]_{\alpha\alpha'} \langle \alpha'\omega_p| \hat{V} |f\omega\rangle . \qquad (3.92)$$

The matrix $\widetilde{X}$ defined by (3.74) can be written using (3.89) as

$$\widetilde{X}_{\alpha\alpha'} = -i\pi \langle \alpha\omega_p| \hat{U} |\alpha'\omega_p\rangle - i\pi \sum_\beta \frac{\langle \alpha\omega_p| \hat{W} |\beta\rangle \langle \beta| \hat{W} |\alpha'\omega_p\rangle}{z - E_\beta + \frac{i}{2}\Gamma_\beta^{\text{rad}}} . \qquad (3.93)$$

We neglect the contribution of the term with $\langle \alpha\omega_p| \hat{U} |\alpha'\omega_p\rangle$ describing the process of radiative recombination of the intermediate state $|\alpha\omega_p\rangle$, which we do not consider in this work. We obtain thus

$$\widetilde{X}_{\alpha\alpha'} = -i\pi \sum_\beta \frac{\langle \alpha\omega_p| \hat{W} |\beta\rangle \langle \beta| \hat{W} |\alpha'\omega_p\rangle}{z - E_\beta + \frac{i}{2}\Gamma_\beta^{\text{rad}}} . \qquad (3.94)$$

We now proceed by summing the series in (3.92). Let us first consider the sum

$$\sum_\alpha \langle\beta|\,\hat{W}\,|\alpha\omega_p\rangle\,\widetilde{X}_{\alpha\alpha'} = \sum_{\beta'} \frac{\langle\beta|\,\hat{Y}\,|\beta'\rangle\,\langle\beta'|\,\hat{W}\,|\alpha'\omega_p\rangle}{z - E_{\beta'} + \frac{i}{2}\Gamma^{\mathrm{rad}}_{\beta'}}\ , \tag{3.95}$$

where the operator $\hat{Y}$ is defined as

$$\hat{Y} = -i\pi \sum_\alpha \hat{W}\,|\alpha\omega_p\rangle\,\langle\alpha\omega_p|\,\hat{W}\ . \tag{3.96}$$

Analogously as we assumed that the matrix $\widetilde{G}_{\beta\beta'}$ and thus the matrix $\langle\beta|\,\hat{W}\,|\beta'\rangle$ are diagonal, we consider the matrix $\langle\beta|\,\hat{Y}\,|\beta'\rangle$ to be diagonal

$$\langle\beta|\,\hat{Y}\,|\beta'\rangle = \delta_{\beta\beta'}\,\langle\beta|\,\hat{Y}\,|\beta\rangle = -\frac{i}{2}\Gamma^{\mathrm{el}}_\beta\ , \tag{3.97}$$

where the decay rate via the electronic shell $\Gamma^{\mathrm{el}}_\beta$ for the state $|\beta\rangle$ is introduced in accordance with Fermi's golden rule as

$$\Gamma^{\mathrm{el}}_\beta = 2\pi \sum_\alpha \left|\langle\alpha\omega_p|\,\hat{W}\,|\beta\rangle\right|^2\ . \tag{3.98}$$

The rate $\Gamma^{\mathrm{el}}_\beta$ consists of the IC and the Auger decay contributions. The sum (3.95) takes then the form

$$\sum_\alpha \langle\beta|\,\hat{W}\,|\alpha\omega_p\rangle\,\widetilde{X}_{\alpha\alpha'} = \frac{-\frac{i}{2}\Gamma^{\mathrm{el}}_\beta}{z - E_\beta + \frac{i}{2}\Gamma^{\mathrm{rad}}_\beta}\,\langle\beta|\,\hat{W}\,|\alpha'\omega_p\rangle\ . \tag{3.99}$$

Using this result, we obtain in the same manner

$$\begin{aligned}\sum_\alpha \langle\beta|\,\hat{W}\,|\alpha\omega_p\rangle\left[\widetilde{X}^2\right]_{\alpha\alpha'} &= \sum_{\alpha\alpha''} \langle\beta|\,\hat{W}\,|\alpha\omega_p\rangle\,\widetilde{X}_{\alpha\alpha''}\widetilde{X}_{\alpha''\alpha'} \\ &= \left(\frac{-\frac{i}{2}\Gamma^{\mathrm{el}}_\beta}{z - E_\beta + \frac{i}{2}\Gamma^{\mathrm{rad}}_\beta}\right)^2 \langle\beta|\,\hat{W}\,|\alpha'\omega_p\rangle\end{aligned} \tag{3.100}$$

and applying this procedure iteratively n times we find

$$\sum_\alpha \langle\beta|\,\hat{W}\,|\alpha\omega_p\rangle\left[\widetilde{X}^n\right]_{\alpha\alpha'} = \left(\frac{-\frac{i}{2}\Gamma^{\mathrm{el}}_\beta}{z - E_\beta + \frac{i}{2}\Gamma^{\mathrm{rad}}_\beta}\right)^n \langle\beta|\,\hat{W}\,|\alpha'\omega_p\rangle\ . \tag{3.101}$$

The series in (3.92) can be then written as

$$\sum_\alpha \langle\beta|\,\hat{W}\,|\alpha\omega_p\rangle\left[\sum_{n=0}^\infty \widetilde{X}^n\right]_{\alpha\alpha'} = \left(\sum_{n=0}^\infty q^n\right)\langle\beta|\,\hat{W}\,|\alpha'\omega_p\rangle\ , \tag{3.102}$$

and reduces thus to the geometric series

$$\sigma(q) = \sum_{n=0}^\infty q^n \tag{3.103}$$

with the complex variable

$$q = \frac{-\frac{i}{2}\Gamma_\beta^{\text{el}}}{z - E_\beta + \frac{i}{2}\Gamma_\beta^{\text{rad}}} \ . \tag{3.104}$$

We note that the standard convergence condition $|q| < 1$ is here generally speaking not satisfied. In spite of this fact, it is possible to evaluate $\sigma(q)$ using the approach of the Borel summation [90]. This method employs the so-called Borel transform, which maps the series

$$S(x) = \sum_n a_n x^n \tag{3.105}$$

with a complex variable x and complex coefficients a_n to the series

$$\mathcal{B}S(x) = \sum_n \frac{a_n}{n!} x^n \ . \tag{3.106}$$

Then $S(x)$ is obtained as

$$S(x) = \int_0^\infty e^{-y}\mathcal{B}S(xy)dy \ . \tag{3.107}$$

In the Borel approach the sum $S(x)$ converges in the region containing the origin O and formed by the intersection of perpendiculars to the lines OP_i at the point P_i for all i, where P_i is the i-th pole of $S(x)$. In our case the Borel transform is

$$\mathcal{B}\sigma(q) = \sum_n \frac{1}{n!}q^n = e^q \tag{3.108}$$

and the sum

$$\sigma(q) = \int_0^\infty e^{-y}e^{yq}dy = \frac{1}{1-q} \ . \tag{3.109}$$

The convergence condition is $\text{Re}(q) < 1$ and for the considered problem is always satisfied, since at the limit $z = \lim_{\delta \to +0}(\omega_p + i\delta)$

$$\text{Re}(q) = \sum_\beta \frac{-\frac{1}{4}\Gamma_\beta^{\text{el}}\Gamma_\beta^{\text{rad}}}{(\omega_p - E_\beta)^2 + (\Gamma_\beta^{\text{rad}}/2)^2} < 0 \ . \tag{3.110}$$

The series in (3.92) takes then the value

$$\sum_\alpha \langle\beta|\,\hat{W}\,|\alpha\omega_p\rangle \left[\sum_{n=0}^\infty \widetilde{X}^n\right]_{\alpha\alpha'} = \frac{z - E_\beta + \frac{i}{2}\Gamma_\beta^{\text{rad}}}{z - E_\beta + \frac{i}{2}\Gamma_\beta} \langle\beta|\,\hat{W}\,|\alpha'\omega_p\rangle \ , \tag{3.111}$$

where we introduce the total decay rate of the state $|\beta\rangle$ as $\Gamma_\beta = \Gamma_\beta^{\text{rad}} + \Gamma_\beta^{\text{el}}$. Taking into account the obtained result, the expression (3.92) for the matrix elements of the operator $\hat{T}(z)$ becomes

$$\langle f'\omega'|\,\hat{T}(z)\,|f\omega\rangle = -i\pi \sum_{\beta\alpha} \frac{\langle f'\omega'|\,\hat{V}\,|\beta\rangle\,\langle\beta|\,\hat{V} + \hat{U}\,|\alpha\omega_p\rangle\,\langle\alpha\omega_p|\,\hat{V}\,|f\omega\rangle}{z - E_\beta + \frac{i}{2}\Gamma_\beta} \ , \tag{3.112}$$

where we have replaced $\hat{W}$ by $\hat{V} + \hat{U}$ in accordance with its definition (3.42)—(3.43).

LANEEC rate

The perturbation $\hat{V}$ consists of the interactions mixing the states from $\mathcal{R}$, $\mathcal{P}$, $\mathcal{Q}$ and can be represented as the sum

$$\hat{V} = \hat{H}_{en} + \hat{H}_{nr} + \hat{H}_{er} \,, \tag{3.113}$$

where $\hat{H}_{en}$ stands for the Coulomb coupling of the nucleus to the electronic shell, $\hat{H}_{nr}$ and $\hat{H}_{er}$ describe the interaction of the nucleus and the electrons respectively with the radiation field. When substituting this representation of $\hat{V}$ into (3.112), only those terms should be kept in the matrix elements which reflect the considered LANEEC process. Namely,

- the absorption of a photon by the electronic shell with a transfer of an electron to a continuum state is described by the matrix element $\langle \alpha\omega_p | \hat{V} | f\omega \rangle \rightarrow \langle \alpha\omega_p | \hat{H}_{er} | f\omega \rangle$;

- the capture of the continuum electron with the simultaneous excitation of the nucleus is represented by $\langle \beta | \hat{V} + \hat{U} | \alpha\omega_p \rangle \rightarrow \langle \beta | \hat{H}_{en} + \hat{U} | \alpha\omega_p \rangle$;

- the radiative decay of the excited nuclear state is described by the matrix element $\langle f'\omega' | \hat{V} | \beta \rangle \rightarrow \langle f'\omega' | \hat{H}_{nr} | \beta \rangle$.

We thus obtain

$$\langle f'\omega' | \hat{T}(z) | f\omega \rangle = -i\pi \sum_{\beta\alpha} \frac{\langle f'\omega' | \hat{H}_{nr} | \beta \rangle \langle \beta | \hat{H}_{en} + \hat{U} | \alpha\omega_p \rangle \langle \alpha\omega_p | \hat{H}_{er} | f\omega \rangle}{z - E_\beta + \frac{i}{2}\Gamma_\beta} \,. \tag{3.114}$$

The operator $\hat{U}$ defined by (3.42) can be replaced in the matrix element $\langle \beta | \cdot | \alpha\omega_p \rangle$ in (3.114) by the operator

$$\hat{H}_{\text{magn}} = -i\pi \hat{H}_{nr} \sum_{f} | f\omega_p \rangle \langle f\omega_p | \hat{H}_{er} \,, \tag{3.115}$$

describing the process of interaction of the continuum electron with the nucleus via an intermediate virtual photon. We refer to this contribution as to magnetic interaction. The sum $\hat{H}_{en} + \hat{H}_{\text{magn}} = \hat{H}_{\text{int}}$ is the total coupling of the nucleus to the electronic shell used throughout this work and described in detail in Appendix A. We obtain finally

$$\langle f'\omega' | \hat{T}(z) | f\omega \rangle = -i\pi \sum_{\beta\alpha} \frac{\langle f'\omega' | \hat{H}_{nr} | \beta \rangle \langle \beta | \hat{H}_{\text{int}} | \alpha\omega_p \rangle \langle \alpha\omega_p | \hat{H}_{er} | f\omega \rangle}{z - E_\beta + \frac{i}{2}\Gamma_\beta} \,. \tag{3.116}$$

The considered process is represented by the Feynman diagram in Fig 3.3. The nucleus depicted by the double-line goes from the ground state (g) through the excited state (m) back to the ground state (g). The electronic shell shown by the solid line evolves from its initial state (i) to the intermediate state (n), which includes a continuum electron, and then to the final state (f). The quantity required to calculate the rate of the process according to Fermi's golden rule is the modulus squared of the matrix element

$$\left| \langle f'\omega' | \hat{T}(z) | f\omega \rangle \right|^2 = \pi^2 \left| \sum_{\beta\alpha} \frac{\langle f'\omega' | \hat{H}_{nr} | \beta \rangle \langle \beta | \hat{H}_{\text{int}} | \alpha\omega_p \rangle \langle \alpha\omega_p | \hat{H}_{er} | f\omega \rangle}{z - E_\beta + \frac{i}{2}\Gamma_\beta} \right|^2 \,. \tag{3.117}$$

We consider at this point the part corresponding to the nuclear excitation shown in Fig. 3.3 to the left of the dashed line. It is possible to split the entire process into
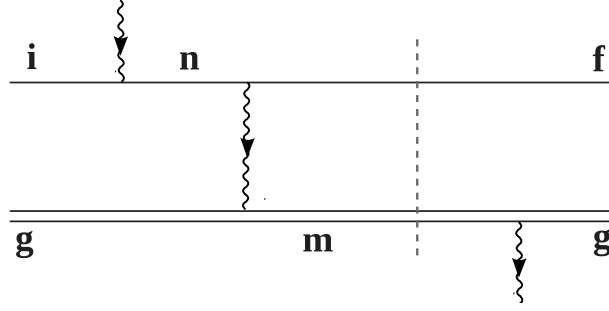
65

Figure 3.3: The Feynman diagram of the LANEEC process (to the left of the dashed line) accomplished with the subsequent decay of the nuclear excited state (to the right of the dashed line). The solid line corresponds to the electronic states, the double-line represents the nuclear state and the wiggly lines depict the photons.

the two parts only if the interference terms in (3.117) corresponding to different $|\beta\rangle$ are omitted giving

$$\left| \langle f'\omega' | \hat{T}(z) | f\omega \rangle \right|^2 = \sum_\beta \frac{\left| \langle f'\omega' | \hat{H}_{nr} | \beta \rangle \right|^2 \left| \sum_\alpha (-i\pi) \langle \beta | \hat{H}_{\text{int}} | \alpha\omega_p \rangle \langle \alpha\omega_p | \hat{H}_{er} | f\omega \rangle \right|^2}{\left| z - E_\beta + \frac{i}{2}\Gamma_\beta \right|^2} .$$

(3.118)

Under this condition the description of the whole process splits into the process of LANEEC and subsequent radiative decay for each $|\beta\rangle$. It can be seen from (3.118) that the former part is represented by the amplitude

$$\langle \beta | \hat{T}_{\text{LANEEC}} | f\omega \rangle = -i\pi \sum_\alpha \langle \beta | \hat{H}_{\text{int}} | \alpha\omega_p \rangle \langle \alpha\omega_p | \hat{H}_{er} | f\omega \rangle .$$

(3.119)

We express the LANEEC rate via the rate of the inverse spontaneous process consisting in decay of the nuclear excited state via IC with subsequent radiative recombination of the continuum electron. The inverse process is represented by the transposed matrix element

$$\langle f\omega | \hat{T}_{\text{LANEEC}} | \beta \rangle = -i\pi \sum_\alpha \langle f\omega | \hat{H}_{er} | \alpha\omega_p \rangle \langle \alpha\omega_p | \hat{H}_{\text{int}} | \beta \rangle .$$

(3.120)

We consider the external photon emitted at the radiative recombination step of the inverse process to be an electric dipole photon, so that the process as a whole can be effectively considered as an electric dipole decay. Carrying out analogous analysis as for the EB decay in Chapter 2, we obtain the inverse process rate $\widetilde{\Gamma}_{\text{inv}}$

$$\widetilde{\Gamma}_{\text{inv}} = \frac{16\pi\alpha^3 E_{\text{phot}}^3}{3(2J_f + 1)} \sum_{\lambda L} \frac{B_\downarrow^{\lambda L} \widetilde{G}^{\lambda L}}{(2L + 1)^2} .$$

(3.121)

analogous to the equation (2.19). Here J_f is the total angular momentum of the initial electronic state in the inverse process, which is the final state in the LANEEC process. $\widetilde{G}^{\lambda L}$ is given by the expression

$$\widetilde{G}^{\lambda L} = \sum_{j_n} \frac{\pi^2}{2j_n + 1} \left| \sum_{l_n} \langle \beta_i J_i \| \hat{D} \| l_n j_n \varepsilon \rangle \langle l_n j_n \varepsilon \| \hat{\mathcal{T}}_{\lambda L} \| \beta_f J_f \rangle \right|^2 ,$$

(3.122)

where the indices i and f correspond respectively to the initial and final states in the LANEEC process, j_n and l_n are the total angular momentum and the orbital angular momentum characterizing the continuum electronic state, ε is the energy of the continuum electron, which with the help of the energy conservation law can be expressed via the energy of the nuclear excited state E_m and the ionization energy E_p for the bound electron as $\varepsilon = E_m - E_i - E_p$. The LANEEC rate can be found via the rate of the spontaneous decay process analogously to the EB excitation considered in Section 2.4 [74]

$$\widetilde{\Gamma}_{\text{excit}} = \widetilde{\Gamma}_{\text{EB}} \frac{4\pi^3 c^2 \hbar^2}{E_{\text{phot}}^3} P_\omega \delta \; . \tag{3.123}$$

The photon energy in (3.123) should be sufficient for the process, that is if the initial energy of the electronic shell is E_i, the value of E_{phot} should be $E_{\text{phot}} = E_m - E_i$.

3.2 LANEEC excitation of the nuclear state at 29.18 keV in ^{229}Th

In this Section we use the obtained theoretical results to investigate an excitation scheme for the nuclear state at 29.19 keV in ^{229}Th at the SACLA facility. The direct excitation of the 29.19-keV levels lies outside the capabilities of SACLA, which is able to provide X-ray photons in the energy range 4–20 keV. We consider an excitation with two beams at energies approx. 20.68 keV and 8.51 keV, which are available or should be available in the nearest future at SACLA. The scheme involves the closed shells of ^{229}Th listed in Table 3.1 with their energies obtained by solving numerically the DHF equations. The first beam ionizes the $2s$ electronic orbital in ^{229}Th creating $2s$-holes in the sample, whereas the second beam induces the LANEEC process involving an electron from the $6p$-shell. A $6p$-electron is promoted to a continuum state at the energy 8.51 keV, which decays to the hole in the $2s$-orbital transferring its energy $8.51 + 20.68 = 29.19$ keV to the nucleus. The 29.19-keV level decays then predominantly to the ^{229}Th isomeric state. The $6p_{\frac{1}{2}}$ and $6p_{\frac{3}{2}}$ orbitals are not distinguished in this scheme due to the spectral width of the SACLA beam of a few tens eV exceeding the energy interval between the two orbitals.

Orbital	Energy (keV)	Orbital	Energy (keV)	Orbital	Energy (keV)
$1s$	-110.466	$3d_{\frac{5}{2}}$	-3.417	$5s$	-0.347
$2s$	-20.674	$4s$	-1.399	$5p_{\frac{1}{2}}$	-0.284
$2p_{\frac{1}{2}}$	-19.894	$4p_{\frac{1}{2}}$	-1.240	$5p_{\frac{3}{2}}$	-0.237
$2p_{\frac{3}{2}}$	-16.457	$4p_{\frac{3}{2}}$	-1.032	$5d_{\frac{3}{2}}$	-0.141
$3s$	-5.288	$4d_{\frac{3}{2}}$	-0.776	$5d_{\frac{5}{2}}$	-0.134
$3p_{\frac{1}{2}}$	-4.935	$4d_{\frac{5}{2}}$	-0.738	$6s$	-0.088
$3p_{\frac{3}{2}}$	-4.139	$4f_{\frac{5}{2}}$	-0.401	$6p_{\frac{1}{2}}$	-0.067
$3d_{\frac{3}{2}}$	-3.579	$4f_{\frac{7}{2}}$	-0.391	$6p_{\frac{3}{2}}$	-0.058

Table 3.1: Closed shells of ^{229}Th and their energies obtained by solving the DHF equations.

As an example of experimental implementation, we consider an isotopically purified ^{229}Th sample of the thickness 1 μm irradiated by the two SACLA beams. The assumed parameters of the beams are shown in Table 3.2 and are taken from Ref. [87]. The

Repetition rate	$\nu = 30$ Hz
Pulse duration	$\tau_p = 10$ fs
Relative spectral width	$\frac{\Delta E_{\text{phot}}}{E_{\text{phot}}} = 0.5\%$
Intensity	$I = 10^{18} \, \frac{\text{W}}{\text{cm}^2}$
Focal diameter	$d = 1 \, \mu\text{m}$

Table 3.2: Parameters of the SACLA beams assumed based on Ref. [87].

electrons extracted from the $2s$-shell move in the sample to neighboring atoms and can recombine with any hole in the surrounding. The electrons from the upper electronic shells in ^{229}Th also recombine with the $2s$-hole within a short time leading to the energy width of 14.3 eV [91], corresponding to the lifetime $\tau_h \approx 50$ as much sorter than the SACLA pulse duration. Under these circumstances, it is reasonable to assume for the estimate that the number of the holes is constant within the pulse time. The condition defining the total number of the holes N^h at equilibrium is then

$$0 = \frac{dN^h}{dt} = \sigma^h F N_{\text{Th}} - \frac{1}{\tau^h} N^h \, , \tag{3.124}$$

where F is the photon flux obtained from the intensity I as $F = I/E_{\text{phot}}$, N_{Th} is the number of irradiated ^{229}Th atoms in the sample and σ^h is the hole creation cross section. We find from this condition

$$N^h = \sigma^h \tau^h F N_{\text{Th}} \, . \tag{3.125}$$

In our case the number of irradiated ^{229}Th atoms is $N_{\text{Th}} \approx 2.4 \cdot 10^{10}$. The value for the cross section $\sigma^h \approx 285$ b was obtained experimentally in Ref. [92]. Accordingly to (3.125), this leads to the steady number of holes in the sample $N^h \approx 1.0 \cdot 10^5$. The LANEEC rate per ^{229}Th atom with a $2s$-hole calculated with the expressions (3.121)—(3.123) is $\widetilde{\Gamma}_{\text{excit}} \approx 4.3 \cdot 10^{-11} \, \text{s}^{-1}$. In this calculation, the relativistic wave functions for the involved bound electronic states are evaluated with the GRASP2K package [47]. The continuum wave functions are obtained using the program *xphoto* from the RATIP package [48]. We use in our calculations the rate of the radiative decay of the nuclear level at 29.19 keV to the ground state $2.6 \cdot 10^6 \, \text{s}^{-1}$. It corresponds to the value 1.7 neV obtained using the half-life, IC coefficient and branching ratios of this level [82]. The total excitation rate is equal then to $\widetilde{\Gamma}_{\text{excit}} N^h \approx 4.5 \cdot 10^{-6} \, \text{s}^{-1}$ or approximately 0.4 excitations per day. Due to this low rate, the scheme is not practical at the moment. Nevertheless, the comparison with the direct two-photon excitation of the nucleus in next Section shows that the electronic shell causes a large enhancement of the excitation process, rendering this scheme interesting for X-ray quantum optics with nuclei.

3.3 Direct two-photon excitation of the nuclear state at 29.18 keV in ^{229}Th

We obtain in this Section the rate of the direct two-photon excitation of the nuclear level at $E_0 = 29.19$ keV in the ^{229}Th nucleus. To the best of our knowledge, reliable information on the multipole mixing of this transition is not available in literature. We consider for the estimate the $M1$ type so that the two photon absorption occurs via the $M1 - M1$ channel. The process depends smoothly on the energies of the exciting photons. We assume here for simplicity that the two photons have equal energy $E_1 =$

$E_2 = E_0/2 \approx 14.6$ keV and the two beams are polarized such that their magnetic fields are directed along the z-axis. These assumptions do not change the results qualitatively allowing comparison of the LANEEC and the direct two-photon excitation. We consider the excitation rate $\Gamma_{2\text{phot}}(M_g \to M_e)$ from the nuclear state $|\alpha_g I_g M_g\rangle$ to the state $|\alpha_e I_e M_e\rangle$, where I and M denote the total spin and the magnetic quantum number respectively and α incorporates the other quantum numbers relevant for description of the nuclear state. The indices g and e correspond to the ground state and the excited state at $E_0 = 29.19$ keV, respectively. It can be shown by applying the time-dependent perturbation theory that $\Gamma_{2\text{phot}}(M_g \to M_e)$ is given by the expression [93]

$$\Gamma_{2\text{phot}}(M_g \to M_e) = \frac{1}{2\Gamma_0} \left| \mathcal{M}^{(2)}(M_g \to M_e) \right|^2 , \qquad (3.126)$$

where Γ_0 denotes the total width of the transition $g \to e$ including the IC channel, and $\mathcal{M}^{(2)}(M_g \to M_e)$ is

$$
\begin{aligned}
\mathcal{M}^{(2)}(M_g \to M_e) &= \sum_n \left[\frac{\langle \alpha_e I_e M_e | \hat{H}_{nr} | \alpha_n I_n M_n \rangle \langle \alpha_n I_n M_n | \hat{H}_{nr} | \alpha_g I_g M_g \rangle}{E_n - E_2} \right. \\
&\quad + \left. \frac{\langle \alpha_e I_e M_e | \hat{H}_{nr} | \alpha_n I_n M_n \rangle \langle \alpha_n I_n M_n | \hat{H}_{nr} | \alpha_g I_g M_g \rangle}{E_n - E_1} \right] \\
&= 2 \sum_n \frac{\langle \alpha_e I_e M_e | \hat{H}_{nr} | \alpha_n I_n M_n \rangle \langle \alpha_n I_n M_n | \hat{H}_{nr} | \alpha_g I_g M_g \rangle}{E_n - \frac{E_0}{2}} .
\end{aligned} \qquad (3.127)
$$

The summation here is carried out over all intermediate states $|\alpha_n I_n M_n\rangle$, the energy of which is denoted by E_n. The expression (3.127) takes into account that we consider a non-resonant case in which the energy of each photon is far from the energy of the driven transition. This results in the absence of the state widths in the denominators. The interaction of the nucleus with the radiation field reduces now to the interaction of the magnetic moment with the magnetic field of the amplitude $\mathcal{B}$, so that the operator $\hat{H}_{nr}$ is represented as $\hat{H}_{nr} = \hat{\mu}_z \mathcal{B}$. We note that in this Section $\hat{\mu}_z$ is defined in the conventional way [94], such that the nuclear transition probability from the excited level to the ground state can be expressed via its reduced matrix element as [94]

$$B_\downarrow^{M1} = \frac{|\langle \alpha_g I_g \| \hat{\mu} \| \alpha_e I_e \rangle|^2}{2I_e + 1} . \qquad (3.128)$$

The operator $\hat{\mu}_z$ corresponds to the zeroth spherical component and preserves thus the magnetic quantum numbers in the matrix elements in (3.127). This allows to rewrite (3.127) as

$$\mathcal{M}^{(2)}(M_g \to M_e) = 2\delta_{M_e M_g} \sum_n \frac{\langle \alpha_e I_e M_g | \hat{\mu}_z \mathcal{B} | \alpha_n I_n M_g \rangle \langle \alpha_n I_n M_g | \hat{\mu}_z \mathcal{B} | \alpha_g I_g M_g \rangle}{E_n - \frac{E_0}{2}} . \qquad (3.129)$$

We suppose that the two levels are isolated such that the state $|\alpha_n I_n M_n\rangle$ belongs either to the ground level or to the excited level multiplet. We obtain therefore

$$\mathcal{M}^{(2)}(M_g \to M_e) = \frac{4\mathcal{B}^2}{E_0} \delta_{M_e M_g} \langle \alpha_e I_e M_g | \hat{\mu}_z | \alpha_g I_g M_g \rangle \qquad (3.130)$$
$$\times \Big(\langle \alpha_e I_e M_g | \hat{\mu}_z | \alpha_e I_e M_g \rangle - \langle \alpha_g I_g M_g | \hat{\mu}_z | \alpha_g I_g M_g \rangle \Big) .$$

69

The matrix elements in this expression can be rewritten with the help of the Wigner-Eckart theorem [39] as

$$\langle\alpha_e I_e M_g|\,\hat{\mu}_z\,|\alpha_g I_g M_g\rangle = (-1)^{1-I_g+I_e}\frac{\langle\alpha_e I_e\|\,\hat{\mu}\,\|\alpha_g I_g\rangle}{\sqrt{2I_e+1}}\,C_{0M_g\,M_g}^{1I_g\ I_e}\,, \qquad (3.131)$$

$$\langle\alpha_e I_e M_g|\,\hat{\mu}_z\,|\alpha_e I_e M_g\rangle = \sqrt{\frac{3}{4\pi}}\frac{C_{0M_g M_g}^{1I_e\ I_e}}{C_{0I_e I_e}^{1I_e I_e}}\mu_e = \sqrt{\frac{3}{4\pi}}\frac{M_g}{I_e}\mu_e\,, \qquad (3.132)$$

$$\langle\alpha_g I_g M_g|\,\hat{\mu}_z\,|\alpha_g I_g M_g\rangle = \sqrt{\frac{3}{4\pi}}\frac{C_{0M_g M_g}^{1I_g\ I_g}}{C_{0I_g I_g}^{1I_g I_g}}\mu_g = \sqrt{\frac{3}{4\pi}}\frac{M_g}{I_g}\mu_g\,, \qquad (3.133)$$

where we use the properties of the Clebsch-Gordan coefficients [69] and the conventional definition of the magnetic moment [94]

$$\mu_{e/g} = \sqrt{\frac{4\pi}{3}}\left\langle\alpha_{e/g}I_{e/g}I_{e/g}\Big|\hat{\mu}_z\Big|\alpha_{e/g}I_{e/g}I_{e/g}\right\rangle \qquad (3.134)$$

for the ground and the excited nuclear states. The expression (3.130) takes now the form

$$\Gamma_{2\text{phot}}(M_g\to M_e) = \delta_{M_e M_g}\frac{6\mathcal{B}^4}{\pi E_0^2\Gamma_0}B_\downarrow^{M1}\left(\frac{\mu_e}{I_e}-\frac{\mu_g}{I_g}\right)^2\left[C_{0M_g M_g}^{1I_g\ I_e}\right]^2 M_g^2\,. \qquad (3.135)$$

Introducing the radiative decay rate as [30]

$$\Gamma_{\text{rad}}^{M1} = \frac{16\pi}{9}\alpha^3 E_0^3 B_\downarrow^{M1}\,, \qquad (3.136)$$

we rewrite (3.135) as

$$\Gamma_{2\text{phot}}(M_g\to M_e) = \delta_{M_e M_g}\frac{27\mathcal{B}^4\Gamma_{\text{rad}}^{M1}}{8\pi\alpha^3 E_0^5\Gamma_0}\left(\frac{\mu_e}{I_e}-\frac{\mu_g}{I_g}\right)^2\left[C_{0M_g M_g}^{1I_g\ I_e}\right]^2 M_g^2\,. \qquad (3.137)$$

In order to obtain the excitation rate, we

- sum over the final states in the excited nuclear level and average over the initial states belonging to the ground multiplet;

- take into account that for the SACLA beams of the bandwidth ΔE_{phot} the fraction of the photon pairs exciting the nucleus is $\Gamma_0/\Delta E_{\text{phot}}$;

- take into account that the SACLA-radiation is pulsed and the actual excitation time is $\tau_p\nu$.

Analytically this yields the expression

$$\Gamma_{2\text{phot}} = \frac{1}{2I_g+1}\sum_{M_g M_e}\Gamma_{2\text{phot}}(M_g\to M_e)\cdot\left(\frac{\Gamma_0}{\Delta E_{\text{phot}}}\right)\cdot(\tau_p\nu)\,. \qquad (3.138)$$

We obtain then

$$\Gamma_{2\text{phot}} = \frac{27\mathcal{B}^4\tau_p\nu}{8\pi\alpha^3 E_0^5\Delta E_{\text{phot}}}\left(\frac{\mu_e}{I_e}-\frac{\mu_g}{I_g}\right)^2\sigma(I_g,I_e)\Gamma_{\text{rad}}^{M1}\,, \qquad (3.139)$$

where the quantity

$$\sigma(I_g, I_e) = \frac{1}{2I_g + 1} \sum_{M_g} \left[C^{1\,I_g\ \ I_e}_{0\,M_g\,M_g} \right]^2 M_g^2 \tag{3.140}$$

is evaluated numerically. In the case of our interest we have

$$\sigma\left(\frac{5}{2}, \frac{5}{2}\right) = \frac{101}{60} \ . \tag{3.141}$$

The magnetic field $\mathcal{B}$ in (3.139) is measured in atomic units $\mathcal{B}_{\text{at}}$, which in SI can be expressed as

$$\mathcal{B}_{\text{at}} = \frac{\hbar}{ea_0^2} \approx 2.35 \cdot 10^5 \ \text{T} \ , \tag{3.142}$$

where e is the elementary charge and a_0 is the Bohr radius. The magnetic field in the exciting beams can be expressed in SI through the intensity with the help of the expression

$$I = \frac{c}{2\mu_0} \mathcal{B}_{\text{SI}}^2 \ , \tag{3.143}$$

where μ_0 is the vacuum permeability, and then converted to the atomic units as $\mathcal{B} = \mathcal{B}_{\text{SI}}/\mathcal{B}_{\text{at}}$.

We consider at this point again an isotopically purified ^{229}Th sample of the thickness 1 μm irradiated by two SACLA photon beams with the properties listed in the Table 3.2. In this calculation the beams have equal energies $E_1 = E_2 = E_0/2 \approx 14.6$ keV. The value for the magnetic moment $\mu_g = 0.464\mu_N$, where μ_N is the nuclear magneton, can be found in the database [95], whereas to the best of our knowledge no information on μ_e is available in literature. We use a preliminary theoretical value $\mu_e = 0.323\mu_N$ [96] obtained with the help of the numerical model developed in Ref. [44] that considers the motion of the single (odd) nucleon coupled to the collective quadrupole-octupole vibration-rotation motion of the nucleus and includes the Coriolis interaction. The calculated two-photon excitation rate per ^{229}Th atom is $\Gamma_{2\text{phot}} \approx 1.6 \cdot 10^{-29}$ s^{-1} leading to the total two-photon excitation rate $\Gamma_{2\text{phot}} N_{\text{Th}} \approx 4.0 \cdot 10^{-19}$ s^{-1}. Comparison of the LANEEC involving the electronic shell with the direct two-photon excitation of the state at 29.18 keV in ^{229}Th shows that the atomic electrons cause a large enhancement of 13 orders of magnitude.

Chapter 4

Numerical methods

In this Chapter we discuss in detail the numerical approaches used in the present work for the obtained results, such as the rates of the considered processes, the electronic energy levels or the lifetimes of particular electronic states. In a number of cases the open source packages GRASP2K [47] and RATIP [48] are used for obtaining all necessary information on the atomic shell structure. In some cases however these packages could not be applied due to the reasons discussed below. In such situations, we develop our own codes using the programming language FORTRAN. We show the theoretical background for the applied methods and carry out necessary consistency checks.

4.1 Calculations with GRASP2K and RATIP packages

The GRASP2K package [47] developed by the Computational Atomic Structure Group [97], consists of a number of programs for calculation of properties of many-electron atomic systems, such as the energy levels, the relativistic wave functions, the hyperfine structure constants, the isotopic shifts and the rates of the transitions between the atomic states. Being based on the multiconfiguration DHF approach, this package provides an opportunity to include higher-order valence, core and core-valence correlations evaluated within the many-body perturbation theory. In this section we describe in a step-by-step manner the application of GRASP2K to calculations carried out in the present work. Depending on the purpose of the calculation, the RATIP package [48] can be used based on the output from GRASP2K.

The calculation starts from the program *rnucleus*, which takes as an input the information related to the atomic nucleus: the charge number, the mass number, the mass of the neutral atom, the nuclear spin, the nuclear magnetic dipole and electric quadrupole moments. Based on the charge and the mass numbers, the code evaluates parameters accounting for the nuclear size. The mass of the neutral atom is used to take into account the nuclear motion. This program allows also change of the grid parameters used throughout the calculation.

After the file with the nuclear data is generated, we run the programs *rcsfexcitation* and *rcsfgenerate*, which read the information about the occupied electronic orbitals, the electronic configurations of the atom, the total angular momentum and the excited electronic orbitals for taking into account the higher-order correlations. Based on these data, the programs generate a list of all possible angular couplings in the electronic shell for the considered electronic configurations of the atom and all involved excited configurations. Each item in the list corresponds to a function referred to as configuration state function (CSF). The atomic state in a particular electronic configuration is a linear combination of the CSFs.

The DHF method is based on the assumption that all electrons in the atom move in a spherical self-consistent field. This leads to separation of the angular and the radial variables. The angular part consists of a set of expressions, which have the form of

matrix elements of irreducible tensor operators. They are evaluated at this stage with the help of the program *rangular*.

The next step is the program *rwfnestimate* carrying out the first estimation of the energy levels and the radial parts of the relativistic wave functions. The used method is according to the user's choice either the Thomas-Fermi method or the hydrogenic approximation with the screened nucleus. In most cases both approaches provide a sufficient estimation for further calculation.

At this point we solve the DHF equations using the program *rmcdhf* and obtain the radial parts of the CSFs. The mixing coefficients for these CSFs and corresponding energy eigenvalues are also evaluated at this stage. This defines completely the atomic wave function for every considered electronic configuration. The code solves the DHF equations using the method of successive approximations, which should converge in a few tens iterations. If convergence is not achieved, the program should be run with a smaller number of varied wave functions and few so-called spectroscopic wave-functions. The accuracy of the spectroscopic wave-functions is additionally improved by the code. The output is then used for a next run with less number of limitations approaching step by step the initial case of our interest. The obtained results should be saved now by calling *rsave* with an argument labeling the considered case. If we are interested in particular bound radial wave functions, they can be extracted at this point with the help of the program *rwfnplot*.

Next, we use the program *rci*, which carries out relativistic configuration-interaction calculations based on the files created by *rsave*. The output consists of the mixing coefficients for the electronic configurations of the atom defining completely the atomic state. The program takes into account the Breit interaction of electrons via a transverse photon, the vacuum polarization, the self-energy correction and the isotopic mass shifts. If it is intended to obtain continuum radial wave functions with the RATIP package, the program *rci92* from the package GRASP92 [98], the predecessor of GRASP2K, should be used at this step due to compatibility reasons.

Depending on the purpose of the calculation, we switch to the RATIP package or proceed with the following GRASP2K programs

- *rbiotransform* and *rtransition* evaluate parameters of transitions between atomic states, such as the energy, the rate and the transition strength. For this calculation the procedure outlined above should be run separately for the initial and the final states.

- *rhfs* calculates the diagonal and off-diagonal hyperfine structure coefficients. Instead of this output, one can extract corresponding matrix elements by editing the source code. We use this approach in Section 2.4, where we obtain the EB excitation rates in highly charged ions.

The RATIP package [48] consists of a number of programs performing multi-electron relativistic atomic calculations with an electron in a continuum state. In the present work we use the program *xphoto* developed initially for calculations of photo-ionization cross-sections. The continuum electron in the photo-ionization process obeys the same selection rules as the IC electron if the initial and the final atomic states in these two processes are identical and the involved photon (which is virtual in the case of IC) has the same multipolarity. By editing the source code of *xphoto*, we extract the continuum electron wave functions and use them for the IC calculations in Chapter 1 and for evaluation of the LANEEC rate in Chapter 3. The output of the GRASP2K calculation consisting of the energies and the wave functions for the involved bound atomic states

serves as an input for *xphoto*. We stress again that at the last step the program *rci92* from the package GRASP92 instead of *rci* from GRASP2K should be used. The procedure described above should be executed separately for the atomic state prior to the ionization and the state of the higher-charge ion produced by the ionization process. During the execution of *xphoto* the user enters the energy and the multipolarity of the ionizing photon.

4.2 Calculations for Th^{3+} ion in a cavity

The calculations described in Chapter 2 for the EB process in the ion ^{229}Th^{3+} contain summation over all possible intermediate electronic states including highly excited and continuum states [see Eq. (2.12)—(2.14)]. As mentioned in Section 2.2, the GRASP2K package is limited in evaluation of excited states already with principal quantum numbers approaching $n = 10$ and cannot provide all needed wave functions. On the other hand, integration over continuum wave functions obtained from the RATIP package is not straightforward. We use instead the procedure described in the following for evaluation of the required matrix elements involving highly excited and continuum electronic states.

4.2.1 Solution of the DHF equations

First, we solve the DHF equations for the Rn-like closed core of Th^{3+} using the numerical method described in Ref. [41]. The DHF system of equations for closed shells can be written in the form [41]

$$\left(\hat{V}_{\text{HF}} - \frac{Z}{r} + c^2 \right) P_a(r) + c \left(\frac{d}{dr} - \frac{\kappa}{r} \right) Q_a(r) = \varepsilon P_a(r) \ , \tag{4.1}$$

$$-c \left(\frac{d}{dr} + \frac{\kappa}{r} \right) P_a(r) + \left(\hat{V}_{\text{HF}} - \frac{Z}{r} - c^2 \right) Q_a(r) = \varepsilon Q_a(r) \ , \tag{4.2}$$

where Z is the charge number of the nucleus, c is the speed of light and $P_a(r)$ and $Q_a(r)$ are the large and the small radial Dirac wave functions in the closed shells enumerated by the index a, respectively. The relativistic quantum number κ represents the angular momentum of the shell, ε is the energy eigenvalue. In accordance with Koopman's theorem [41], ε has the physical meaning of the energy necessary for removing the electron from the shell. The operator $\hat{V}_{\text{HF}}$ acts on the functions $P_a(r)$ and $Q_a(r)$ represented by the generic notation $R_a(r)$ as

$$\hat{V}_{\text{HF}} R_a(r) = \sum_b (2j_b + 1) \left(v_0(b,b,r) R_a(r) - \sum_k \Lambda_{\kappa_a k \kappa_b} v_k(b,a,r) R_b(r) \right) \ , \tag{4.3}$$

where the first summation is carried out over all closed shells enumerated by the index b and the second sum runs over all integer numbers $k \geq 0$. The function v_k is defined as

$$v_k(i,j,r) = \int_0^{+\infty} dr' \frac{r_<^k}{r_>^{k+1}} [P_i(r') P_j(r') + Q_i(r') Q_j(r')] \ , \tag{4.4}$$

with $r_> = \max\{r, r'\}$ and $r_< = \min\{r, r'\}$. The coefficient $\Lambda_{\kappa_a k \kappa_b}$ in (4.3) can be expressed as

$$\Lambda_{\kappa_a k \kappa_b} = \begin{pmatrix} j_a & j_b & k \\ -\frac{1}{2} & \frac{1}{2} & 0 \end{pmatrix}^2 \Pi_{l_a + l_b + k} \ , \tag{4.5}$$

where the function Π defined by the equation (1.16) assures proper parity for the numbers l_a, l_b and k.

The finite nuclear size is taken into account in our calculations by using the charge $Z(r)$ dependent on the distance from the origin. We assume that the nucleus has radius R_n and the charge Z is uniformly distributed in its volume. Then the function $Z(r)$ is given by the expression

$$Z(r) = \begin{cases} \left[\frac{3}{2}\frac{r}{R} - \frac{1}{2}\left(\frac{r}{R}\right)^3\right] Z, & \text{for } r < R_n, \\ Z, & \text{for } r \geq R_n. \end{cases} \tag{4.6}$$

The nuclear radius measured in fm is obtained from the empirical formula [41]

$$R_n = \sqrt{\frac{5}{3}}\left(0.836 A^{\frac{1}{3}} + 0.570\right), \tag{4.7}$$

where A is the mass number of the nucleus.

We solve the DHF system by the method of successive approximations repeated until the relative change in the energy eigenvalue ε reduces to 10^{-9}. The input for the first iteration is evaluated from solving the Dirac equation for each shell corresponding to taking $\hat{V}_{\mathrm{HF}} = 0$. In most cases, a few tens of loops is necessary to achieve convergence.

We proceed now by considering the ion Th^{3+}, which has one electron above the Rn-like closed core. We solve the DHF equation for the valence electron above the closed shells found at the last step. We adopt the so-called frozen-core approximation assuming that the change in the energies and the wave functions of the closed-core orbitals due to the added electron is negligible. The DHF equation for the valence electron has the same form as the equations in the system (4.1) with the only difference that the summation over b in (4.3) is carried out only over the closed shells and does not involve the considered orbital. The method allows to obtain a few low-lying electronic states of Th^{3+}, which serve as an input for the subsequent calculations.

In Table 4.1 we present the obtained low-lying energy levels in Th^{3+} measured with respect to the ground state. For comparison we show also the values calculated in Ref. [30] and the values obtained experimentally [46]. Although a very good agreement with Ref. [30] is achieved, the accuracy of the energy spectrum is not sufficient for calculations in the present work due to the wrong order of the states obtained with the DHF method. This can be explained by the influence of correlation of the valence electron with the closed core leading to significant energy corrections (see later in this Chapter). At the same time, the electronic wave functions obtained with the DHF method have sufficient accuracy.

4.2.2 Expansion in the *B*-spline basis set

As the next step, we consider the ion $^{229}\mathrm{Th}^{3+}$ to be located in a cavity of a radius R very large in comparison with the size of the ion. This implies the condition $P(R) = Q(R) = 0$ on all wave functions $P(r)$ and $Q(r)$ involved in the calculation, making the energy spectrum discrete both for negative and for positive energies. Due to the large size of the cavity, this simplification does not affect the numerical results for the described process in the $^{229}\mathrm{Th}^{3+}$ ion. We solve the DHF equation for the valence electron in the cavity by expansion in the B-spline basis set as described in the following.

We introduce the B-spline basis set as a finite set of N functions $B_1^k(r), B_2^k(r), \ldots, B_N^k(r)$ defined on the interval $r \in [0, R]$. The order k is a positive integer number characteriz-

DHF method			Experiment	
El. state	Present work	Ref. [30]	El. state	Ref. [46]
$6d_{3/2}$	Ground state		$5f_{5/2}$	Ground state
$6d_{5/2}$	4225	4225	$5f_{7/2}$	4325
$5f_{5/2}$	5189	5190	$6d_{3/2}$	9193
$5f_{7/2}$	8615	8617	$6d_{5/2}$	14486
$7s_{1/2}$	11525	11519	$7s_{1/2}$	23131
$7p_{1/2}$	46704	46702	$7p_{1/2}$	60239
$7p_{3/2}$	58227	58225	$7p_{3/2}$	73056

Table 4.1: Energy levels of $^{229}\text{Th}^{3+}$ (in cm^{-1}) obtained in the present work and in Ref. [30] using the DHF method and the corresponding experimental values from Ref. [46]. The low-lying levels obtained numerically have the wrong order.

ing the set. The functions B_i^k are constructed recursively based on $N + k$ knot points $r_1 \leq r_2 \leq \ldots \leq r_{N+k}$ as

$$B_i^1(r) = \begin{cases} 1 , & \text{for } r_i \leq r < r_{i+1} , \\ 0 , & \text{otherwise} , \end{cases} \tag{4.8}$$

$$B_i^k(r) = \frac{r - r_i}{r_{i+k-1} - r_i} B_i^{k-1}(r) + \frac{r_{i+k} - r}{r_{i+k} - r_{i+1}} B_{i+1}^{k-1}(r) . \tag{4.9}$$

We choose k-degenerate knots at the ends of the interval $[0, R]$, such that $r_1 = r_2 = \ldots = r_k = 0$ and $r_{n+1} = r_{n+1} = \ldots = r_{n+k} = R$. The other knot points are exponentially distributed over the interval $[0, R]$ in accordance with the exponential grid used in our calculations. The N functions B_i^k form a complete basis in the space of functions built from polynomials of the $(k-1)$-th power in a piecewise way. Expansion of a function $F(r)$ in this basis set as

$$F(r) = \sum_{i=1}^{N} f_i B_i^k(r) \tag{4.10}$$

is an approximation to this function with accuracy increasing with the number of the B-splines N and their order k. In Fig. 4.1 we show an example of the basis set for $N = 6$ and $k = 4$ on the interval $[0, 1]$. The functions B_i^k are enumerated by their maxima, which follow from left to right. We show in Fig. 4.2 also the B-spline basis for $N = 60$ and $k = 13$, the parameters used in calculations in the present work. Only the functions B_i^k with i starting from approx. 43 are distinguishable in the Figure due to the very high concentration of the B-splines with lower i close to the origin. Such a behavior is sufficient for our calculations as the atomic wave functions have oscillations with a strongly decreasing period at $r \to 0$.

In order to obtain the DHF equations in the B-spline basis set, we use the approach outlined in [41] for the non-relativistic case. We start from the Dirac equation for the valence electron, which can be obtained from the DHF equation by taking $\hat{V}_{\text{HF}} = 0$.
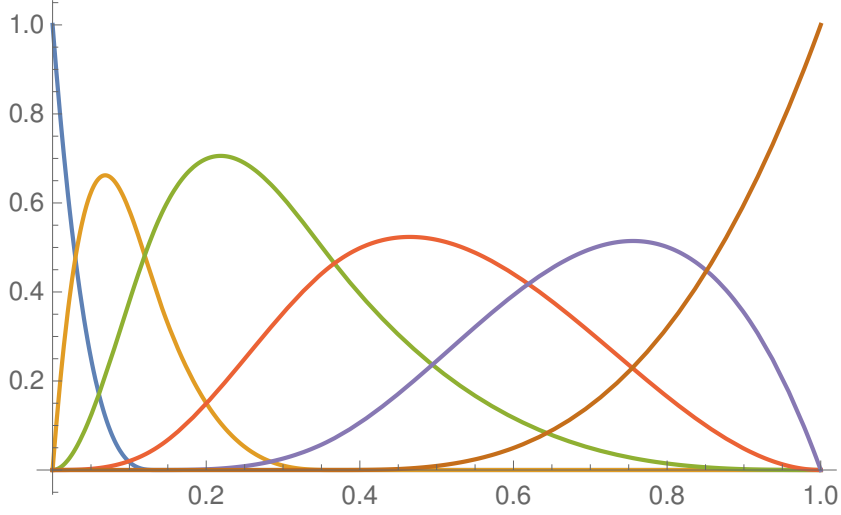
Figure 4.1: The B-spline basis set for $N = 6$ and $k = 4$ on the interval $[0, 1]$. The i-th maximum from left to right corresponds to the function B_i^k. The knots at the ends of the interval are k-degenerate. The other knots are exponentially distributed over the interval $[0, R]$ (see the text for explanations).
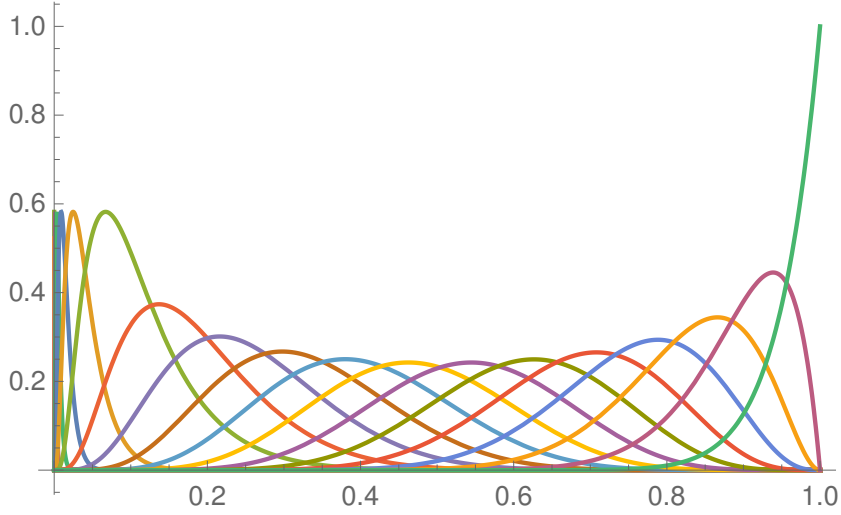

Figure 4.2: The B-spline basis set on the interval $[0, 1]$ for the parameters $N = 60$ and $k = 13$ used in calculations in the present work. The i-th maximum from left to right corresponds to the function B_i^k. The knots at the ends of the interval are k-degenerate. The other knots are exponentially distributed over the interval $[0, R]$ (see the text for explanations). Only the functions with i starting from approx. 43 are distinguishable due to the very high concentration of the B-splines with lower i close to the origin.

Instead of working with the equation itself, we introduce the functional

$$
\begin{aligned}
I \;=\; & \int_0^\infty dr \left\{ P_v \left(-\frac{Z}{r} + c^2 \right) P_v + c P_v \left(\frac{d}{dr} - \frac{\kappa}{r} \right) Q_v - c Q_v \left(\frac{d}{dr} + \frac{\kappa}{r} \right) P_v \right. \\
& \left. + \; Q_v \left(-\frac{Z}{r} - c^2 \right) Q_v \right\} - \varepsilon \int_0^\infty dr \left(P_v^2 + Q_v^2 \right) .
\end{aligned}
\tag{4.11}
$$

The Dirac equation can be obtained by minimizing this functional with respect to P_v and Q_v. We expand the wave functions in the B-spline basis set for a fixed k as

$$P_v = \sum_i p_i B_i^k , \qquad (4.12)$$

$$Q_v = \sum_i q_i B_i^k , \qquad (4.13)$$

where we omit the summation limits assuming that i takes the values from 1 to N. The functional I takes then the form

$$I = \sum_{ij} \left(p_i p_j M_{ij}^1 + q_i q_j M_{ij}^2 + p_i q_j c N_{ij}^1 - q_i p_j c N_{ij}^2 \right) - \varepsilon \sum_{ij} \left(p_i p_j + q_i q_j \right) C_{ij} , \qquad (4.14)$$

where we define the matrices M^1, M^2, N^1, N^2, C by their matrix elements as

$$M_{ij}^1 = \int_0^R dr \left(-\frac{Z}{r} + c^2 \right) B_i^k B_j^k , \qquad (4.15)$$

$$M_{ij}^2 = \int_0^R dr \left(-\frac{Z}{r} - c^2 \right) B_i^k B_j^k , \qquad (4.16)$$

$$N_{ij}^1 = \int_0^R dr B_i^k \left(\frac{d}{dr} - \frac{\kappa}{r} \right) B_j^k , \qquad (4.17)$$

$$N_{ij}^2 = \int_0^R dr B_i^k \left(\frac{d}{dr} + \frac{\kappa}{r} \right) B_j^k , \qquad (4.18)$$

$$C_{ij} = \int_0^R dr B_i^k B_j^k . \qquad (4.19)$$

The variational condition for minimizing the functional I can be written within this framework as

$$\frac{\partial I}{\partial p_i} = 0 , \qquad (4.20)$$

$$\frac{\partial I}{\partial q_i} = 0 , \qquad (4.21)$$

giving

$$\sum_j M_{ij}^1 p_j + c \frac{N_{ij}^1 - N_{ji}^2}{2} q_j = \varepsilon \sum_j C_{ij} p_j , \qquad (4.22)$$

$$\sum_j M_{ij}^2 q_j + c \frac{N_{ji}^1 - N_{ij}^2}{2} p_j = \varepsilon \sum_j C_{ij} q_j . \qquad (4.23)$$

Introducing the vector $(p, q) = (p_1, p_2, \dots, p_N, q_1, q_2, \dots, q_N)$, we rewrite this system of equations in the form

$$\begin{pmatrix} M^1 & N \\ N^T & M^2 \end{pmatrix} \begin{pmatrix} p \\ q \end{pmatrix} = \varepsilon \begin{pmatrix} C & 0 \\ 0 & C \end{pmatrix} \begin{pmatrix} p \\ q \end{pmatrix} , \qquad (4.24)$$

where the matrix N can be expressed via N^1 and N^2 as

$$N_{ij} = c\frac{N_{ij}^1 - N_{ji}^2}{2} \; . \tag{4.25}$$

We note that for $i \neq j$

$$\int_0^R dr\, B_i^k(r)\frac{dB_j^k(r)}{dr} = -\int_0^R dr\, B_j^k(r)\frac{dB_i^k(r)}{dr}. \tag{4.26}$$

This property together with the symmetry of the matrices $\int dr B_i^k B_j^k$ and $\int dr B_i^k \frac{1}{r} B_j^k$ simplifies significantly the numerical solution of the system (4.24).

In the case of a DHF equation with $\hat{V}_{\text{HF}} \neq 0$, the functional (4.11) should be generalized by adding the term

$$I_{DHF} = \sum_b (2j_b + 1)\left[R_0(vbvb) - \sum_k \Lambda_{\kappa_v k \kappa_b} R_k(vbbv)\right] \; , \tag{4.27}$$

where the first summation is carried out over the closed orbitals enumerated by the index b and the second summation is over all integer numbers $k \geq 0$. The radial integral $R_k(abcd)$ with the indices in the parenthesis denoting the corresponding orbitals is given by the expression

$$
\begin{aligned}
R_k(abcd) &= \int_0^R dr\, [P_a(r)P_c(r) + Q_a(r)Q_c(r)] \\
&\times \int_0^R dr'\, \frac{r_<^k}{r_>^{k+1}}[P_b(r')P_d(r') + Q_b(r')Q_d(r')] \; .
\end{aligned}
\tag{4.28}
$$

The radial integrals $R_0(vbvb)$ and $R_k(vbbv)$ in the expression (4.27) represent the contributions of the direct Coulomb interaction and the exchange interaction, respectively. The quantity $R_0(vbvb)$ for the wave functions represented in the B-spline basis set has the form

$$
\begin{aligned}
R_0(vbvb) &= \int_0^R dr\left[P_v^2(r) + Q_v^2(r)\right]\int_0^R dr'\frac{1}{r_>}\left[P_b^2(r') + Q_b^2(r')\right] \\
&= \sum_{ij}(p_ip_j + q_iq_j)\int_0^R dr\, B_i(r)v_0(bbr)B_j(r) \; .
\end{aligned}
\tag{4.29}
$$

After variation of (4.29) by p and q we obtain the additional terms in the matrices M_1 and M_2 due to the direct Coulomb interaction

$$\delta_{dir}M_{ij}^1 = \delta_{dir}M_{ij}^2 = \int_0^R dr\, B_i(r)\left[\sum_b (2j_b + 1)v_0(bbr)\right]B_j(r) \; . \tag{4.30}$$

Analogously we obtain the expression for the exchange radial integral $R_k(vbbv)$

$$
\begin{aligned}
R_k(vbbv) &= \sum_{ij}\iint_{00}^{RR} dr\, dr'\frac{r_<^k}{r_>^{k+1}}[p_iB_i(r)P_b(r) + q_iB_i(r)Q_b(r)] \\
&\times [p_jB_j(r')P_b(r') + q_jB_j(r')Q_b(r')] \; ,
\end{aligned}
\tag{4.31}
$$

leading after variation by p and q to the corrections

$$\delta_{exc}M^1_{ij} \;=\; \int_0^R dr\, B_i(r) \sum_b (2j_b + 1) P_b(r) \sum_k \Lambda_{\kappa_v k \kappa_b} v_k(P_b, B_j, r)\,, \qquad (4.32)$$

$$\delta_{exc}N_{ij} \;=\; \int_0^R dr\, B_i(r) \sum_b (2j_b + 1) P_b(r) \sum_k \Lambda_{\kappa_v k \kappa_b} v_k(Q_b, B_j, r)\,, \qquad (4.33)$$

$$\delta_{exc}M^2_{ij} \;=\; \int_0^R dr\, B_i(r) \sum_b (2j_b + 1) Q_b(r) \sum_k \Lambda_{\kappa_v k \kappa_b} v_k(Q_b, B_j, r)\,, \qquad (4.34)$$

$$\delta_{exc}(N^T)_{ij} \;=\; \int_0^R dr\, B_i(r) \sum_b (2j_b + 1) Q_b(r) \sum_k \Lambda_{\kappa_v k \kappa_b} v_k(P_b, B_j, r)\,. \qquad (4.35)$$

Here $\delta(N^T)$ denotes the correction to the matrix N^T. We note that

$$\delta_{exc}(N^T)_{ij} = \delta_{exc}N_{ji} \qquad (4.36)$$

and thus

$$\delta(N^T) = (\delta N)^T\,. \qquad (4.37)$$

The system (4.24) has $2N$ solutions separated into two classes by an energy gap of approx. $2m_e c^2$, where m_e is the electron mass. The solutions below the gap correspond to the energy eigenvalues $\varepsilon < -m_e c^2$ and represent the positronic continuum states. The solutions above the gap have values ε both smaller and larger than $m_e c^2$, which correspond to the bound electronic and continuum electronic states, respectively. Among the bound levels there are the closed orbitals. We will exclude the rest energy $m_e c^2$ from the value ε in the following.

In our calculations we choose the B-spline parameters $N = 60$, $k = 13$ and the cavity radius $R = 60$—90 a.u.. The DHF corrections to the matrices M and N given by the expressions (4.32)—(4.33) and (4.34)—(4.35) are evaluated using the solutions of the DHF equations for the closed shells obtained before. The system (4.24) is solved using the LAPACK library [99]. We omit completely the positronic part in the obtained spectrum and neglect the contribution of the electronic solutions with very high energies keeping for further calculations only the levels with the principal quantum number up to 20—40 for each orbital. The particular choice depends on the orbital and the value of R. In Table 4.2 we present the energies of the obtained electronic levels for the s-states. For comparison we show also the results obtained by directly solving the DHF equations for the closed shells ($1s$—$6s$) and for the valence electron in the states $7s$, $8s$ and $9s$. The agreement between the obtained values serves as a consistency check of the calculation.

Second-order correction to the electronic energy levels of Th^{3+}

As an example of application of the obtained energies and wave functions, we calculate the second-order corrections to the electronic energy spectrum of the valence electron in Th^{3+}. We show that the right order of the levels is restored when this correction is taken into account, although a discrepancy with the experimental values attributed to higher-order corrections is still present. The second-order correction $E_v^{(2)}$ to the energy

n	B-splines	DHF
1	-4059.7813259202	-4059.7745969898
2	-759.7911089813	-759.7892814904
3	-194.3291670274	-194.3286689654
4	-51.4048251212	-51.404690161
5	-12.7700141327	-12.769982356
6	-3.2373637354	-3.2373573417
7	-0.9125150197	-0.9125138346
8	-0.4975555662	-0.4975551145
9	-0.3164607401	-0.3164605121
10	-0.2195100512	
11	-0.1613136102	
12	-0.123588294	
13	-0.097724893	
14	-0.0790504324	
15	-0.0633339257	
16	-0.0449016735	
17	-0.0242573157	
18	0.0049707182	
19	0.023504848	
20	0.069603357	
21	0.1460859091	
22	0.1503207601	
23	0.3076060309	
24	0.9079095861	
25	2.2586795217	
26	5.0993343497	
27	10.918131342	
28	16.6049208309	
29	16.6325973891	
30	22.8176083828	

Table 4.2: The ns orbitals with their energies in a.u. obtained using expansion in the B-spline basis set and by directly solving the DHF equations.

of the valence orbital v is given by the expression [41]

$$
\begin{aligned}
E_v^{(2)} &= \sum_k \frac{2}{(2k+1)(2j_v+1)} \sum_{abn} \frac{Z_k(vnab)X_k(vnab)}{\varepsilon_v + \varepsilon_n - \varepsilon_a - \varepsilon_b} \\
&- \sum_k \frac{2}{(2k+1)(2j_v+1)} \sum_{bmn} \frac{Z_k(mnvb)X_k(mnvb)}{\varepsilon_m + \varepsilon_n - \varepsilon_v - \varepsilon_b} \;,
\end{aligned}
\tag{4.38}
$$

where k is a non-negative integer number, the summation with the indices a and b is carried out only over the closed shells, whereas the sums with m and n extend only over the shells outside the core (including the orbital v). The quantities X and Z in (4.38)

are defined via the radial integral (4.28) as

$$X_k(mnab) = (-1)^k \langle \kappa_m \| C_k \| \kappa_a \rangle \langle \kappa_n \| C_k \| \kappa_b \rangle R_k(mnab) , \qquad (4.39)$$

$$Z_k(mnab) = X_k(mnab) + \sum_{k'} (2k+1) \left\{ \begin{array}{ccc} j_a & j_m & k \\ j_b & j_n & k' \end{array} \right\} X_{k'}(mnba) . \quad (4.40)$$

The function C_k and its matrix elements are given by the expressions (2.27)—(2.28). In order to improve the quality of the result, we use the experimental values from Ref. [46] for the energies ε in (4.38) where available. From Table 4.3 it is seen that taking

El. state	Present work	Experiment [46]
$5f_{5/2}$	Ground state	
$5f_{7/2}$	4837	4325
$6d_{3/2}$	9429	9193
$6d_{5/2}$	15170	14486
$7s_{1/2}$	21828	23131
$7p_{1/2}$	60058	60239
$7p_{3/2}$	73283	73056

Table 4.3: Energy levels of $^{229}\text{Th}^{3+}$ (in cm^{-1}) obtained in the present work using the DHF method with the second-order correlation corrections and the corresponding experimental values.

into account the correction $E_v^{(2)}$ restores the right order of the levels. The remaining disagreement is attributed to higher-order corrections.

4.2.3 RPA calculations

In Chapter 2 we calculate the EB decay enhancement factors for the $M1$ and $E2$ channels in ^{229}Th using the expressions (2.21) and (2.12)—(2.14). The calculation contains summation over all intermediate electronic states allowed by the corresponding selection rules, including summation over highly excited bound states and integration over continuum states. Considering the ion ^{229}Th to be placed into a cavity with large radius, such that the obtained physical results are not affected, we reduce the problem to summation over the discrete finite spectrum obtained in the way described in Section 4.2.2.

As the first step we use the electronic matrix elements evaluated with the help of the expressions (2.22)—(2.23). As seen from Table 2.1, in the case of the $E2$ channel the obtained EB enhancement factors are satisfactory already at this stage. The results show a good agreement with those from Ref. [30] for the $E2$ channel. At the same time, the $M1$ enhancement factors require further improvement, since the matrix elements of the operator $\hat{\mathcal{T}}_{M1}$ are very sensible to the correlation effects between the valence electron and the frozen core, which often lead to corrections significantly larger than the value obtained with Eq. (2.23). We take into account the correlations using the method of RPA described in the following.

We start from the second-order correction to the matrix element of the operator $\hat{\mathcal{T}}_{\lambda L}$ between the valence electronic states v and w due to the correlation with the closed

core [41]

$$\langle w \| \hat{\mathcal{T}}_{\lambda L} \| v \rangle^{(2)} = \sum_{am} \frac{(-1)^{j_a - j_m + L}}{2L + 1} \frac{\langle a \| \hat{\mathcal{T}}_{\lambda L} \| m \rangle \, Z_L(wmva)}{\varepsilon_a - \varepsilon_m - \omega}$$

$$+ \sum_{am} \frac{(-1)^{j_a - j_m + L}}{2L + 1} \frac{Z_L(wavm) \, \langle m \| \hat{\mathcal{T}}_{\lambda L} \| a \rangle}{\varepsilon_a - \varepsilon_m + \omega} , \qquad (4.41)$$

where $\omega = \varepsilon_w - \varepsilon_v$, the function Z_L is defined by (4.39)—(4.40), and the indices a and m in the sums run over the closed and the excited shells, respectively. The matrix elements $\langle a \| \hat{\mathcal{T}}_L \| m \rangle$ and $\langle m \| \hat{\mathcal{T}}_{\lambda L} \| a \rangle$ in (4.41) describe transitions of the closed shells to the particle-hole states. As the next step, we write the expressions for these matrix elements taking into account their first-order values obtained using the equation (2.23) and second-order corrections [41]

$$\langle a \| \hat{\mathcal{T}}_{\lambda L} \| m \rangle^{(1+2)} = \langle a \| \hat{\mathcal{T}}_{\lambda L} \| m \rangle + \sum_{bn} \frac{(-1)^{j_b - j_n + L}}{2L + 1} \frac{\langle b \| \hat{\mathcal{T}}_{\lambda L} \| n \rangle \, Z_L(anmb)}{\varepsilon_b - \varepsilon_n - \omega}$$

$$+ \sum_{bn} \frac{(-1)^{j_b - j_n + L}}{2L + 1} \frac{Z_L(abmn) \, \langle n \| \hat{\mathcal{T}}_{\lambda L} \| b \rangle}{\varepsilon_b - \varepsilon_n + \omega} , \qquad (4.42)$$

$$\langle m \| \hat{\mathcal{T}}_{\lambda L} \| a \rangle^{(1+2)} = \langle m \| \hat{\mathcal{T}}_{\lambda L} \| a \rangle + \sum_{bn} \frac{(-1)^{j_b - j_n + L}}{2L + 1} \frac{\langle b \| \hat{\mathcal{T}}_{\lambda L} \| n \rangle \, Z_L(nmab)}{\varepsilon_b - \varepsilon_n - \omega}$$

$$+ \sum_{bn} \frac{(-1)^{j_b - j_n + L}}{2L + 1} \frac{Z_L(mban) \, \langle n \| \hat{\mathcal{T}}_{\lambda L} \| b \rangle}{\varepsilon_b - \varepsilon_n + \omega} . \qquad (4.43)$$

The RPA equations are obtained from (4.42)—(4.43) by replacing the matrix elements both on the left-hand side and in the sums on the right hand side by the same approximate matrix elements, which we label by the superscript RPA. We obtain the linear system of equations with respect to the RPA matrix elements

$$\langle a \| \hat{\mathcal{T}}_{\lambda L} \| m \rangle^{\mathrm{RPA}} = \langle a \| \hat{\mathcal{T}}_{\lambda L} \| m \rangle + \sum_{bn} \frac{(-1)^{j_b - j_n + L}}{2L + 1} \frac{\langle b \| \hat{\mathcal{T}}_{\lambda L} \| n \rangle^{\mathrm{RPA}} \, Z_L(anmb)}{\varepsilon_b - \varepsilon_n - \omega}$$

$$+ \sum_{bn} \frac{(-1)^{j_b - j_n + L}}{2L + 1} \frac{Z_L(abmn) \, \langle n \| \hat{\mathcal{T}}_{\lambda L} \| b \rangle^{\mathrm{RPA}}}{\varepsilon_b - \varepsilon_n + \omega} , \qquad (4.44)$$

$$\langle m \| \hat{\mathcal{T}}_{\lambda L} \| a \rangle^{\mathrm{RPA}} = \langle m \| \hat{\mathcal{T}}_{\lambda L} \| a \rangle + \sum_{bn} \frac{(-1)^{j_b - j_n + L}}{2L + 1} \frac{\langle b \| \hat{\mathcal{T}}_{\lambda L} \| n \rangle^{\mathrm{RPA}} \, Z_L(nmab)}{\varepsilon_b - \varepsilon_n - \omega}$$

$$+ \sum_{bn} \frac{(-1)^{j_b - j_n + L}}{2L + 1} \frac{Z_L(mban) \, \langle n \| \hat{\mathcal{T}}_{\lambda L} \| b \rangle^{\mathrm{RPA}}}{\varepsilon_b - \varepsilon_n + \omega} . \qquad (4.45)$$

After solving this system, the found matrix elements $\langle a \| \hat{\mathcal{T}}_{\lambda L} \| m \rangle^{\mathrm{RPA}}$ and $\langle m \| \hat{\mathcal{T}}_{\lambda L} \| a \rangle^{\mathrm{RPA}}$ are used in the equation (4.41) in order to obtain the matrix element $\langle w \| \hat{\mathcal{T}}_{\lambda L} \| v \rangle^{\mathrm{RPA}}$. We note that the RPA-corrected matrix elements include automatically the second-order correlation corrections.

We implement the described approach using the LAPACK library [99] for solving the linear system (4.42)—(4.43). We double check the computation method for the $M1$ matrix elements by calculating the hyperfine structure constant A for different orbitals of the Na atom and comparing with the values available in literature. For the valence

orbital v, A in MHz can be evaluated as [41]

$$A_v = \frac{\mu_I/I}{\sqrt{j_v(j_v + 1)(2j_v + 1)}} \langle v \| \hat{\mathcal{T}}_{M1} \| v \rangle \times 13074.7 \; \text{MHz} , \qquad (4.46)$$

where $I = 3/2$ is the spin and $\mu_I = 2.2176$ is the magnetic moment measured in nuclear magnetons for the ^{23}Na nucleus in the ground state. In Table 4.4 we show the values for A when the matrix element $\langle v \| \hat{\mathcal{T}}_{M1} \| v \rangle$ is obtained with the DHF approach and when the RPA correction is included. For comparison we show also the corresponding results obtained in Ref. [41] and the experimental values for A [41]. The discrepancy of the calculated RPA corrections lies in the acceptable range taking into account the significant disagreement in RPA calculations for $M1$ matrix elements present in literature [70, 71]. Moreover, comparison with the experimental values shows that the combined DHF+RPA method itself is limited in accuracy, although the RPA corrections account for most of the difference between the experimental and the DHF values. In Chapter 2 we applied the described approach to the EB enhancement factors in the case of the $M1$ channel obtaining an accuracy adequate for our purposes.

El. state	Present work			Calculated in Ref. [41]			Experiment [41]
	DHF	RPA	Total	DHF	RPA	Total	
$3s_{1/2}$	623.93	136.21	760.13	623.64	143.60	767.24	885.81
$3p_{1/2}$	63.43	16.29	79.72	63.43	18.90	82.33	94.44
$3p_{3/2}$	12.60	5.84	18.44	12.60	5.41	18.01	18.53
$4s_{1/2}$	150.56	32.75	183.30	150.48	34.21	184.70	202
$4p_{1/2}$	21.03	5.38	26.41	20.99	6.25	27.24	30.6
$4p_{3/2}$	4.17	1.90	6.07	4.17	1.76	5.93	6.01

Table 4.4: Hyperfine structure constant A in MHz for different electronic levels in the ^{23}Na atom. We compare the values obtained in the present work with theoretical values that use the combined DHF and RPA methods and with experimental data, both taken from Ref. [41].

Summary and Outlook

Summary

In this work we have investigated theoretically the coupling of the nuclear isomeric transition in the ^{229}Th isotope to the atomic electrons. We have carried out a detailed analysis of the IC and EB decay of the isomer ^{229m}Th for different states of the atomic shell and values of the energy E_m in the commonly accepted range 7.8 ± 0.5 eV and beyond. Based on the IC and EB processes, we have envisaged novel laser-assisted schemes allowing for efficient excitation of the isomer and accurate determination of the energy E_m and studied the feasibility of the proposed methods using modern laboratory means.

The IC process in a neutral ^{229}Th atom has been investigated in detail in this work. The outcoming IC electrons have not a unique energy but a set of possible energies corresponding to different initial electronic states of the Th atom and final states of the Th$^+$ ion produced by IC. We have obtained the IC electron spectra for a number of values of E_m and different electronic states of the ^{229}Th atom prior to IC. These results can be used for determination of the value E_m based on the experiment described in Ref. [28, 35]. We have calculated the IC and EB rates for different electronic shells in a neutral ^{229}Th atom and ^{229}Th ions and studied the contribution of the $M1$ and $E2$ channels. Although the $E2$ part has been widely disregarded in literature, we have shown that for the actual parameters of the nuclear isomeric transition in ^{229}Th it can be safely neglected only if the nuclear transition couples to a $7s$ electron.

We have put forward a novel experimental scheme based on IC from excited electronic states in ^{229}Th ions which allows to determine the strength of the isomeric transition and estimate the energy E_m. The IC channel forbidden in ^{229}Th ions in the ground electronic state is opened by excitation of the outer electrons using optical laser sources. If the excited electronic state undergoes IC at a rate fast enough compared with its radiative decay, ions of a higher charge state are produced in the process. Detection of such ions and direct comparison of the obtained signal with the case of ^{232}Th which does not possess any nuclear states at optical energies, would indicate the presence of the isomeric state. We have considered different electronic states in ^{229}Th ions and chosen proper candidates based on comparison of their IC rates and radiative decay rates. Given that the energy E_m may lie outside the range 7.8 ± 0.5 eV, we have shown that the scheme based on IC from excited electronic states is applicable for Th$^+$ in the case when E_m lies between approx. 9.0 and 12.0 eV, while Th^{2+} can be used only in the rather unlikely case that E_m is higher than 19.1 eV, but less than 20.0 eV. We have discussed a possible implementation of the proposal at the IGISOL facility, Jyväskylä, Finland.

Based on the EB decay process, we have envisaged a new experimental method for precise measurement of the energy E_m with the help of the laser-induced EB (LIEB) mechanism in the ^{229}Th^{3+} ion. In the LIEB process the EB decay of the nuclear isomeric state ^{229m}Th is induced by an external laser photon absorbed by the electronic shell. Since the energy conservation laws allow only particular energies of the absorbed photon, observation of LIEB can provide the transition energy E_m. We have evaluated the LIEB rates and shown that the proposed approach can be especially efficient if the value E_m

happens to be around 12 eV. In this case the LIEB rate achieved with a commercially available tunable laser source is as high as 10^4 s^{-1}. If E_m lies in the commonly accepted energy range $E_m = 7.8 \pm 0.5$ eV, a UV laser instead of the optical laser should be used. We have shown that in this case a lower but measurable LIEB rate can be achieved. We have discussed a practical implementation including a possible detection scheme for the LIEB process.

We have also studied the possibility to use highly charged ^{229}Th ions with open d and f electronic shells for excitation of the nuclear isomer ^{229m}Th via the inverse EB process with optical lasers. Considering specific excitation schemes in the Th^{35+} and Th^{17+} ions and evaluating the excitation rates, we have shown that this approach has advantages in comparison to usage of the ^{229}Th$^+$ ion. Whereas the ^{229}Th$^+$ ion allows the EB excitation only for particular energies of E_m, the excitation scheme in the Th^{35+} ion is applicable for energies E_m in the entire range 7.8 ± 0.5 eV. The schemes in the Th^{35+} and Th^{17+} ions can be also employed if the isomer energy E_m happens to have a higher value. Another advantage is the possibility to apply higher laser power on HCI which would otherwise induce multi-photon ionization when applied to induce the EB excitation in a ^{229}Th$^+$ ion. We have considered a possible implementation of this approach using the electron beam ion trap (EBIT) at the Max Planck Institute for Nuclear Physics in Heidelberg, Germany for production and trapping of HCI.

The isomer ^{229m}Th can be excited via another nuclear level at 29.19 keV decaying predominantly to the isomeric state. We have proposed and investigated an excitation scheme for the 29.19-keV nuclear state based on the process of laser-assisted nuclear excitation by electron capture (LANEEC), which to the best of our knowledge has not been discussed in literature before. In this mechanism the atomic shell absorbs an external X-ray photon which promotes an electron to a continuum state. This electron recombines then with a vacancy in an inner electronic shell simultaneously driving the nuclear transition. The inner-shell vacancy should be created prior to the described process with another X-ray beam. We have developed a complete theory of LANEEC and applied the obtained results for calculation of the LANEEC rate in a concrete implementation at the SACLA facility. We have also evaluated the rate of the alternative direct nonlinear excitation of the nucleus with two X-ray beams. The comparison has shown that the LANEEC excitation rate is more than ten orders larger than the direct two-photon excitation rate due to the strong enhancement of the process by the electronic shell. Although the excitation rate itself is below the practical interest at the moment, this scheme may find future applications in the field of X-ray quantum optics with nuclei.

We conclude that our results demonstrate the promising efficiency of the nuclear coupling to the atomic shell for the isomeric transition in ^{229}Th. It is therefore quite probable that this coupling will play an important role in next more precise determinations of the isomer state energy, for instance by measurement of the IC electron energies. Furthermore, EB in ion traps might be routinely used in the future to pump the isomeric state. While at present only speculative, it is not unlikely that processes exploiting the nuclear coupling to the atomic shell will also play a role in the future development of the nuclear clock.

Outlook

Some theoretical calculations presented in this thesis could be subject for further refining. For instance, in Chapter 1 when we estimate the IC electron distribution for the experimental setup described in [28, 35], we consider a distribution of the initial excited states proportional to their magnetic quantum number degenracies. This might not be

the case and we could try to model the electron-collision process to include a realistic description of the initial state distribution. As a different aspect, for the EB in HCI presented in Chapter 2 we have restricted ourselves to the near-resonant case and considered a single electronic transition instead of a sum over all possible virtual states as presented in Section 2.3. We recall that our LIEB calculations in Section 2.3 consider the case of ^{229}Th^{3+}, with a single open-shell electron, while for HCI we should take into consideration numerous many-electron configurations corresponding to the open d or f shells.

Apart from improving the accuracy of the present results, several aspects in the nuclear coupling to the atomic shell in ^{229}Th have not been touched yet and could be the subject of further studies. First, the inverse IC process, usually referred to as nuclear excitation by electron capture (NEEC), may allow excitation of the isomeric state in ^{229}Th nuclei irradiated by a monoenergetic electron beam. Since the final electronic state is a bound state, the process is allowed only for discrete set of electron energies. Experimental determination of these energies might allow to evaluate the value of E_m. Although NEEC and its applications have been theoretically studied in detail [84, 85], this particular case of very low energy E_m is still to be examined. We note that the NEEC excitation of the isomer ^{229m}Th in laser-generated plasma may also be possible. The excitation of the low-lying nuclear isomer ^{235m}U at the energy 76 eV in laser-generated plasma via NEEC or nuclear excitation by electronic transition (NEET) has been studied experimentally in recent years (see Ref. [100] and references therein). For the case of ^{229m}Th, excitation in plasma could occur via several such processes with coupling to the atomic shell: NEEC, NEET or EB.

Next, ^{229}Th ions with only a few electrons in the electronic shell may render possible an interesting version of the EB decay mechanism which could also be employed for the isomer excitation. In this case EB involves only one electronic orbital and transitions within the hyperfine splitting structure due to the large energy separation with the other orbitals in the shell. The hyperfine splitting of this level is most pronounced for the 1s orbital in the H-like Th^{89+} ion and even in this case does not exceed 1 eV. The electronic transition energy is therefore very far from the nuclear isomer energy E_m and the resonance condition for the EB process is not satisfied here. Nevertheless, due to very large matrix element of the operator $\hat{\mathcal{T}}$ for the strongly localized electronic orbital, the EB rate turns out to have a considerable value as shown by the recent calculations in Ref. [101]. Such EB decay has been theoretically investigated [101, 102] and the next step would be to consider the excitation mechanism via the inverse process. It would be also of interest to study a possibility of multiphoton absorption from the externally applied laser field in this EB excitation as strong optical lasers could be used in this case.

In the present work we have concentrated on investigation of the decay and excitation mechanisms for the nuclear isomer ^{229m}Th in isolated atomic systems. At the same time, the solid-state-based nuclear frequency standard is also discussed in literature [18]. In this scheme the ^{229}Th isotope is doped into a crystal environment which should be optically transparent at the energy E_m allowing thus direct photoexcitation of the nuclear isomer. For instance, CaF$_2$ is a candidate if the value E_m does not exceed its bandgap of approx. 12.1 eV. The large number of doped ^{229}Th nuclei in this approach would be an advantage for implementation of an accurate nuclear clock. A theoretical study of the ^{229}Th nuclear isomeric transition coupling to the crystal electrons potentially with the formation of crystal defects would be thus important also in the solid-state case.

Finally, we note that all our results were obtained assuming that the energy E_m may

lie in the range 7.8 ± 0.5 eV and beyond. Most of them should be reconsidered and concretized when the energy E_m is known at a better accuracy.

Appendices

Appendix A

Hamiltonian for the nuclear multipole moments' coupling to an atomic electron

In this Appendix we derive the Hamiltonian of the interaction between the nuclear multipole moments and an atomic electron. We start from the Hamiltonian for the interaction of the electron with the electromagnetic field created by the nucleus. In the Coulomb gauge it can be represented as the sum of the Coulomb interaction with the nuclear charge and the magnetic interaction with the nuclear current

$$\hat{H}_{\text{int}} = \int d^3 r_n \frac{\rho_n(\vec{r}_n)}{|\vec{r} - \vec{r}_n|} - \frac{\vec{\alpha}}{c} \int d^3 r_n \frac{\vec{j}_n(\vec{r}_n)}{|\vec{r} - \vec{r}_n|} \, , \qquad (A.1)$$

where $\vec{r}$ denotes the coordinates of the electron, $\rho_n(\vec{r}_n)$ and $\vec{j}_n(\vec{r}_n)$ are the nuclear charge density and the nuclear current density at the point $\vec{r}_n$, respectively. The components of the vector $\vec{\alpha}$ are the 4×4 Dirac matrices α_i which can be expressed via the Pauli matrices as

$$\alpha_i = \begin{pmatrix} 0 & \sigma_i \\ \sigma_i & 0 \end{pmatrix} \qquad (A.2)$$

for $i = 1, \, 2, \, 3$. The vector $c\vec{\alpha}$ is the current operator in the Dirac theory of the electron [103]. We denote the Coulomb and the magnetic interaction terms $\hat{H}_{en}$ and $\hat{H}_{\text{magn}}$, respectively, in order to maintain consistency with the notations in Chapter 3. We make use of the expansion [41]

$$\frac{1}{|\vec{r} - \vec{r}_n|} = \sum_{L,q} \frac{4\pi}{2L + 1} \frac{r_<^L}{r_>^{L+1}} (-1)^q Y_{L,-q}(\hat{r}) Y_{L,q}(\hat{r}_n) \, , \qquad (A.3)$$

where $r_> = \max\{r, r_n\}$, $r_< = \min\{r, r_n\}$ and $Y_{L,q}(\hat{r})$ is the spherical function of argument $\hat{r} = \vec{r}/r$. The Coulomb interaction $\hat{H}_{en}$ can be then written as

$$\hat{H}_{en} = \sum_{L,q} \frac{4\pi}{2L + 1} \int d^3 r_n \frac{r_<^L}{r_>^{L+1}} \rho_n(\vec{r}_n)(-1)^q Y_{L,-q}(\hat{r}) Y_{L,q}(\hat{r}_n) \, . \qquad (A.4)$$

We assume at this point that the nuclear volume is negligible in comparison to the electronic shell so that $r_< = r_n$ and $r_> = r$. This approximation is justified in the present work since we consider the coupling of the nuclear multipole moments to the outer electronic orbitals. We obtain

$$\hat{H}_{en} = \sum_{L,q} (-1)^q \frac{4\pi}{2L + 1} \frac{Y_{L,-q}(\hat{r})}{r^{L+1}} \int d^3 r_n r_n^L \rho_n(\vec{r}_n) Y_{L,q}(\hat{r}_n) \, . \qquad (A.5)$$

We introduce now the electric nuclear multipole moment operator of rank L by its spherical components as

$$\hat{\mathcal{M}}_{EL,q} = \sqrt{\frac{4\pi}{2L+1}} \int d^3 r_n\, r_n^L \rho_n(\vec{r}_n) Y_{L,q}(\hat{r}_n) \,. \tag{A.6}$$

Then the Coulomb interaction takes the form

$$\hat{H}_{en} = \sum_{L,q} (-1)^q \sqrt{\frac{4\pi}{2L+1}} \frac{Y_{L,-q}(\hat{r})}{r^{L+1}} \hat{\mathcal{M}}_{EL,q} \tag{A.7}$$

and can be rewritten as

$$\hat{H}_{en} = \sum_{L,q} (-1)^q \hat{\mathcal{M}}_{EL,q} \hat{\mathcal{T}}_{EL,-q} \,, \tag{A.8}$$

with the electronic coupling operator $\hat{\mathcal{T}}_{EL,q}$ defined as

$$\hat{\mathcal{T}}_{EL,q} = \sqrt{\frac{4\pi}{2L+1}} \frac{Y_{L,q}(\hat{r})}{r^{L+1}} \,. \tag{A.9}$$

Using the expansion (A.3), we obtain analogously the following expression for the magnetic term

$$\hat{H}_{\text{magn}} = -\frac{\vec{\alpha}}{c} \sum_{L,q} (-1)^q \frac{4\pi}{2L+1} \frac{Y_{L,-q}(\hat{r})}{r^{L+1}} \int d^3 r_n r_n^L \vec{j}_n(\vec{r}_n) Y_{L,q}(\hat{r}_n) \,. \tag{A.10}$$

The scalar product $\vec{\alpha} \cdot \vec{j}_n$ can be written via the spherical components of these vectors as

$$\vec{\alpha} \cdot \vec{j}_n = \sum_\sigma (-1)^\sigma \alpha_{-\sigma} j_\sigma = \sum_\sigma (-1)^\sigma (\vec{\alpha} \cdot \vec{\xi}_{-\sigma})(\vec{j}_n \cdot \vec{\xi}_\sigma) \,. \tag{A.11}$$

where the spherical basis vectors $\vec{\xi}_\sigma$ are expressed via the Cartesian unit vectors as

$$\begin{aligned}
\vec{\xi}_{\pm 1} &= \mp \frac{\vec{e}_x \pm i\vec{e}_y}{\sqrt{2}} \,, \\
\vec{\xi}_0 &= \vec{e}_z \,.
\end{aligned} \tag{A.12}$$

We use in the following the vector spherical harmonics

$$\vec{Y}_{LJ}^\mu(\hat{r}) = \sum_{q,\sigma} C_{q\,\sigma\,\mu}^{L\,1\,J} Y_{L,q}(\hat{r}) \vec{\xi}_\sigma \,, \tag{A.13}$$

which are spherical tensors of rank J for $J = L-1$, L, $L+1$. With the help of the orthogonality relations for the Clebsch-Gordan coefficients, this expression can be rewritten as

$$Y_{L,q}(\hat{r})\vec{\xi}_\sigma = \sum_{J,\mu} C_{q\,\sigma\,\mu}^{L\,1\,J} \vec{Y}_{LJ}^\mu(\hat{r}) \,. \tag{A.14}$$

Using (A.11), (A.14) and the properties of the Clebsch-Gordan coefficients, we obtain

$$\hat{H}_{\text{magn}} = -\frac{1}{c} \sum_{L,J,\mu} (-1)^{J-L+\mu} \frac{4\pi}{2L+1} \frac{\vec{\alpha} \cdot \vec{Y}_{LJ}^{-\mu}(\hat{r})}{r^{L+1}} \int d^3 r_n r_n^L \vec{j}_n(\vec{r}_n) \cdot \vec{Y}_{LJ}^\mu(\hat{r}_n) \,. \tag{A.15}$$

The integral in this expression represents the contribution of the current $\vec{j}_n$ to the multipole component $\vec{A}_{J\mu}$ of the vector potential. The vector spherical harmonics $\vec{Y}_{LJ}^{\mu}(\hat{r}_n)$ in the integrand have the parity $(-1)^L$, whereas the vector potential for the magnetic interaction should have the parity $(-1)^J$ [104]. We conclude therefore that the vector spherical harmonics with $L = J \pm 1$ do not contribute to the magnetic interaction and obtain the expression

$$\hat{H}_{\text{magn}} = -\frac{1}{c} \sum_{L,q} (-1)^q \frac{4\pi}{2L+1} \frac{\vec{\alpha} \cdot \vec{Y}_{LL}^{-q}(\hat{r})}{r^{L+1}} \int d^3 r_n r_n^L \, \vec{j}_n(\vec{r}_n) \cdot \vec{Y}_{LL}^q(\hat{r}_n) \, , \qquad (\text{A.16})$$

where we have replaced μ by q. We introduce at this point the magnetic nuclear multipole moment of the rank L as

$$\hat{\mathcal{M}}_{ML,q} = -\frac{i}{c} \sqrt{\frac{L}{L+1}} \sqrt{\frac{4\pi}{2L+1}} \int d^3 r_n r_n^L \, \vec{j}_n(\vec{r}_n) \cdot \vec{Y}_{LL}^q(\hat{r}_n) \, . \qquad (\text{A.17})$$

The magnetic Hamiltonian can be then represented as

$$\hat{H}_{\text{magn}} = -i \sum_{L,q} (-1)^q \sqrt{\frac{4\pi}{2L+1}} \frac{\vec{\alpha} \cdot \vec{Y}_{LL}^{-q}(\hat{r})}{r^{L+1}} M_{L,q} \, . \qquad (\text{A.18})$$

Introducing the electronic coupling operator $\hat{\mathcal{T}}_{ML,q}$ in the magnetic case as

$$\hat{\mathcal{T}}_{ML,q} = -i \sqrt{\frac{4\pi(L+1)}{L(2L+1)}} \frac{\vec{\alpha} \cdot \vec{Y}_{LL}^{-q}(\hat{r})}{r^{L+1}} \, , \qquad (\text{A.19})$$

we rewrite the magnetic Hamiltonian in the form

$$\hat{H}_{\text{magn}} = \sum_{L,q} (-1)^q \hat{\mathcal{M}}_{ML,q} \hat{\mathcal{T}}_{ML,-q} \, . \qquad (\text{A.20})$$

The total Hamiltonian can be then represented as

$$\hat{H}_{\text{int}} = \sum_{\lambda L,q} (-1)^q \hat{\mathcal{M}}_{\lambda L,q} \hat{\mathcal{T}}_{\lambda L,-q} \, , \qquad (\text{A.21})$$

where the generic notation λ depicts the interaction hype (electric or magnetic). The Hamiltonian for the coupling of the nuclear multipole moments to the atomic electron is used throughout the present work in this form.

Appendix B

Graphical method in quantum theory of angular momentum

We introduce here the graphical method in the quantum theory of angular momentum which has been used throughout the present work. This approach allows to simplify significantly calculations with angular momenta couplings by reducing them to illustrative transformations of diagrams constructed in a special way. We use the version of this method described in Ref. [105].

Ket- and bra-vectors

We start from the graphical representation of a state with the total angular momentum j and its projection m. The ket-vector $|jm\rangle$ is depicted by an "outcoming" line with one arrow as

$$|jm\rangle = \vdash\!\!\!\longrightarrow\!\!\!\overset{jm}{\rule{1cm}{0.4pt}} \tag{B.1}$$

while the bra-vector $\langle jm|$ corresponds to an "incoming" line with two arrows

$$\langle jm| = \vdash\!\!\!\longleftarrow\!\!\!\overset{jm}{\rule{1cm}{0.4pt}} \tag{B.2}$$

We note that the orientation of the diagrams in this method can be arbitrary. The scalar product $\langle jm|j'm'\rangle$ is represented as

$$\langle jm|j'm'\rangle = \overset{jm}{\longrightarrow\!\!\!\!\gg}\vdash\overset{j'm'}{\longrightarrow} = \delta_{jj'}\delta_{mm'} \ . \tag{B.3}$$

The projection operator onto the subspace of the states with fixed total angular momentum j is denoted as

$$\sum_m |jm\rangle\langle jm| = \sum_m \vdash\!\overset{jm}{\longrightarrow}\ \overset{jm}{\longrightarrow\!\!\!\gg}\!\dashv = \vdash\!\overset{j}{\longrightarrow}\!\dashv \tag{B.4}$$

Clebsch-Gordan coefficients

We proceed by considering the coupling of two angular momenta j_1 and j_2 to the total angular momentum j which takes the values $|j_1 - j_2|, \ldots, j_1 + j_2$. The corresponding states $|jm\rangle$ are constructed as

$$|jm\rangle = \sum_{m_1 m_2} C^{j_1\ j_2\ j}_{m_1 m_2 m} |j_1 m_1\rangle |j_2 m_2\rangle \ . \tag{B.5}$$

The Clebsch-Gordan coefficient $C^{j_1 \ j_2 \ j}_{m_1 m_2 m}$ can be also denoted as

$$C^{j_1 \ j_2 \ j}_{m_1 m_2 m} = \langle j_1 m_1 \ j_2 m_2 | j m \rangle = \langle j m | j_1 m_1 \ j_2 m_2 \rangle \ . \tag{B.6}$$

These notations often used in literature, allow representation of the Clebsch-Gordan coefficient with the two equivalent diagrams

$$\tag{B.7}$$

which are obtained by merging the graphs for the ket- and bra-vectors in Eq. (B.6) ordered counterclockwise (shown by the sign $+$) or clockwise (shown by the sign $-$). The symmetry relations for the Clebsch-Gordan coefficients can be formulated in terms of transformations of the corresponding diagrams.

Wigner *3j*-symbols

Instead of the Clebsch-Gordan coefficients, it is often convenient to use the Wigner $3j$-symbols defined by the relation

$$C^{j_1 \ j_2 \ j}_{m_1 m_2 m} = (-1)^{j_1 - j_2 + m} \sqrt{2j+1} \begin{pmatrix} j_1 & j_2 & j \\ m_1 & m_2 & -m \end{pmatrix} , \tag{B.8}$$

and represented graphically as

$$\begin{pmatrix} j_1 & j_2 & j \\ m_1 & m_2 & m \end{pmatrix} = \tag{B.9}$$

The change of direction of the line $j_1 m_1$ corresponds to the following transformation of the $3j$-symbol

$$(-1)^{j_1 - m_1} \begin{pmatrix} j_1 & j_2 & j \\ -m_1 & m_2 & m \end{pmatrix} = \tag{B.10}$$

The direction of the other lines can be changed in the same manner. It can be shown from the symmetry properties of the $3j$-coefficients that the sign of the vertex can be changed as

$$= (-1)^{j_1 + j_2 + j_3} \tag{B.11}$$

The relation (B.8) can be then graphically represented as

$$+\ \langle\!\!\!\!\!\begin{smallmatrix} j_1 m_1 \\ \\ j_2 m_2 \end{smallmatrix} \longrightarrow \underline{jm} \ = \ (-1)^{2j_1}\sqrt{2j+1}\ \begin{smallmatrix} j_1 m_1 \\ -\bullet \\ j_2 m_2 \end{smallmatrix} \longrightarrow \underline{jm} \tag{B.12}$$

$$+\ \langle\!\!\!\!\!\begin{smallmatrix} j_1 m_1 \\ \\ j_2 m_2 \end{smallmatrix} \overset{jm}{\longleftarrow\!\!\!\longleftarrow} \ = \ (-1)^{2j_2}\sqrt{2j+1}\ \begin{smallmatrix} j_1 m_1 \\ -\bullet \\ j_2 m_2 \end{smallmatrix} \overset{jm}{\longleftarrow\!\!\!\longleftarrow} \tag{B.13}$$

Transformations of the diagrams

The introduced graphical notations allow to simplify calculation of sums with a few $3j$-symbols. Summation over magnetic quantum numbers is represented by merging the corresponding lines of the $3j$-coefficients in accordance with (B.4). The following rules can be applied to the obtained diagram in order to express it via the standard quantities of the angular momentum theory which are then evaluated numerically [105].

- Change of the direction of an internal line, i.e., a line connecting two $3j$-symbols

$$\bullet\!\!\overset{j}{\longrightarrow}\!\!\bullet \ = \ (-1)^{2j} \ \bullet\!\!\overset{j}{\longleftarrow}\!\!\bullet \tag{B.14}$$

The dashed lines represent the other (incoming or outcoming) lines of the corresponding $3j$-symbols.

- Cutting a diagram connected by three lines

$$\begin{smallmatrix} \overset{j_3}{\longrightarrow} \\ \overset{j_2}{\longrightarrow} \\ \overset{j_1}{\longrightarrow} \end{smallmatrix} \ = \ \begin{smallmatrix} j_3 \\ j_2 \\ j_1 \end{smallmatrix} + \ -\ \begin{smallmatrix} j_3 \\ j_2 \\ j_1 \end{smallmatrix} \tag{B.15}$$

If some lines happen to have different direction, the latter should be changed prior to cutting. If there are more lines connecting parts of the diagrams, the cutting can be performed by subsequent application of the rule for three lines.

99

Orthogonality relations

The Wigner $3j$-coefficients obey two orthogonality conditions, which have in the graphical representation the form

$$\sum_{m_1 m_2} \quad \raisebox{-1em}{[diagram]} \quad = \quad \raisebox{-1em}{[diagram]} \quad = \delta_{j_1 j_2}\delta_{m_1 m_2} \;, \quad \text{(B.16)}$$

$$\sum_{jm} \quad \raisebox{-1em}{[diagram]} \quad = \sum_{j} \quad \raisebox{-1em}{[diagram]} \quad = \delta_{m_1 m_1'}\delta_{m_2 m_2'} \quad \text{(B.17)}$$

These graphical rules are also useful for simplification of the diagrams.

6j- and *9j*-symbols

Evaluation of sums with a few Clebsch-Gordan coefficients or $3j$-symbols involves often the so called $6j$- and $9j$-symbols. They can be introduced with the help of the $3j$-symbols represented by the corresponding diagrams. The $6j$-symbol is defined as

$$\left\{ \begin{array}{ccc} j_1 & j_2 & j_3 \\ J_1 & J_2 & J_3 \end{array} \right\} = \sum_{m_\bullet M_\bullet} \quad \raisebox{-1em}{[diagram]} \quad \text{(B.18)}$$

where the summation if carried out aver all indices m and M. Connecting the lines with the same angular momentum and applying the rule for changing the direction of internal lines, we obtain the graphical representation for the $6j$-symbol in the two equivalent forms

$$\left\{ \begin{array}{ccc} j_1 & j_2 & j_3 \\ J_1 & J_2 & J_3 \end{array} \right\} = \quad \raisebox{-2em}{[diagram]} \quad = \quad \raisebox{-2em}{[diagram]} \quad \text{(B.19)}$$

Analogously, the graphical representation of the $9j$-symbol can be obtained. In this case six connected $3j$-coefficients are involved resulting in the diagram

$$
\left\{
\begin{array}{ccc}
j_1 & j_2 & j_3 \\
l_1 & l_2 & l_3 \\
k_1 & k_2 & k_3
\end{array}
\right\} = +
$$

$$(B.20)$$

Wigner-Eckart theorem

In accordance with the Wigner-Eckart theorem [39], matrix elements of an irreducible tensor operator T_{JM} can be written via the corresponding RME as

$$
\langle j_1 m_1 | T_{JM} | j_2 m_2 \rangle = (-1)^{j_1 - m_1}
\begin{pmatrix}
j_1 & J & j_2 \\
-m_1 & M & m_2
\end{pmatrix}
\langle j_1 \| T_J \| j_2 \rangle \ .
$$

$$(B.21)$$

This theorem can be represented graphically as

$$
\langle j_1 m_1 | T_{JM} | j_2 m_2 \rangle = \langle j_1 \| T_J \| j_2 \rangle
$$

$$(B.22)$$

The circle at the vertex of the $3j$-symbol denotes multiplication by the corresponding RME.

Appendix C

Matrix elements of the electronic coupling operator

We derive in this Appendix the one-electron RME $\langle \gamma_a \kappa_a \| \hat{\mathcal{T}} \| \gamma_b \kappa_b \rangle$ of the coupling operator $\hat{\mathcal{T}}$ given by the expressions (A.9) and (A.19) for the electric and magnetic type, respectively. The generic notation γ here stands for the (discrete or continuous) quantities which together with κ and m completely describe the electronic state. The RME for the operator $\hat{\mathcal{T}}_{EL}$ reduces to the RME of the spherical harmonic Y_L as

$$
\begin{aligned}
\langle \gamma_a \kappa_a \| \hat{\mathcal{T}}_{EL} \| \gamma_b \kappa_b \rangle &= \sqrt{\frac{4\pi}{2L+1}} \langle \kappa_a \| Y_L \| \kappa_b \rangle \\
&\times \int_0^\infty \frac{dr}{r^{L+1}} \Big(P_{\gamma_a \kappa_a}(r) P_{\gamma_b \kappa_b}(r) + Q_{\gamma_a \kappa_a}(r) Q_{\gamma_b \kappa_b}(r) \Big). \quad \text{(C.1)}
\end{aligned}
$$

Using the expression [41]

$$
\langle \kappa_a \| Y_L \| \kappa_b \rangle = (-1)^{j_a + \frac{1}{2}} \Pi_{l_a + l_b + L} \sqrt{\frac{(2j_a + 1)(2j_b + 1)(2L + 1)}{4\pi}} \begin{pmatrix} j_a & j_b & L \\ -\frac{1}{2} & \frac{1}{2} & 0 \end{pmatrix} \quad \text{(C.2)}
$$

and the properties of the $3j$-coefficients [69], we obtain

$$
\langle \gamma_a \kappa_a \| \hat{\mathcal{T}}_{EL} \| \gamma_b \kappa_b \rangle = (-1)^{L + \frac{1}{2} - j_b} \Pi_{l_a + l_b + L} \sqrt{(2j_a + 1)(2j_b + 1)} \begin{pmatrix} j_a & j_b & L \\ \frac{1}{2} & -\frac{1}{2} & 0 \end{pmatrix} R_{ab}^{EL}, \quad \text{(C.3)}
$$

where we introduce the radial integral

$$
R_{ab}^{EL} = \int_0^\infty \frac{dr}{r^{L+1}} \Big(P_{\gamma_a \kappa_a}(r) P_{\gamma_b \kappa_b}(r) + Q_{\gamma_a \kappa_a}(r) Q_{\gamma_b \kappa_b}(r) \Big). \quad \text{(C.4)}
$$

In the case of the magnetic type we obtain the expression

$$
\langle \gamma_a \kappa_a \| \hat{\mathcal{T}}_{ML} \| \gamma_b \kappa_b \rangle = -i \sqrt{\frac{4\pi(L+1)}{L(2L+1)}} \left\langle \gamma_a \kappa_a \left\| \frac{\vec{\alpha} \cdot \vec{Y}_{LL}}{r^{L+1}} \right\| \gamma_b \kappa_b \right\rangle, \quad \text{(C.5)}
$$

which after substitution of the electronic wave functions and the Dirac matrices α_i expressed via the Pauli matrices σ_i takes the form

$$
\begin{aligned}
\langle \gamma_a \kappa_a \| \hat{\mathcal{T}}_{ML} \| \gamma_b \kappa_b \rangle &= \sqrt{\frac{4\pi(L+1)}{L(2L+1)}} \bigg(\langle \kappa_a \| \vec{\sigma} \cdot \vec{Y}_{LL} \| -\kappa_b \rangle \int_0^\infty \frac{dr}{r^{L+1}} P_{\gamma_a \kappa_a}(r) Q_{\gamma_b \kappa_b}(r) \\
&- \langle -\kappa_a \| \vec{\sigma} \cdot \vec{Y}_{LL} \| \kappa_b \rangle \int_0^\infty \frac{dr}{r^{L+1}} Q_{\gamma_a \kappa_a}(r) P_{\gamma_b \kappa_b}(r) \bigg). \quad \text{(C.6)}
\end{aligned}
$$

We proceed with the evaluation of the matrix elements of the form $\langle \kappa_a \| \, \vec{\sigma} \cdot \vec{Y}_{LL} \, \| \kappa_b \rangle$ using the graphical method introduced in Appendix B. The ket- and bra-vectors here are the spherical spinors which can be constructed from the spherical harmonics Y_{lm_l} and the two-component spin wave functions χ_{m_s} as

$$\Omega_{\kappa m}(\hat{r}) = \sum_{m_l m_s} C^{l \quad \frac{1}{2} \quad j}_{m_l m_s m} Y_{lm_l}(\hat{r}) \chi_{m_s} \,. \tag{C.7}$$

The graphical representation of $\Omega_{\kappa m}(\hat{r})$ has correspondingly the form

$$\Omega_{\kappa m}(\hat{r}) = \sum_{m_l m_s} \qquad\qquad = \qquad\qquad \tag{C.8}$$

Analogously we find

$$\Omega^{\dagger}_{\kappa m}(\hat{r}) = \qquad\qquad \tag{C.9}$$

The expression $\vec{\sigma} \cdot \vec{Y}^M_{LL}$ can be rewritten in the form

$$\vec{\sigma} \cdot \vec{Y}^M_{LL}(\hat{r}) = \sum_{\mu,\nu} C^{L 1 L}_{\mu \nu M} Y_{L,\mu}(\hat{r}) \sigma_\nu \,. \tag{C.10}$$

Here the operator $\sigma_\nu = \vec{\sigma} \cdot \vec{\xi}_\nu$ acts on the spin wave functions. At the same time, this product is a tensor of rank 1 due to the quantity $\vec{\xi}_\nu$. The expression (C.10) can be represented graphically as

$$\vec{\sigma} \cdot \vec{Y}^M_{LL} = \qquad\qquad \tag{C.11}$$

We note that in the introduced diagrams the lines with the angular momenta L and l ("orbital" lines) correspond to the states described by the angular variables, whereas the lines labeled as $\frac{1}{2}$ and 1 ("spin" lines) represent the states in the two-component spinor space in accordance with (C.7) and (C.10). The matrix element $\langle \kappa_a m_a | \, \vec{\sigma} \cdot \vec{Y}^M_{LL} \, | \kappa_b m_b \rangle$ can be constructed from these diagrams with the help of the graphical representation of the Wigner-Eckart theorem (see Appendix B) applied separately to the orbital and the

spin lines. This results in the graph

$$
\text{(C.12)}
$$
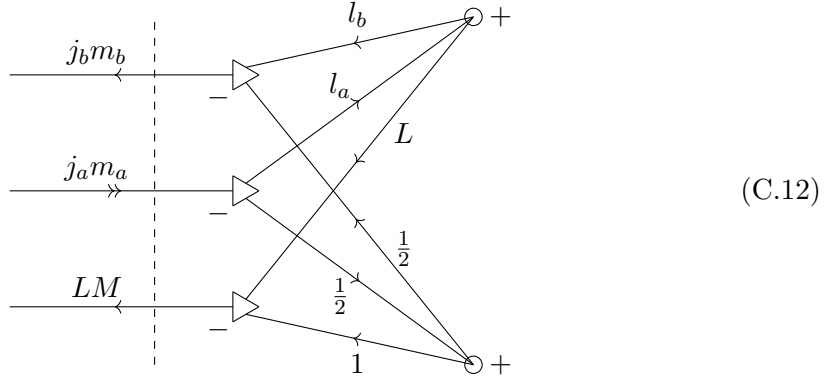
We cut this diagram as shown by the dashed line obtaining

$$
\text{(C.13)}
$$
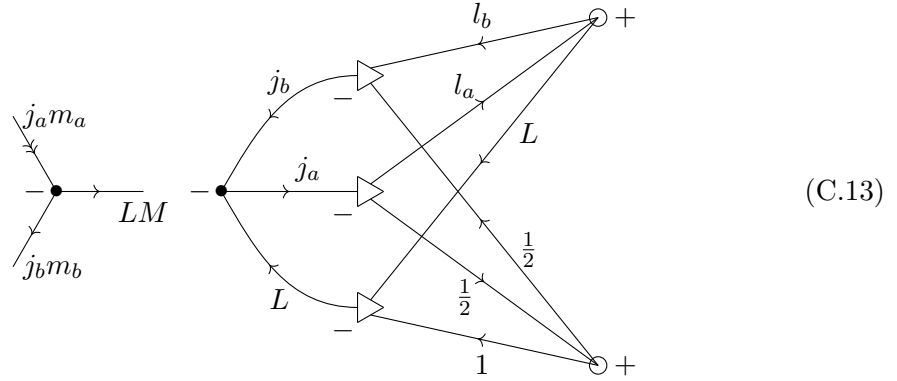
It is seen from comparison to the graphical version of the Wigner-Eckart theorem, that the right separated part of this diagram is the RME $\langle \kappa_a \| \, \vec{\sigma} \cdot \vec{Y}_{LL} \, \| \kappa_b \rangle$. We work further only with this part changing the Clebsch-Gordan coefficients to the $3j$-symbols

$$
\text{(C.14)}
$$
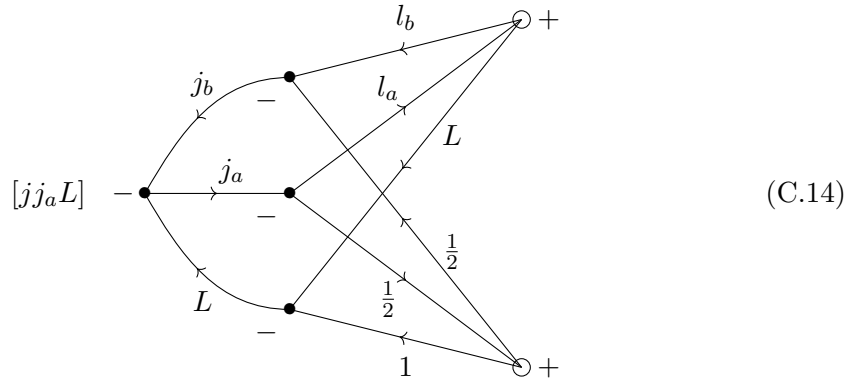
We use here a compact notation $[j_1 j_2 \ldots j_n] = \sqrt{(2j_1 + 1)(2j_2 + 1) \ldots (2j_n + 1)}$. The RME corresponding to the $3j$-symbol with the angular momenta l_a, l_b, L (upper circle

in the graph) is the RME of the spherical harmonic of rank L and can be represented as

$$\frac{[l_a l_b L]}{\sqrt{4\pi}} \quad \text{(C.15)}$$

The diagram (C.14) can be redrawn as

$$\frac{[j j_a L l_a l_b L]}{\sqrt{4\pi}} \quad \text{(C.16)}$$

Indeed, cutting this graph as shown by the dashed line we would obtain again the diagram (C.14). We consider the $3j$-symbol marked by the blue arrow and given by the diagram

$$\sim \begin{pmatrix} L & 1 & L \\ 0 & -\mu & \mu \end{pmatrix}. \quad \text{(C.17)}$$

The diagram (C.16) contains summation over the introduced magnetic quantum number μ. Taking into account

$$\begin{pmatrix} L & 1 & L \\ 0 & 0 & 0 \end{pmatrix} = 0 \,, \quad \text{(C.18)}$$

we obtain that μ takes only the values ± 1 in (C.16). Moreover, it can be seen from the graph (C.16) that both values define uniquely the magnetic quantum numbers of the other $3j$-coefficients. The diagram (C.16) splits then into a product of the corresponding $3j$-symbols for each value of μ. For instance, in the case $\mu = 1$ we have

$$\frac{[j j_a L l_a l_b L]}{\sqrt{4\pi}} \quad \text{(C.19)}$$

The RME $\langle\kappa_a\|\,\vec{\sigma}\cdot\vec{Y}_{LL}\,\|\kappa_b\rangle$ can be obtained by evaluating this product separately for $\mu = 1$ and $\mu = -1$ and summing the results. The RME denoted in (C.16) by the circle is $\left\langle\frac{1}{2}\middle\|\sigma\middle\|\frac{1}{2}\right\rangle$ accordingly to the expression (C.10). Its numerical value is [69]

$$\left\langle\frac{1}{2}\middle\|\sigma\middle\|\frac{1}{2}\right\rangle = \sqrt{6}\,. \tag{C.20}$$

The expressions for the $3j$-symbols involved in the products can be taken from Ref [69]. We obtain

$$\langle\kappa_a\|\,\vec{\sigma}\cdot\vec{Y}_{LL}\,\|\kappa_b\rangle = (-1)^{l_a}\Pi_{l_a+l_b+L+1}\sqrt{\frac{(2j_a+1)(2j_b+1)(2L+1)}{4\pi}}$$
$$\times\begin{pmatrix} j_b & j_a & L \\ -\frac{1}{2} & -\frac{1}{2} & 1 \end{pmatrix}\,. \tag{C.21}$$

We have introduced in this expression the parity condition $\Pi_{l_a+l_b+L+1}$. The matrix elements $\langle\gamma_a\kappa_a\|\,\hat{\mathcal{T}}_{ML}\,\|\gamma_b\kappa_b\rangle$ can be now obtained using (C.6)

$$\langle\gamma_a\kappa_a\|\,\hat{\mathcal{T}}_{ML}\,\|\gamma_b\kappa_b\rangle = (-1)^{l_a}\Pi_{l_a+l_b+L+1}\sqrt{\frac{(2j_a+1)(2j_b+1)(L+1)}{L}}$$
$$\times\begin{pmatrix} j_a & j_b & L \\ -\frac{1}{2} & -\frac{1}{2} & 1 \end{pmatrix}R_{ab}^{ML}\,, \tag{C.22}$$

where we introduce the radial integral

$$R_{ab}^{ML} = \int_0^\infty \frac{dr}{r^{L+1}}\Big(P_{\gamma_a\kappa_a}(r)Q_{\gamma_b\kappa_b}(r) + Q_{\gamma_a\kappa_a}(r)P_{\gamma_b\kappa_b}(r)\Big)\,. \tag{C.23}$$

We transform this expression using the relation [106]

$$\begin{pmatrix} j_a & j_b & L \\ -\frac{1}{2} & -\frac{1}{2} & 1 \end{pmatrix} = -\frac{1}{2}\begin{pmatrix} j_a & j_b & L \\ -\frac{1}{2} & \frac{1}{2} & 0 \end{pmatrix}\frac{(2j_b+1)+(-1)^{j_a+j_b+L}(2j_a+1)}{\sqrt{L(L+1)}}\,, \tag{C.24}$$

which under the parity condition defined by $\Pi_{l_a+l_b+L+1}$ can be rewritten as

$$\begin{pmatrix} j_a & j_b & L \\ -\frac{1}{2} & -\frac{1}{2} & 1 \end{pmatrix} = (-1)^{j_b-l_b-\frac{1}{2}}\frac{\kappa_a+\kappa_b}{\sqrt{L(L+1)}}\begin{pmatrix} j_a & j_b & L \\ -\frac{1}{2} & \frac{1}{2} & 0 \end{pmatrix}\,. \tag{C.25}$$

We obtain finally the magnetic electronic RME

$$\langle\gamma_a\kappa_a\|\,\hat{\mathcal{T}}_{ML}\,\|\gamma_b\kappa_b\rangle = (-1)^{j_b+L+\frac{1}{2}}\frac{\sqrt{(2j_a+1)(2j_b+1)}}{L}$$
$$\times (\kappa_a+\kappa_b)\begin{pmatrix} j_a & j_b & L \\ -\frac{1}{2} & \frac{1}{2} & 0 \end{pmatrix}R_{ab}^{ML}\,. \tag{C.26}$$

Bibliography

[1] https://physics.nist.gov/cuu/Units/second.html, accessed: 2018-09-24.

[2] Anonymous, "Meeting at New York, January 19 and 20, 1945," Phys. Rev. **67**, 199 (1945).

[3] I. I. Rabi, J. R. Zacharias, S. Millman, and P. Kusch, "A New Method of Measuring Nuclear Magnetic Moment," Phys. Rev. **53**, 318 (1938).

[4] L. Essen and J. V. L. Parry, "An Atomic Standard of Frequency and Time Interval: A Cæsium Resonator," Nature **176**, 280 (1955).

[5] F. Riehle, *Frequency Standards: Basics and Applications* (John Wiley & Sons, Inc., 2006).

[6] R. W. P. Drever, J. L. Hall, F. V. Kowalski, J. Hough, G. M. Ford, A. J. Munley, and H. Ward, "Laser phase and frequency stabilization using an optical resonator," Applied Physics B **31**, 97 (1983).

[7] J. L. Hall, "Nobel Lecture: Defining and measuring optical frequencies," Rev. Mod. Phys. **78**, 1279 (2006).

[8] T. W. Hänsch, "Nobel Lecture: Passion for precision," Rev. Mod. Phys. **78**, 1297 (2006).

[9] T. Rosenband, D. B. Hume, P. O. Schmidt, C. W. Chou, A. Brusch, L. Lorini, W. H. Oskay, R. E. Drullinger, T. M. Fortier, J. E. Stalnaker, S. A. Diddams, W. C. Swann, N. R. Newbury, W. M. Itano, D. J. Wineland, and J. C. Bergquist, "Frequency Ratio of Al^+ and Hg^+ Single-Ion Optical Clocks; Metrology at the 17th Decimal Place," Science **319**, 1808 (2008).

[10] C. W. Chou, D. B. Hume, J. C. J. Koelemeij, D. J. Wineland, and T. Rosenband, "Frequency Comparison of Two High-Accuracy Al^+ Optical Clocks," Phys. Rev. Lett. **104**, 070802 (2010).

[11] N. Hinkley, J. A. Sherman, N. B. Phillips, M. Schioppo, N. D. Lemke, K. Beloy, M. Pizzocaro, C. W. Oates, and A. D. Ludlow, "An Atomic Clock with 10^{18} Instability," Science **341**, 1215 (2013).

[12] T. L. Nicholson, S. L. Campbell, R. B. Hutson, G. E. Marti, B. J. Bloom, R. L. McNally, W. Zhang, M. D. Barrett, M. S. Safronova, G. F. Strouse, W. L. Tew, and J. Ye, "Systematic evaluation of an atomic clock at $2 \cdot 10^{-18}$ total uncertainty," Nature Communications **6**, 6896 (2015).

[13] G. E. Marti, R. B. Hutson, A. Goban, S. L. Campbell, N. Poli, and J. Ye, "Imaging Optical Frequencies with 100 μHz Precision and 1.1 μm Resolution," Phys. Rev. Lett. **120**, 103201 (2018).

[14] B. R. Beck, J. A. Becker, P. Beiersdorfer, G. V. Brown, K. J. Moody, J. B. Wilhelmy, F. S. Porter, C. A. Kilbourne, and R. L. Kelley, "Energy Splitting of the Ground-State Doublet in the Nucleus ^{229}Th," Phys. Rev. Lett. **98**, 142501 (2007).

[15] *12th International Conference on Nuclear Reaction Mechanisms*, Vol. LLNL-PROC-415170 (Varenna, Italy, 2009).

[16] E. Peik and C. Tamm, "Nuclear spectroscopy of the 3.5 eV transition in Th-229," Europhys. Lett. **61**, 181 (2003).

[17] C. J. Campbell, A. G. Radnaev, A. Kuzmich, V. A. Dzuba, V. V. Flambaum, and A. Derevianko, "Single-Ion Nuclear Clock for Metrology at the 19th Decimal Place," Phys. Rev. Lett. **108**, 120802 (2012).

[18] E. Peik and M. Okhapkin, "Nuclear clocks based on resonant excitation of γ-transitions," Comptes Rendus Physique **16**, 516 (2015).

[19] J. C. Berengut, V. A. Dzuba, V. V. Flambaum, and S. G. Porsev, "Proposed Experimental Method to Determine α Sensitivity of Splitting between Ground and 7.6 eV Isomeric States in ^{229}Th," Phys. Rev. Lett. **102**, 210801 (2009).

[20] A. Arvanitaki, J. Huang, and K. Van Tilburg, "Searching for dilaton dark matter with atomic clocks," Phys. Rev. D **91**, 015015 (2015).

[21] E. V. Tkalya, "Proposal for a Nuclear Gamma-Ray Laser of Optical Range," Phys. Rev. Lett. **106**, 162501 (2011).

[22] W.-T. Liao, S. Das, C. H. Keitel, and A. Pálffy, "Coherence-Enhanced Optical Determination of the ^{229}Th Isomeric Transition," Phys. Rev. Lett. **109**, 262502 (2012).

[23] L. Kroger and C. Reich, "Features of the low-energy level scheme of ^{229}Th as observed in the α-decay of ^{233}U," Nuclear Physics A **259**, 29 (1976).

[24] C. Reich, R. Helmer, J. Baker, and R. Gehrke, "Emission probabilities and energies of γ-ray transitions from the decay of ^{233}U," The International Journal of Applied Radiation and Isotopes **35**, 185 (1984).

[25] C. W. Reich and R. G. Helmer, "Energy separation of the doublet of intrinsic states at the ground state of ^{229}Th," Phys. Rev. Lett. **64**, 271 (1990).

[26] R. G. Helmer and C. W. Reich, "An excited state of ^{229}Th at 3.5 eV," Phys. Rev. C **49**, 1845 (1994).

[27] Z. O. Guimarães Filho and O. Helene, "Energy of the $3/2^+$ state of ^{229}Th reexamined," Phys. Rev. C **71**, 044303 (2005).

[28] L. von der Wense, B. Seiferle, M. Laatiaoui, J. B. Neumayr, H.-J. Maier, H.-F. Wirth, C. Mokry, J. Runke, K. Eberhardt, C. E. Düllmann, N. G. Trautmann, and P. G. Thirolf, "Direct detection of the ^{229}Th nuclear clock transition," Nature **533**, 47 (2016).

[29] B. Seiferle, L. von der Wense, and P. G. Thirolf, "Lifetime Measurement of the ^{229}Th Nuclear Isomer," Phys. Rev. Lett. **118**, 042501 (2017).

[30] S. G. Porsev and V. V. Flambaum, "Effect of atomic electrons on the 7.6-eV nuclear transition in ^{229}Th^{3+}," Phys. Rev. A **81**, 032504 (2010).

[31] S. G. Porsev and V. V. Flambaum, "Electronic bridge process in ^{229}Th^{+}," Phys. Rev. A **81**, 042516 (2010).

[32] J. Jeet, C. Schneider, S. T. Sullivan, W. G. Rellergert, S. Mirzadeh, A. Cassanho, H. P. Jenssen, E. V. Tkalya, and E. R. Hudson, "Results of a Direct Search Using Synchrotron Radiation for the Low-Energy ^{229}Th Nuclear Isomeric Transition," Phys. Rev. Lett. **114**, 253001 (2015).

[33] A. Yamaguchi, M. Kolbe, H. Kaser, T. Reichel, A. Gottwald, and E. Peik, "Experimental search for the low-energy nuclear transition in ^{229}Th with undulator radiation," New Journal of Physics **17**, 053053 (2015).

[34] S. G. Porsev, V. V. Flambaum, E. Peik, and C. Tamm, "Excitation of the Isomeric ^{229m}Th Nuclear State via an Electronic Bridge Process in ^{229}Th^{+}," Phys. Rev. Lett. **105**, 182501 (2010).

[35] B. Seiferle, L. von der Wense, and P. G. Thirolf, "Feasibility study of internal conversion electron spectroscopy of 229mTh," The European Physical Journal A **53**, 108 (2017).

[36] `http://physics.nist.gov/PhysRefData/ASD/ionEnergy.html`, accessed: 2018-08-08.

[37] D. R. Lide, *CRC Handbook of Chemistry and Physics* (CRC Press. Boca Raton, Florida, 2003).

[38] P. V. Bilous, G. A. Kazakov, I. D. Moore, T. Schumm, and A. Pálffy, "Internal conversion from excited electronic states of ^{229}Th ions," Phys. Rev. A **95**, 032503 (2017).

[39] A. R. Edmonds, *Angular Momentum in Quantum Mechanics* (Princeton University Press, Princeton, 1996).

[40] J. Eichler and W. Meyerhof, *Relativistic Atomic Collisions* (Academic Press, 1995).

[41] W. R. Johnson, *Atomic Structure Theory: Lectures on Atomic Physics* (Springer, New York, 2007).

[42] A. M. Dykhne and E. V. Tkalya, "Matrix element of the anomalously low-energy $(3.5 \pm 0.5$ eV) transition in ^{229}Th and the isomer lifetime," JETP Lett. **67**, 251 (1998).

[43] E. V. Tkalya, C. Schneider, J. Jeet, and E. R. Hudson, "Radiative lifetime and energy of the low-energy isomeric level in ^{229}Th," Phys. Rev. C **92**, 054324 (2015).

[44] N. Minkov and A. Pálffy, "Reduced Transition Probabilities for the Gamma Decay of the 7.8 eV Isomer in ^{229}Th," Phys. Rev. Lett. **118**, 212501 (2017).

[45] P. V. Bilous, N. Minkov, and A. Pálffy, "Electric quadrupole channel of the 7.8 eV ^{229}Th transition," Phys. Rev. C **97**, 044320 (2018).

[46] `http://web2.lac.u-psud.fr/lac/Database/Tab-energy/Thorium/`, accessed: 2018-08-08.

[47] P. Jönsson, G. Gaigalas, J. Bieron, C. F. Fischer, and I. P. Grant, "New version: Grasp2K relativistic atomic structure package," Computer Physics Communications **184**, 2197 (2013).

[48] S. Fritzsche, "The RATIP program for relativistic calculations of atomic transition, ionization and recombination properties," Computer Physics Communications **183**, 1525 (2012).

[49] F. Rösel, H. Fries, K. Alder, and H. Pauli, "Internal conversion coefficients for all atomic shells," Atomic Data and Nuclear Data Tables **21**, 91 (1978).

[50] T. Kibédi, T. Burrows, M. Trzhaskovskaya, P. Davidson, and C. Nestor, "Evaluation of theoretical conversion coefficients using BrIcc," Nuclear Instruments and Methods in Physics Research Section A: Accelerators, Spectrometers, Detectors and Associated Equipment **589**, 202 (2008).

[51] P. Borisyuk, E. Chubunova, N. Kolachevsky, Y. Lebedinskii, O. Vasiliev, and E. Tkalya, (2018), arXiv:1804.00299 [nucl-th] .

[52] A. Kramida, Yu. Ralchenko, J. Reader, and and NIST ASD Team, NIST Atomic Spectra Database (ver. 5.5.6) Available online: `https://physics.nist.gov/asd`. National Institute of Standards and Technology, Gaithersburg, MD. (2018), accessed: 2018-09-19.

[53] V. Barci, G. Ardisson, G. Barci-Funel, B. Weiss, O. El Samad, and R. K. Sheline, "Nuclear structure of ^{229}Th from γ-ray spectroscopy study ^{233}U α-particle decay," Phys. Rev. C **68**, 034329 (2003).

[54] J. Thielking, M. V. Okhapkin, P. Glowacki, D. M. Meier, L. von der Wense, B. Seiferle, C. E. Düllmann, P. G. Thirolf, and E. Peik, "Laser spectroscopic characterization of the nuclear-clock isomer ^{229m}Th," Nature **556**, 321 (2018).

[55] E. V. Tkalya, "Excitation of low-lying isomer level of the nucleus ^{229}Th by optical photons," JETP Lett. **55**, 211 (1992).

[56] M. Reponen, I. D. Moore, T. Kessler, I. Pohjalainen, S. Rothe, and V. Sonnenschein, "Laser developments and resonance ionization spectroscopy at IGISOL," The European Physical Journal A **48**, 45 (2012).

[57] V. Sonnenschein, I. D. Moore, S. Raeder, A. Hakimi, A. Popov, and K. Wendt, "The search for the existence of ^{229m}Th at IGISOL," The European Physical Journal A **48**, 52 (2012).

[58] M. V. Okhapkin, D. M. Meier, E. Peik, M. S. Safronova, M. G. Kozlov, and S. G. Porsev, "Observation of an unexpected negative isotope shift in ^{229}Th^{+} and its theoretical explanation," Phys. Rev. A **92**, 020503 (2015).

[59] I. D. Moore, P. Dendooven, and J. Ärje, "The IGISOL technique — three decades of developments," Hyperfine Interactions **223**, 17 (2014).

[60] A. Nieminen, J. Huikari, A. Jokinen, J. Äystö, P. Campbell, and E. Cochrane, "Beam cooler for low-energy radioactive ions," Nuclear Instruments and Methods in Physics Research Section A: Accelerators, Spectrometers, Detectors and Associated Equipment **469**, 244 (2001).

112

[61] B. Cheal, K. Baczynska, J. Billowes, P. Campbell, F. C. Charlwood, T. Eronen, D. H. Forest, A. Jokinen, T. Kessler, I. D. Moore, M. Reponen, S. Rothe, M. Rüffer, A. Saastamoinen, G. Tungate, and J. Äystö, "Laser Spectroscopy of Niobium Fission Fragments: First Use of Optical Pumping in an Ion Beam Cooler Buncher," Phys. Rev. Lett. **102**, 222501 (2009).

[62] V. Krutov, "Internal conversion in the field of an "electronic bridge"," JETP Lett. **52**, 584 (1990).

[63] V. Strizhov and E. Tkalya, "Decay channel of low-lying isomer state of the ^{229}Th nucleus. Possibilities of experimental investigation," Sov. Phys. JETP **72**, 387 (1991).

[64] F. F. Karpeshin, I. M. Band, M. B. Trzhaskovskaya, and A. Pastor, "On the Question of Electron Bridge for the 3.5-eV Isomer of ^{229}Th," Phys. Rev. Lett. **83**, 1072 (1999).

[65] P. Kálmán and T. Bükki, "Deexcitation of ^{229}Th^m : Direct γ decay and electronic-bridge process," Phys. Rev. C **63**, 027601 (2001).

[66] P. V. Bilous, E. Peik, and A. Pálffy, "Laser-induced electronic bridge for characterization of the ^{229m}Th $\to$ ^{229g}Th nuclear transition with a tunable optical laser," New Journal of Physics **20**, 013016 (2018).

[67] E. V. Tkalya, "Probability of nonradiative excitation of nuclei in transitions of an electron in an atomic shell," Sov. Phys. JETP. **75**, 200 (1992).

[68] E. V. Tkalya, "Cross-section for excitation of the low-lying (less-than-or-equal-to-5 eV) ^{229}Th isomer with laser-radiation by the inverse electron bridge," Soviet Journal of Nuclear Physics-USSR **55**, 1611 (1992).

[69] D. A. Varshalovich, A. N. Moskalev, and V. K. Khersonskii, *Quantum Theory Of Angular Momemtum* (World Scientific, 1988).

[70] G. H. Gossel, V. A. Dzuba, and V. V. Flambaum, "Calculation of strongly forbidden $M1$ transitions and g-factor anomalies in atoms considered for parity-nonconservation measurements," Phys. Rev. A **88**, 034501 (2013).

[71] U. I. Safronova, M. S. Safronova, and W. R. Johnson, "Forbidden $M1$ and $E2$ transitions in monovalent atoms and ions," Phys. Rev. A **95**, 042507 (2017).

[72] F. Karpeshin, I. Band, M. Trzhaskowskaya, and B. Zon, "Study of ^{229m}Th through laser-induced resonance internal conversion," Physics Letters B **282**, 267 (1992).

[73] M. S. Safronova and U. I. Safronova, "Relativistic many-body calculation of energies, oscillator strengths, transition rates, lifetimes, polarizabilities, and quadrupole moment of a Fr-like Th iv ion," Phys. Rev. A **87**, 062509 (2013).

[74] I. I. Sobelman, *Atomic Spectra And Radiative Transitions* (Springer-Verlag, Berlin, 1979).

[75] M. Schwarz, O. Versolato, A. Windberger, F. Brunner, T. Ballance, S. Eberle, J. Ullrich, P. Schmidt, A. Hansen, A. Gingell, M. Drewsen, and J. Crespo López-Urrutia, "Cryogenic linear Paul trap for cold highly charged ion experiments," Review of Scientific Instruments **83**, 083115 (2012).

[76] B. W. Shore, K. Bergmann, A. Kuhn, S. Schiemann, J. Oreg, and J. H. Eberly, "Laser-induced population transfer in multistate systems: A comparative study," Phys. Rev. A **45**, 5297 (1992).

[77] P. Jönsson, F. Parpia, and C. Fischer, "HFS92: A program for relativistic atomic hyperfine structure calculations," Computer Physics Communications **96**, 301 (1996).

[78] P. Micke, S. Kühn, L. Buchauer, J. R. Harries, T. M. Bücking, K. Blaum, A. Cieluch, A. Egl, D. Hollain, S. Kraemer, T. Pfeifer, P. O. Schmidt, R. X. Schüssler, C. Schweiger, T. Stöhlker, S. Sturm, R. N. Wolf, S. Bernitt, and J. R. Crespo López-Urrutia, "The Heidelberg compact electron beam ion traps," Review of Scientific Instruments **89**, 063109 (2018).

[79] `https://www.mpi-hd.mpg.de/pfeifer/page.php?id=89`, accessed: 2018-09-07.

[80] M. F. Gu, "The flexible atomic code," Canadian Journal of Physics **86**, 675 (2008).

[81] H. Bekker, private communication (2018).

[82] A. Yoshimi, H. Hara, T. Hiraki, Y. Kasamatsu, S. Kitao, Y. Kobayashi, K. Konashi, R. Masuda, T. Masuda, Y. Miyamoto, K. Okai, S. Okubo, R. Ozaki, N. Sasao, O. Sato, M. Seto, T. Schumm, Y. Shigekawa, S. Stellmer, K. Suzuki, S. Uetake, M. Watanabe, A. Yamaguchi, Y. Yasuda, Y. Yoda, K. Yoshimura, and M. Yoshimura, (2018), arXiv:1705.07320 [nucl-ex] .

[83] A. Yoshimi, H. Hara, T. Hiraki, Y. Kasamatsu, S. Kitao, Y. Kobayashi, K. Konashi, R. Masuda, T. Masuda, Y. Miyamoto, K. Okai, S. Okubo, R. Ozaki, N. Sasao, O. Sato, M. Seto, T. Schumm, Y. Shigekawa, S. Stellmer, K. Suzuki, S. Uetake, M. Watanabe, A. Yamaguchi, Y. Yasuda, Y. Yoda, K. Yoshimura, and M. Yoshimura, "Nuclear resonant scattering experiment with fast time response: Photonuclear excitation of ^{201}Hg," Phys. Rev. C **97**, 024607 (2018).

[84] A. Pálffy, W. Scheid, and Z. Harman, "Theory of nuclear excitation by electron capture for heavy ions," Phys. Rev. A **73**, 012715 (2006).

[85] A. Pálffy, J. Evers, and C. H. Keitel, "Isomer Triggering via Nuclear Excitation by Electron Capture," Phys. Rev. Lett. **99**, 172502 (2007).

[86] C. J. Chiara, J. J. Carroll, M. P. Carpenter, J. P. Greene, D. J. Hartley, R. V. F. Janssens, G. J. Lane, J. C. Marsh, D. A. Matters, M. Polasik, J. Rzadkiewicz, D. Seweryniak, S. Zhu, S. Bottoni, A. B. Hayes, and S. A. Karamian, "Isomer depletion as experimental evidence of nuclear excitation by electron capture," Nature **554**, 216 (2018).

[87] M. Yabashi, H. Tanaka, and T. Ishikawa, "Overview of the SACLA facility," Journal of Synchrotron Radiation **22**, 477 (2015).

[88] S. L. Haan and V. L. Jacobs, "Projection-operator approach to the unified treatment of radiative and dielectronic recombination," Phys. Rev. A **40**, 80 (1989).

[89] A. Burgess, "Delectronic Recombination and the Temperature of the Solar Corona." Astrophysical Journal **139**, 776 (1964).

[90] M. Reed and B. Simon, *Methods of Modern Mathematical Physics*, Vol. 4 (Academic Press, 1978).

[91] P.-A. Raboud, J.-C. Dousse, J. Hoszowska, and I. Savoy, "L_1 to N_5 atomic level widths of thorium and uranium as inferred from measurements of L and M x-ray spectra," Phys. Rev. A **61**, 012507 (1999).

[92] K. S. Mann, N. Singh, R. Mittal, K. L. Allawadhi, and B. S. Sood, "Measurement of L X-ray production cross sections in elements $57 \leq Z \leq 92$ at 22.6 keV," Journal of Physics B: Atomic, Molecular and Optical Physics **23**, 3521 (1990).

[93] V. Letokhov, *Laser Photoionization Spectroscopy* (Academic Press, 1987).

[94] P. Ring and P. Schuck, *The Nuclear Many-Body Problem* (Springer Verlag, New York, 1980).

[95] `http://www.nndc.bnl.gov/ensdf/`, accessed: 2018-09-12.

[96] N. Minkov, private communication (2018).

[97] `http://ddwap.mah.se/tsjoek/compas/`, accessed: 2018-09-21.

[98] F. Parpia, C. Fischer, and I. Grant, "GRASP92: A package for large-scale relativistic atomic structure calculations," Computer Physics Communications **94**, 249 (1996).

[99] E. Anderson, Z. Bai, C. Bischof, S. Blackford, J. Demmel, J. Dongarra, J. Du Croz, A. Greenbaum, S. Hammarling, A. McKenney, and D. Sorensen, *LAPACK Users' Guide*, 3rd ed. (Society for Industrial and Applied Mathematics, Philadelphia, PA, 1999).

[100] P. A. Chodash, J. T. Burke, E. B. Norman, S. C. Wilks, R. J. Casperson, S. E. Fisher, K. S. Holliday, J. R. Jeffries, and M. A. Wakeling, "Nuclear excitation by electronic transition of ^{235}U," Phys. Rev. C **93**, 034610 (2016).

[101] E. V. Tkalya and A. V. Nikolaev, "Magnetic hyperfine structure of the ground-state doublet in highly charged ions ^{229}Th$^{89+,87+}$ and the Bohr-Weisskopf effect," Phys. Rev. C **94**, 014323 (2016).

[102] F. F. Karpeshin, S. Wycech, I. M. Band, M. B. Trzhaskovskaya, M. Pfützner, and J. Żylicz, "Rates of transitions between the hyperfine-splitting components of the ground-state and the 3.5 eV isomer in ^{229}Th^{89+}," Phys. Rev. C **57**, 3085 (1998).

[103] A. S. Davydov, *Quantum mechanics* (Pergamon, 1965).

[104] M. Rose, *Multipole fields* (J. Wiley & Sons, New York, 1955).

[105] E. El Baz and B. Castel, *Graphical methods of spin algebras in atomic, nuclear, and particle physics* (Marcel Dekker, 1972).

[106] D. M. Brink and G. R. Satchler, *Angular Momemtum* (Clarendon Press, Oxford, 1968).

Acknowledgements